

声子的量子操控和 不同种离子间的纠缠操作

(申请清华大学理学博士学位论文)

培养单位：交叉信息研究院

学 科：物理学

研 究 生：张君华

指导教师：金奇奂 副教授

二〇一七年十二月

Quantum Operation of Phonons and Entanglement of Multi-Species Ions

Dissertation Submitted to

Tsinghua University

in partial fulfillment of the requirement

for the degree of

Doctor of Philosophy

in

Physics

by

Zhang Junhua

Dissertation Supervisor: Associate Professor Kihwan Kim

December, 2017

关于学位论文使用授权的说明

本人完全了解清华大学有关保留、使用学位论文的规定，即：

清华大学拥有在著作权法规定范围内学位论文的使用权，其中包括：（1）已获学位的研究生必须按学校规定提交学位论文，学校可以采用影印、缩印或其他复制手段保存研究生上交的学位论文；（2）为教学和科研目的，学校可以将公开的学位论文作为资料在图书馆、资料室等场所供校内师生阅读，或在校园网上供校内师生浏览部分内容；（3）根据《中华人民共和国学位条例暂行实施办法》，向国家图书馆报送可以公开的学位论文。

本人保证遵守上述规定。

（保密的论文在解密后遵守此规定）

作者签名： _____

导师签名： _____

日 期： _____

日 期： _____

摘 要

以声子为媒介的多离子间的相干操作是实现离子阱系统规模化重要的一环，而声子系统本身也可以作为平台进行量子模拟和量子计算。本文介绍了一些面向声子的量子操作技术，包括声子的算术操作、投影测量和任意声子 NOON 态的制备。此外也展示了通过 Mølmer-Sørensen 操作实现的镱-171 和钡-138 离子间的量子纠缠。用于实现这些操作的离子阱系统包含一个镱-171 离子和一个钡-138 离子，离子内能级和声子的量子相干操作由受激拉曼跃迁实现。该系统的相关细节和搭建系统所需的实验技术也在文中进行了介绍。

关键词：声子；多种离子的离子阱系统；NOON 态；投影测量

Abstract

In scaling up the trapped-ion system, phonons serve an important role as the quantum bus to mediate multi-qubit operations in the trap. Moreover, phonons by themselves can be used as the carrier of information to perform quantum simulations and computations. In this thesis, various control protocols of phonons are discussed and demonstrated, including the uniform driving, the projective measurement and the generation of arbitrary NOON states of phonons. The entanglement of a $^{171}\text{Yb}^+$ ion and a $^{138}\text{Ba}^+$ ion through the Mølmer-Sørensen interaction is also demonstrated. The trapped-ion system to implement these protocols consists of a $^{171}\text{Yb}^+$ ion and a $^{138}\text{Ba}^+$ ion with the quantum control realized by stimulated Raman transitions. The details of this system and the experiment techniques required in constructing the system are discussed as well.

Key words: Phonon; Multi-species trapped-ion system; NOON state; Projective measurement.

Table of Contents

Chapter 1	Introduction	1
Chapter 2	Theory of the Trapped-ion System	3
2.1	The Paul Trap.....	3
2.2	$^{138}\text{Ba}^+$ Ion	6
2.3	$^{171}\text{Yb}^+$ Ion.....	9
2.4	Electric Quadrupole Transitions	10
2.5	Harmonic Modes of Phonons	11
2.6	Sideband Operations of Phonons	14
2.7	Cooling of the Phonon Modes	19
2.8	Mølmer-Sørensen Interaction	22
Chapter 3	Laser Systems.....	25
3.1	Lasers for Barium Ion	25
3.1.1	Alignment of 493 nm and 650 nm Diode Laser.....	25
3.1.2	Frequency Arrangements of 493 nm and 650 nm Laser	28
3.1.3	1762 nm Fiber Laser and 614 nm Diode Laser	32
3.2	Lasers for Stimulated Raman Transitions.....	33
3.2.1	Alignment of Raman Lasers.....	33
3.2.2	Frequency Arrangement of Raman Lasers.....	35
3.3	Techniques for Alignment	39
3.3.1	AOM Alignment	39
3.3.2	Diffraction Patterns	40
Chapter 4	Pulse Sequencer	44
4.1	Function and Performance Goals.....	44
4.2	Pipeline Timer and Time Stamp Encoding.....	47
4.3	Structure of the Pulse Sequencer	49
Chapter 5	Geometric Landau-Zener-Stückelberg Interferometry.....	52
5.1	Introduction.....	52
5.2	Landau-Zener Transition	53
5.3	Adiabatic Passage	53

5.4	Geometric Landau-Zener-Stückelberg Interferometry	56
5.5	Robustness of the Interferometry	56
Chapter 6	Arithmetic Operations of Phonons	58
6.1	Introduction	58
6.2	Uniform Driving of the Phonons	60
6.3	Arithmetic Operations of the Phonons	61
6.4	Projective Measurement of the Fock States	65
Chapter 7	Deterministic Generation of High NOON States of Phonons.....	67
7.1	Introduction	67
7.2	Generation Sequence of the NOON State	68
7.3	Fidelity and Quantum Fisher Information	71
7.4	Experiment Protocol to Measure the Fidelity	74
7.5	Optimization and Parameter Calibration	78
Chapter 8	Entanglement of $^{171}\text{Yb}^+$ Ion and $^{138}\text{Ba}^+$ Ion.....	80
8.1	Introduction	80
8.2	Parameter Calibration	82
8.2.1	Coarse Calibration	82
8.2.2	Fine Calibration	82
8.2.3	Final Calibration	84
8.3	Fidelity of the Mølmer-Sørensen Interaction	85
Chapter 9	Conclusion and Outlook	87
References.....		88
Acknowledgement.....		96
Appendix A	Verilog Code of the Pulse Sequencer	98
A.1	Top Module	98
A.2	Input Dispatcher	99
A.3	Controller	103
A.4	FIFO Array	104
A.5	Timer	110
A.6	Common Modules and Functions	111

List of Figures

Fig. 2.1	The four-rod trap and the vacuum chamber of our system.	5
Fig. 2.2	The operations and related energy levels of $^{138}\text{Ba}^+$ ion.....	7
Fig. 2.3	The operations and related energy levels of $^{171}\text{Yb}^+$ ion.	8
Fig. 2.4	The geometry dependency of the Rabi frequency of the quadrupole transition.	10
Fig. 2.5	An example of the measurement of the phonon distribution.	18
Fig. 2.6	The coupling strength of the red sideband transition related to n and η	21
Fig. 2.7	The EIT cooling scheme.	21
Fig. 2.8	The scheme of the Mølmer-Sørensen interaction.	22
Fig. 2.9	The simulated time evolution of the Mølmer-Sørensen interaction.....	24
Fig. 3.1	The arrangement of all the laser beams entering the trap.	25
Fig. 3.2	The alignment of the 493 nm laser with the legend of the optical components used in this chapter.	26
Fig. 3.3	The alignment of the 650 nm laser.....	27
Fig. 3.4	The numerical simulation of the optical Bloch equations.....	28
Fig. 3.5	The spectrum and frequency arrangements of the 493 nm laser beams.....	29
Fig. 3.6	The spectrum and frequency arrangements of the 650 nm laser beam.	30
Fig. 3.7	The alignment of the 650 nm laser.....	31
Fig. 3.8	The alignment of the 1762 nm laser.....	31
Fig. 3.9	A typical spectrum of the $\Delta m = 0$ quadrupole transition of a single $^{138}\text{Ba}^+$ ion with phonon sidebands.	32
Fig. 3.10	The alignment of the 355 nm and 532nm pulsed lasers.....	34
Fig. 3.11	A typical phonon sideband spectrum of two $^{138}\text{Ba}^+$ ions.....	35
Fig. 3.12	A typical phonon sideband spectrum of two $^{171}\text{Yb}^+$ ions.....	36

Fig. 3.13	The crosstalk effect of the 532 nm Raman beams to the $^{171}\text{Yb}^+$ ion.	37
Fig. 3.14	A small tool used to analyze the crosstalk problem and arrange the frequencies.	38
Fig. 3.15	The diffraction patterns of the laser beam hitting a needle tip, with varying position of the needle tip along the axis of the beam.	40
Fig. 3.16	The diffraction patterns of the laser beam hitting a needle tip, with varying position of the needle tip around the focus of the beam.	41
Fig. 3.17	The diffraction patterns of the laser beam hitting a pinhole with a diameter of $150\ \mu\text{m}$	43
Fig. 4.1	A typical pulse sequence in experiment.	45
Fig. 4.2	The TTL pulse sequencer of our system and its user interface.	46
Fig. 4.3	The control structure of our system.	47
Fig. 4.4	The states of the T and C register of the pipeline timer.	48
Fig. 4.5	The module structure and signal flow of the pulse sequencer.	51
Fig. 5.1	The transition probability and dynamics of the Landau-Zener transition.	54
Fig. 5.2	The adiabatic passage.	54
Fig. 5.3	The procedure of a LZS interferometry.	55
Fig. 5.4	The interference fringe and its robustness of the geometric LZS interferometry.	57
Fig. 6.1	The numerical simulations of the adiabatic driving.	59
Fig. 6.2	The uniform driving with a spin-echo in the middle.	62
Fig. 6.3	The procedure of the arithmetic addition and subtraction operations.	62
Fig. 6.4	The Wigner function and phonon distribution of coherent state $\alpha = 0.8$ after 1, 2, 3 times of arithmetic addition operation.	63
Fig. 6.5	The real component of the density matrix of superposition state $ 0\rangle+ 1\rangle$ after 1, 2, 3 times of arithmetic addition operation.	64
Fig. 6.6	The real component of the density matrix of superposition state $ 2\rangle+ 3\rangle$ after 1,	

2 times of arithmetic subtraction operation.	64
Fig. 6.7 The protocol to reconstruct the density matrix and the Wigner function.....	65
Fig. 6.8 The protocol of the projective measurement.....	66
Fig. 7.1 The generation sequence of $ 3003\rangle$ state.	68
Fig. 7.2 The procedure of the composite-pulse operation.	69
Fig. 7.3 The procedure to measure $P_{0,N}$	76
Fig. 7.4 The parity oscillations of the generated NOON states from $N = 1$ to $N = 9$	77
Fig. 7.5 The (a) fidelity and (b) quantum Fisher information of the generated NOON states.	77
Fig. 7.6 The phase calibration scheme.	79
Fig. 8.1 The fidelity diagram of the Mølmer-Sørensen interaction with respect to the detuning of the driving frequencies.	84
Fig. 8.2 The experiment result of the Mølmer-Sørensen interaction.....	86

Chapter 1 Introduction

Driven by the unending curiosity, we human try to seek for deeper understanding of the nature in various directions, and try to make use of what we understand on the way. As the scale of the system we study gets smaller and smaller, quantum effects start to manifest themselves and we encounter new phenomenon which are confusing in the classical realm of physics, such as quantum superposition and entanglement. As Rolf Landauer put it, *information is physical* [1], different physics leads to different informatics. We have extracted the potential of communication and computation from electrodynamics, and with the power of quantum mechanics we can make it faster and more secure. In the theory of quantum informatics, there are quite some impressive result, such as Shor's factorization algorithm [2], Grover's search algorithm [3], and various schemes of quantum simulation [4] [5]. However, in experiment, we experimentalists are still struggling to realize the beautiful blueprints of a practical quantum computer drawn by the theorists. So far, many kinds of quantum systems with different nature and their own advantages are studied and explored, including photonic system [6], neutral atom system [7], superconducting system [8], trapped-ion system [9] and many else [10] [11].

The trapped-ion system, among others, is better isolated from the noisy environment and takes the advantage of the uniformity of atomic parameters, which makes it a good platform for developing and testing basic quantum operations. Now the research interest of the trapped-ion community lies mainly in integrating these basic operations and scaling up the system to make it truly superior than classical systems [12]. For scaling up the system, the interaction between different ions is essential. The collective motion of the ions in the same trap serves as a good quantum bus for coupling different ions in the same trap [13]. And the entanglement between ions in different traps has been realized through photons [14]. However, in order to combine these two protocols together, it would be convenient to have different species of ions trapped in the same trap with one species serving as a quantum interface for remote entanglement and others as local memory. Hence the entanglement operation between different species of ions is an important technique.

During the five years of my PhD. program, my research is primarily focused on developing and implementing quantum control protocols for phonons. As an experimentalist, I have learnt that details are important for a successful experiment, any careless mistake tends to come back and bite you in unexpected ways. And if you do the job with right tricks, the life would be much easier. So in this thesis, other than introducing our experiment system, summarizing the research projects I have done, I will also share some experiment techniques I find useful in developing and maintaining the experiment system. I hope that other fellow experimentalists would also find them useful.

Chapter 2 Theory of the Trapped-ion System

2.1 The Paul Trap

According to the Laplace equation, a 3-D static electric field with no charge distribution should not have local minimum, so it is not possible to steadily hold a charged particle. However, a Paul trap is able to trap a charged particle with a rotating radio frequency (RF) electric field, whose averaged pseudopotential is a harmonic potential [9]. For a linear Paul trap, the radial confinement is provided by the RF field, while the axial confinement is provided by DC voltages.

The trapping effect of a linear Paul trap can be analyzed by calculating the pseudopotential that the ion experiences in the radial direction. Suppose the RF field has no axial component, the instantaneous electric field potential is

$$V(x, y, z, t) = k \frac{V_a}{2} \cdot \frac{2z^2 - x^2 - y^2}{A^2} + \frac{V_r}{2} \cdot \frac{x^2 - y^2}{R^2} \cdot \cos \Omega t, \quad (2.1)$$

in which V_a is the DC voltage for the axial confinement, A is the effective distance from the DC electrodes to the center of the trap, V_r is the voltage of the RF field, R is the effective distance between the center and the RF electrodes, Ω is the frequency of the RF field, and k is a geometric factor that accounts for the shape of the electrodes. The terms in Equ. (2.1) can be understood intuitively in this way. Considering the symmetry of the system, there should be no first order term in the equation. For the DC part, the sign of z^2 is positive because it should provide axial confinement, and the signs of x^2 and y^2 are negative because there should be no local minimum. Also the signs of x^2 and y^2 in the RF part are different for the same reason. From Equ. (2.1), we can derive the electric field,

$$\mathbf{E}(x, y, z, t) = \frac{kV_a}{A^2} (x, y, -2z) - \frac{V_r \cos \Omega t}{R^2} (x, -y, 0). \quad (2.2)$$

According to the Newton's second law, the motion of an ion with charge q and mass m can be described by

$$\frac{d^2}{dt^2} r_i + \frac{\Omega^2}{4} [a_i + 2p_i \cos \Omega t] r_i = 0, \quad (2.3)$$

in which (r_x, r_y, r_z) is the position of the ion, and

$$\begin{aligned} a_x = a_y &= -\frac{a_z}{2} = -\frac{4kqV_a}{A^2\Omega^2m}, \\ p_x = -p_y &= \frac{2qV_r}{R^2\Omega^2m}, \quad p_z = 0. \end{aligned} \quad (2.4)$$

This is the Mathieu equation. When $|p_i|, |a_i| \ll 1$, the approximated solution up to the first order [15] is

$$r_i(t) = A_i \left[1 + \frac{p_i}{2} \cos \Omega t \right] \cos(\omega_i t + \phi_i), \quad (2.5)$$

in which

$$\omega_i = \frac{\Omega}{2} \sqrt{a_i + \frac{p_i^2}{2}} \quad (2.6)$$

are the frequencies of the harmonic oscillation modes of the ion. These frequencies are important parameters for the quantum control of the motion of the ion, and will be analyzed later with a different approach in this chapter. From Equ. (2.5), we can see that the motion of the ion basically consists of two types of oscillation, one is the previously mentioned harmonic oscillation, and the other one with frequency Ω is the so-called ‘‘intrinsic micromotion’’. Moreover, there is also ‘‘excess micromotion’’ if the ion is not at the center of the RF field. It is just the oscillation driven by the RF field and usually has negative impact to the operations of the ion. This is often the case in experiment when the background electric field is nonzero. So usually extra DC electrodes are placed near the trap to compensate the background field.

The trap we use in the experiment is a four-rod trap (Fig. 2.1). The RF signal is applied to the two RF electrodes and DC voltages is applied to the two needle electrodes (DC1). The DC voltages can also be applied to the two RF ground electrode (GND) to break the symmetry of the radial direction. The two auxiliary DC electrodes (DC2, DC3) are used to compensate the background electric field to minimize the excess micromotion [16].

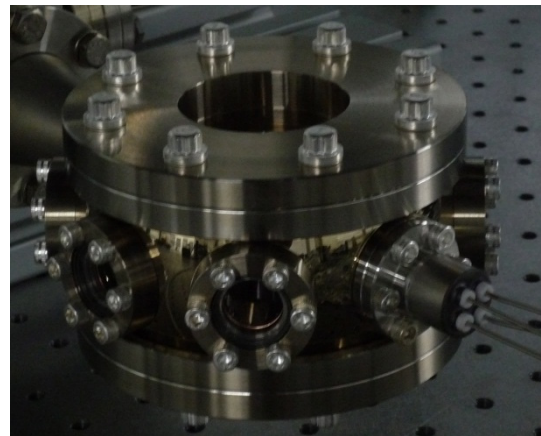
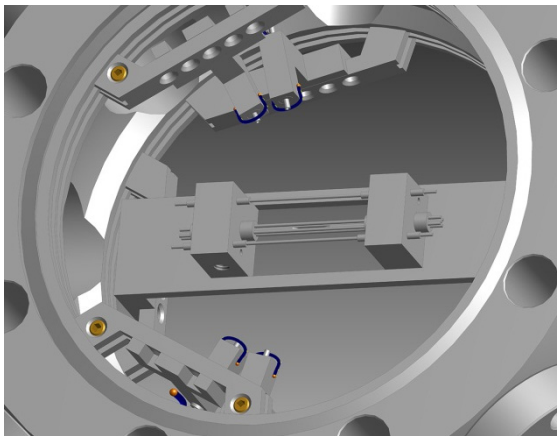
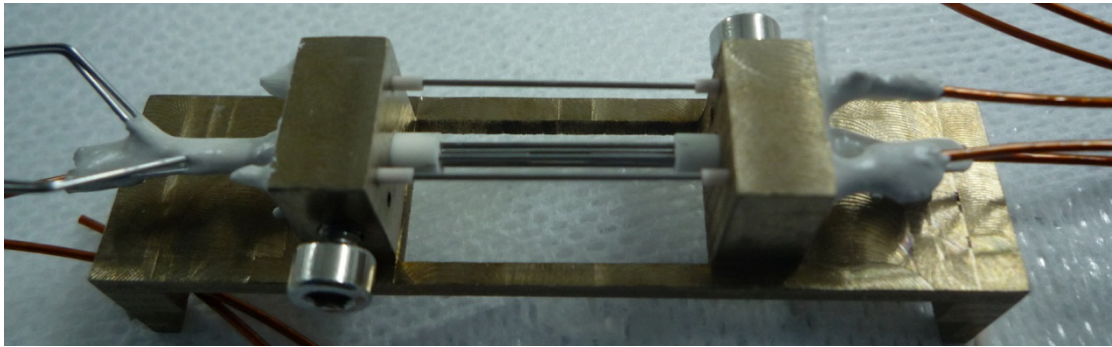
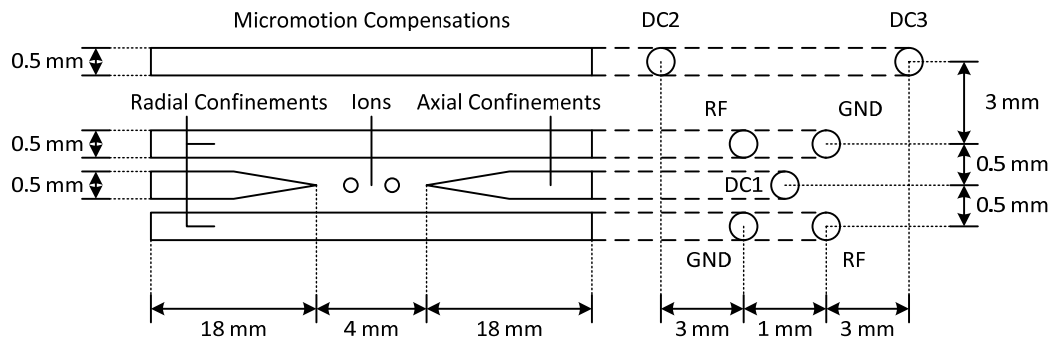


Fig. 2.1 The four-rod trap and the vacuum chamber of our system.

2.2 $^{138}\text{Ba}^+$ Ion

One kind of the ions we use is the $^{138}\text{Ba}^+$ ion, which has no nuclear spin. The related energy levels and operations are in Fig. 2.2. The two Zeeman levels of $S_{1/2}$ are used as the qubit, with $|m = +1\rangle$ denoted as $|\downarrow\rangle$ and $|m = -1\rangle$ as $|\uparrow\rangle$. The Landé g -factors of these levels are also shown in the figure.

The initialization of the qubit is implemented by optical pumping method [17]. A 493 nm laser beam with pure σ^+ polarization is applied to pump the population to $|\downarrow\rangle$. The detection of the qubit state is realized by first shelving the $|\downarrow\rangle$ state to metastable levels, $D_{5/2}$, with 1762 nm laser through an electric quadrupole transition [18], and then excite the cyclic transitions between $S_{1/2}$ and $P_{1/2}$ with 493 nm laser to collect the scattered fluorescence photons. The Doppler cooling operation of the ion is implemented in the same way, with an additional 614 nm laser to repump the population from $D_{5/2}$ levels and the 493 nm laser beam is slightly red-detuned. For all the operations involving 493 nm laser, there is a 25% probability that the ion will decay from $P_{1/2}$ to $D_{3/2}$, rather than $S_{1/2}$. So a 650 nm laser beam is always applied to repump the population from $D_{3/2}$ levels. The quantum operation of the qubit states is realized through stimulated Raman transitions [19] with a 532 nm pulsed laser.

The loading of the $^{138}\text{Ba}^+$ ion is realized by photoionization. Small shards of barium metal is placed in a small needle tube oven that can be heated up by applying electric current. The barium atoms shooting out of the oven are first excited by a 413 nm laser beam from 1S_0 to 3D_1 and then ionized by a 493 nm laser beam around the center of the trap.

Other isotopes of barium are also used in other groups, such as ^{137}Ba with hyperfine structure. The hyperfine qubit has a significantly longer coherence time than the Zeeman qubit. But the more complicated level structure also requires more complicated laser configurations. For our system, the $^{138}\text{Ba}^+$ ion is used because the coherence time of the qubit can be extended to around 1 ms with active compensation of the magnetic field fluctuation, which is long enough for the experiments.

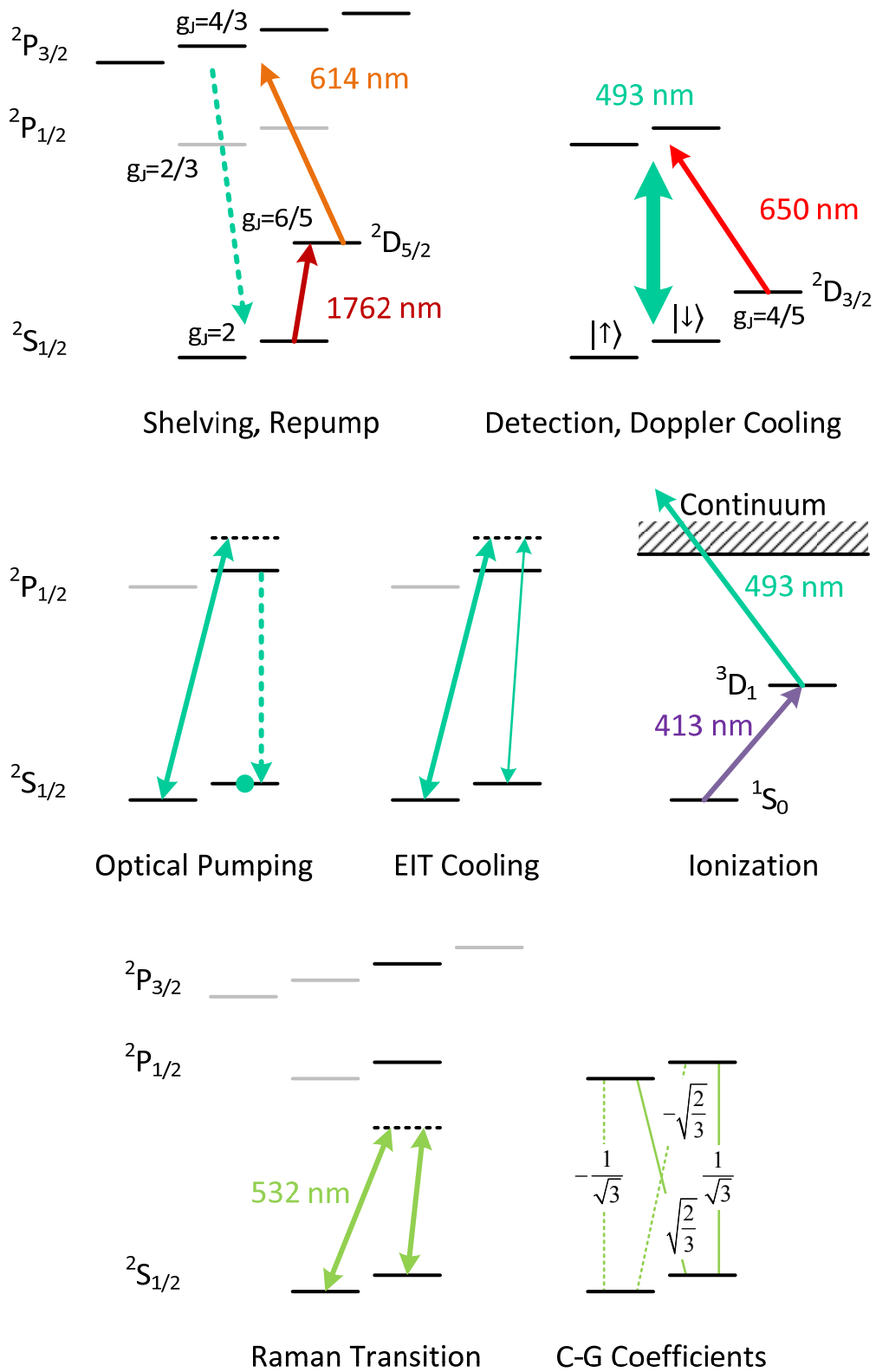


Fig. 2.2 The operations and related energy levels of $^{138}\text{Ba}^+$ ion.

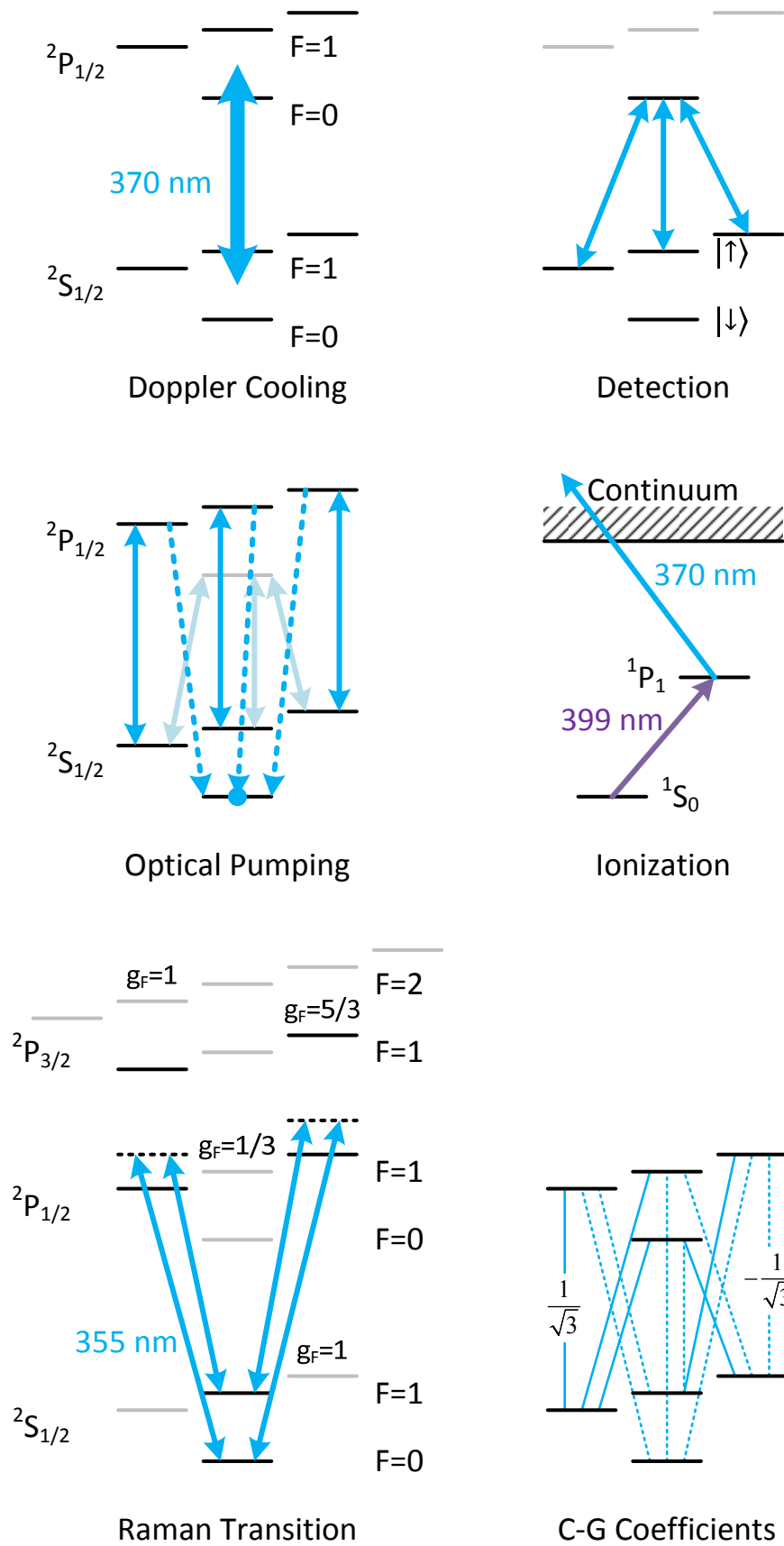


Fig. 2.3 The operations and related energy levels of $^{171}\text{Yb}^+$ ion.

The C-G coefficients of all the possible transitions have the same absolute value $1/\sqrt{3}$. The dashed lines indicate the negative ones.

2.3 $^{171}\text{Yb}^+$ Ion

The other kind of the ions we use is the $^{171}\text{Yb}^+$ ion with nuclear spin $1/2$. The level structure of the $^{171}\text{Yb}^+$ ion is more complicated due to the nuclear spin (Fig. 2.3). We use the two hyperfine levels of $S_{1/2}$, $|F = 0, m = 0\rangle$ and $|F = 1, m = 0\rangle$, as the qubit, with the hyperfine splitting of 12.64281212 GHz. These two states have no first order Zeeman effect, so the coherence time can be very long.

The detection operation of the qubit is realized by exciting the cyclic transition between levels $|F = 1, m = 0, \pm 1\rangle$ of $S_{1/2}$ and $|F = 0\rangle$ of $P_{1/2}$ with 370 nm laser. For the initialization of the qubit, the 370 nm laser is modulated with an electro-optical modulator (EOM) to generate a sideband of 2.105 GHz, so that the transitions between $F = 1$ levels of both $S_{1/2}$ and $P_{1/2}$ are excited and the ion will be pumped to $|\downarrow\rangle$ eventually. Similarly, the Doppler cooling operation of the $^{171}\text{Yb}^+$ ion is implemented by adding a 14.74 GHz sideband to excite all the possible transitions between $S_{1/2}$ and $P_{1/2}$ levels. The quantum operation of the qubit state can be realized either by Raman transition with a 355 nm pulsed laser or by magnetic dipole transition excited by microwave fields [19]. The loading of the $^{171}\text{Yb}^+$ ion is also realized by photoionization. The ytterbium atoms are first excited from 1S_0 to 1P_1 by a 399 nm laser beam and then ionized by a 370 nm laser beams.

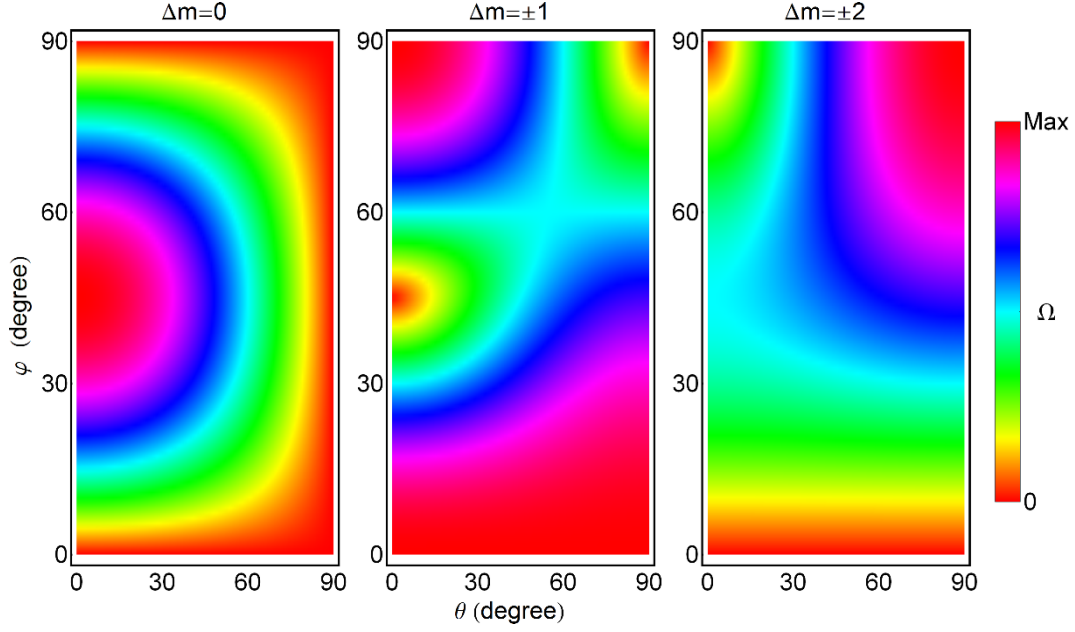


Fig. 2.4 The geometry dependency of the Rabi frequency of the quadrupole transition.

2.4 Electric Quadrupole Transitions

The transitions between the Zeeman levels of $S_{1/2}$ and $D_{5/2}$ of the $^{138}\text{Ba}^+$ ion are electric quadrupole transitions. In our system, these transitions are mainly used for shelving, but they can also be used as qubit transitions if quantum manipulation of the motion is not required. Since there are two Zeeman levels in $S_{1/2}$ and six in $D_{5/2}$, and the electric quadrupole transition is able to couple the levels with $\Delta m \leq 2$, these electric quadrupole transitions are actually quite handy in performing experiments that requires more than two levels.

The Rabi frequency of an electric quadrupole transition can be calculated by [20]

$$\Omega = \left| \frac{eE}{2\hbar} \langle S_{1/2}, m_S | (\boldsymbol{\epsilon} \cdot \hat{\mathbf{r}}) (\mathbf{k} \cdot \hat{\mathbf{r}}) | D_{5/2}, m_D \rangle \right|, \quad (2.7)$$

in which E is the amplitude of the electric field, $\boldsymbol{\epsilon}$ is the unit vector describing the polarization of the laser field, \mathbf{k} is the wave vector and $\hat{\mathbf{r}}$ is the position operator for the valence electron. The formula above can be expanded as

$$\Omega = \left| \frac{eE}{2\hbar} \langle S_{1/2} || r^2 \mathbf{C}^2 || D_{5/2} \rangle \sum_{q=-2}^2 \begin{pmatrix} 1/2 & 2 & 5/2 \\ -m_S & q & m_D \end{pmatrix} c_{ij}^{(q)} \epsilon_i n_j \right|, \quad (2.8)$$

in which $\langle S_{1/2} || r^2 \mathbf{C}^2 || D_{5/2} \rangle$ is the reduced matrix element and is independent of m .

The geometry dependency of the Rabi frequency is contained in $g^{(a)} = c_{ij}^{(q)} \epsilon_i n_j$. The geometry of the interaction can be modeled by the angle φ between the wave vector \mathbf{k} and the magnetic field \mathbf{B} and the angle θ between the polarization vector $\boldsymbol{\epsilon}$ and the vector \mathbf{B} projected into the plane of incidence. Without loss of generality, we can assume

$$\begin{aligned} \mathbf{B} &= (0, 0, B), & \mathbf{k} &= k(\sin \varphi, 0, \cos \varphi), \\ \boldsymbol{\epsilon} &= (\cos \theta \cos \varphi, \sin \theta, -\cos \theta \sin \varphi), \end{aligned} \quad (2.9)$$

and then

$$\begin{aligned} g^{(0)} &= \frac{1}{2} |\cos \theta \sin 2\varphi|, \\ g^{(\pm 1)} &= \frac{1}{\sqrt{6}} |\cos \theta \cos 2\varphi + i \sin \theta \cos \varphi|, \\ g^{(\pm 2)} &= \frac{1}{\sqrt{6}} \left| \frac{1}{2} \cos \theta \sin 2\varphi + i \sin \theta \sin \varphi \right|. \end{aligned} \quad (2.10)$$

The geometry dependency is illustrated in Fig. 2.4. The configuration used in our system is $\theta = 0^\circ$ and $\varphi = 45^\circ$, corresponding to the horizontal polarization of the 1762 nm laser beam.

2.5 Harmonic Modes of Phonons

When the ions are trapped in a 3-D harmonic potential, the motion of the ions can be decomposed into harmonic modes with different frequencies. For N ions in the trap, there are $2N$ radial modes and N axial modes. The frequency of each mode is determined by the strength of confinement of the corresponding direction.

For two ions with different mass, m_1 and m_2 , in a trap with axial DC voltage V_a and radial RF voltage V_r , the classical Hamiltonian of the two ions are

$$\begin{aligned} H &= \frac{p_{1a}^2 + p_{1r}^2}{2m_1} + \frac{p_{2a}^2 + p_{2r}^2}{2m_2} \\ &+ \frac{V_a}{2} (x_{1a}^2 + x_{1r}^2) + \left(\frac{V_r}{2} - \frac{V_a}{4} \right) (x_{1a}^2 + x_{1r}^2) \\ &+ Q[(x_{1a} + x_{2a})^2 + (x_{1r} + x_{2r})^2]^{-1/2}, \quad Q = \frac{e^2}{4\pi\epsilon_0}, \end{aligned} \quad (2.11)$$

where the terms with subscript ‘‘1’’ are associated with ion 1, and the terms with subscript ‘‘a’’ are associated with axial direction. In the equilibrium state, the two ions should have a spacing of d and suppose that the oscillation of the ions in all the modes is way smaller than d , then we can expand the columb potential term in the vicinity of $x_{1a} + x_{2a} = d$

and $x_{1r} + x_{2r} = 0$, which is

$$\begin{aligned} (x_{1a} + x_{2a})^{-1} &= \frac{1}{d} - \frac{1}{d^2}(x_{1a} + x_{2a} - d) + \frac{1}{d^3}(x_{1a} + x_{2a} - d)^2 \\ &\quad + O[(x_{1a} + x_{2a} - d)^3], \\ [d^2 + (x_{1r} + x_{2r})^2]^{-\frac{1}{2}} &= \frac{1}{d} - \frac{1}{2d^3}(x_{1r} + x_{2r})^2 + O[(x_{1r} + x_{2r})^3]. \end{aligned} \quad (2.12)$$

When the system is in the equilibrium state, for axial modes we should have

$$\frac{dp_{(i)a}}{dt} = -\frac{\partial H}{\partial x_{(i)a}} = 0, \quad (2.13)$$

which yields

$$V_a x_{(i)a} - \frac{Q}{d^2} = 0, \quad (2.14)$$

and thus

$$d = \sqrt[3]{\frac{2Q}{V_a}}, \quad x_{1a} = x_{2a} = \frac{d}{2}. \quad (2.15)$$

By substituting

$$x_{(i)a} \rightarrow \frac{d}{2} + x_{(i)a}, \quad (2.16)$$

and neglecting the constant terms, we can simplify the axial part of the Hamiltonian to

$$H_a = \frac{p_{1a}^2}{2m_1} + \frac{p_{2a}^2}{2m_2} + V_a(x_{1a}^2 + x_{2a}^2 + x_{1a}x_{2a}). \quad (2.17)$$

Similarly,

$$H_r = \frac{p_{1r}^2}{2m_1} + \frac{p_{2r}^2}{2m_2} + \frac{1}{2}(V_r - V_a)(x_{1r}^2 + x_{2r}^2) - \frac{V_a}{2}x_{1r}x_{2r}. \quad (2.18)$$

The two Hamiltonians have the unified form of

$$H = \frac{p_1^2}{2m_1} + \frac{p_2^2}{2m_2} + V(x_1^2 + x_2^2 + Cx_1x_2), \quad (2.19)$$

for axial modes $C = 1$ and for radial modes $C = -V_a/(V_r - V_a)$. Now consider the small harmonic oscillation solution of the system,

$$\begin{pmatrix} x_1 \\ x_2 \end{pmatrix} = \begin{pmatrix} A_{11} & A_{12} \\ A_{21} & A_{22} \end{pmatrix} \begin{pmatrix} e^{i\omega_1 t} \\ e^{i\omega_2 t} \end{pmatrix}. \quad (2.20)$$

According to the Hamiltonian equations,

$$\frac{dx_i}{dt} = \frac{\partial H}{\partial p_i}, \quad \frac{dp_i}{dt} = -\frac{\partial H}{\partial x_i}, \quad (2.21)$$

we have

$$\begin{pmatrix} p_1 \\ p_2 \end{pmatrix} = \begin{pmatrix} m_1 & 0 \\ 0 & m_2 \end{pmatrix} \begin{pmatrix} A_{11} & A_{12} \\ A_{21} & A_{22} \end{pmatrix} \begin{pmatrix} i\omega_1 & 0 \\ 0 & i\omega_2 \end{pmatrix} \begin{pmatrix} e^{i\omega_1 t} \\ e^{i\omega_2 t} \end{pmatrix} \quad (2.22)$$

and

$$\begin{pmatrix} m_1 & 0 \\ 0 & m_2 \end{pmatrix} \begin{pmatrix} A_{11} & A_{12} \\ A_{21} & A_{22} \end{pmatrix} \begin{pmatrix} \omega_1^2 & 0 \\ 0 & \omega_2^2 \end{pmatrix} \begin{pmatrix} e^{i\omega_1 t} \\ e^{i\omega_2 t} \end{pmatrix} = V \begin{pmatrix} 2 & C \\ C & 2 \end{pmatrix} \begin{pmatrix} A_{11} & A_{12} \\ A_{21} & A_{22} \end{pmatrix}. \quad (2.23)$$

This yields

$$\begin{aligned} [(2-C)V - m_1\omega_i^2]A_{1i} - [(2-C)V - m_2\omega_i^2]A_{2i} &= 0, \\ \{[(2-C)V - m_2\omega_i^2][(2+C)V - m_1\omega_i^2] \\ + [(2-C)V - m_1\omega_i^2][(2+C)V - m_2\omega_i^2]\}A_{1i} &= 0. \end{aligned} \quad (2.24)$$

The frequency ω_i should be independent of the amplitude, and assuming $m_1 \geq m_2$, so

$$\begin{aligned} \omega_i^2 &= \frac{V}{\mu}(1 \pm \alpha), & \frac{A_{1i}}{A_{2i}} &= \frac{C}{2} \cdot \frac{1 - \beta}{\beta \pm \alpha}, \\ \mu &= \frac{m_1 m_2}{m_1 + m_2}, & \rho &= \frac{\mu}{m_1 + m_2}, \\ \alpha &= \sqrt{1 - (4 - C^2)\rho}, & \beta &= \sqrt{1 - 4\rho}, \end{aligned} \quad (2.25)$$

in which $i = 1$ takes the plus sign.

By applying the following linear transformation, the Hamiltonian can be decoupled,

$$\begin{aligned} \begin{pmatrix} x_1 \\ x_2 \end{pmatrix} &= U_x \begin{pmatrix} x_H \\ x_L \end{pmatrix}, \\ U_x &= \frac{1}{\sqrt{2\alpha}} \begin{pmatrix} \operatorname{sgn} C \sqrt{\frac{(1-\beta)(\alpha-\beta)}{1+\alpha}} & \sqrt{\frac{(1-\beta)(\alpha+\beta)}{1-\alpha}} \\ \sqrt{\frac{(1+\beta)(\alpha+\beta)}{1+\alpha}} & -\operatorname{sgn} C \sqrt{\frac{(1+\beta)(\alpha-\beta)}{1-\alpha}} \end{pmatrix}, \end{aligned} \quad (2.26)$$

where $\operatorname{sgn} C$ is the sign of C and the subscript ‘‘H’’ and ‘‘L’’ denotes the mode of higher

and lower frequency respectively. The Hamiltonian is thus

$$H = \frac{p_1^2}{2m_1} + \frac{p_2^2}{2m_2} + V(x_H^2 + x_L^2). \quad (2.27)$$

For the generalized momentums, we assume the linear transformation to be

$$\begin{pmatrix} p_1 \\ p_2 \end{pmatrix} = U_p \begin{pmatrix} p_H \\ p_L \end{pmatrix}, \quad (2.28)$$

so

$$\begin{aligned} \frac{d}{dt} \begin{pmatrix} p_1 \\ p_2 \end{pmatrix} &= -V \begin{pmatrix} 2 & C \\ C & 2 \end{pmatrix} \begin{pmatrix} x_1 \\ x_2 \end{pmatrix} \\ &= -V \begin{pmatrix} 2 & C \\ C & 2 \end{pmatrix} U_x \begin{pmatrix} x_H \\ x_L \end{pmatrix} \\ &= U_p \frac{d}{dt} \begin{pmatrix} p_H \\ p_L \end{pmatrix} = -U_p \cdot 2V \begin{pmatrix} x_H \\ x_L \end{pmatrix}, \end{aligned} \quad (2.29)$$

and hence

$$U_p = \frac{1}{2} \begin{pmatrix} 2 & C \\ C & 2 \end{pmatrix} U_x. \quad (2.30)$$

So the decoupled Hamiltonian is

$$H = \frac{1 + \alpha}{4\mu} p_H^2 + \frac{1 - \alpha}{4\mu} p_L^2 + V(x_H^2 + x_L^2), \quad (2.31)$$

and the effective mass of the two modes are

$$m_H = \frac{2\mu}{1 + \alpha}, \quad m_L = \frac{2\mu}{1 - \alpha}. \quad (2.32)$$

For axial modes, the one with higher frequency is the breathing mode (ions moving in the opposite direction) and the lower the center of mass mode (ions moving in the same direction). While for radial modes, the higher one is the center of mass mode, the lower one is the zig-zag mode.

2.6 Sideband Operations of Phonons

The quantized energy of a harmonic mode is described by a kind of bosonic quasi-particle, phonons. The Hamiltonian of a mode is written as

$$\hat{H} = \hbar\omega \left(\hat{a}^\dagger \hat{a} + \frac{1}{2} \right), \quad (2.33)$$

in which ω is the frequency of the mode, $\hat{a}^\dagger(\hat{a})$ is the creation (annihilation) operator of phonons in this mode. Usually the constant $1/2$ is omitted and \hbar is taken to be 1, so the Hamiltonian is simply $\hat{H} = \omega \hat{a}^\dagger \hat{a}$. The eigenstates of the Hamiltonian are ‘‘Fock’’ states, i.e. number states of phonon. The effect of the creation or annihilation operator on the Fock state with n phonons, $|n\rangle$, is just creating or removing a phonon,

$$\hat{a}^\dagger |n\rangle = \sqrt{n+1} |n+1\rangle, \quad \hat{a} |n\rangle = \sqrt{n} |n-1\rangle. \quad (2.34)$$

When an ion is interacting with the laser beam, momentum and energy transfer can happen between the phonon modes of the ion and the electromagnetic field. For a stimulated Raman transition, if the wavepacket size of the ion is much smaller than the wavelength of the laser, the Hamiltonian of the ion is,

$$\hat{H} = \frac{\Delta}{2} \hat{\sigma}_z + \omega \hat{a}^\dagger \hat{a} + \Omega \hat{\sigma}_x \cos(k\hat{x} - \lambda t + \phi), \quad (2.35)$$

in which Δ is the energy gap of the spin, ω is the frequency of the modes of interest, Ω is the coupling strength of the Raman transition, k is the wave vector difference of the two Raman beams projected to the direction of the mode, λ is the frequency difference of the two Raman beams, ϕ is the phase of the coupling, and \hat{x} is the position operator of the mode given by

$$\hat{x} = \sqrt{\frac{\hbar}{2m\omega}} (\hat{a}^\dagger + \hat{a}), \quad (2.36)$$

where m is the effective mass of the mode. The quantity

$$\eta = k \sqrt{\frac{\hbar}{2m\omega}} \quad (2.37)$$

is the Lamb-Dicke parameter, quantifying the coupling strength between the laser and the phonon modes. If the number of phonons n in the mode is low enough, i.e. in the Lamb-Dicke regime,

$$\eta^2(2n+1) \ll 1, \quad (2.38)$$

the cosine function in the Hamiltonian (2.35) can be expanded only to the first order. Depending on the value of λ , the Hamiltonian can be simplified to the following cases by taking the interaction picture of $\Delta \hat{\sigma}_z/2$ and $\omega \hat{a}^\dagger \hat{a}$, and then the rotating wave

approximation,

$$\begin{cases} \hat{H}_C = \frac{\Omega}{2} \hat{\sigma}_x & \lambda = \Delta \\ \hat{H}_B = \frac{i\eta\Omega}{2} (\hat{\sigma}^+ \hat{a}^\dagger - \hat{\sigma}^- \hat{a}) & \lambda = \Delta + \omega. \\ \hat{H}_R = \frac{i\eta\Omega}{2} (\hat{\sigma}^- \hat{a}^\dagger - \hat{\sigma}^+ \hat{a}) & \lambda = \Delta - \omega \end{cases} \quad (2.39)$$

Here \hat{H}_C , \hat{H}_B and \hat{H}_R is the Hamiltonian of the carrier, blue sideband and red sideband transition respectively. With these three operations, the state of the phonons can be controlled.

If more than one ions are trapped in one trap, the form of the Lamb-Dicke parameter will be more complicated, since the position operator \hat{x} of Equ. (2.36) is defined per phonon mode, but the position operator actually involved in the laser-ion interaction [Equ. (2.35)] is the position operator for each ion. If only one ion is in the trap, the two operators are identical, but not for more ions. Continue the calculation in the previous section, the position operators for the high-frequency and low-frequency modes are

$$\begin{aligned} \hat{x}_H &= \sqrt{\frac{\hbar}{2m_H\omega_H}} (\hat{a}_H^\dagger + \hat{a}_H) = \frac{\sqrt{\hbar}}{2} \left(\frac{1+\alpha}{V\mu} \right)^{\frac{1}{4}} (\hat{a}_H^\dagger + \hat{a}_H), \\ \hat{x}_L &= \sqrt{\frac{\hbar}{2m_L\omega_L}} (\hat{a}_L^\dagger + \hat{a}_L) = \frac{\sqrt{\hbar}}{2} \left(\frac{1-\alpha}{V\mu} \right)^{\frac{1}{4}} (\hat{a}_L^\dagger + \hat{a}_L). \end{aligned} \quad (2.40)$$

According to Equ. (2.26), the position operators for the two ions are

$$\begin{aligned} \begin{pmatrix} \hat{x}_1 \\ \hat{x}_2 \end{pmatrix} &= U_x \begin{pmatrix} \hat{x}_H \\ \hat{x}_L \end{pmatrix} \\ &= \sqrt{\frac{\hbar}{4\sqrt{V\mu}}} U_x \begin{pmatrix} (1+\alpha)^{\frac{1}{4}} & 0 \\ 0 & (1-\alpha)^{\frac{1}{4}} \end{pmatrix} \begin{pmatrix} \hat{a}_H^\dagger + \hat{a}_H \\ \hat{a}_L^\dagger + \hat{a}_L \end{pmatrix}. \end{aligned} \quad (2.41)$$

When ion i is interacting with the laser, the Lamb-Dicke parameter of mode H (L) is just the coefficient of $\hat{a}_H^\dagger + \hat{a}_H$ ($\hat{a}_L^\dagger + \hat{a}_L$) in the expansion of kx_i , so

$$(2.42)$$

$$\begin{aligned}\eta_{1L} &= k_1 \sqrt{\frac{\hbar(1-\beta)(\alpha+\beta)}{4\sqrt{V\mu}(1-\alpha)}}, \\ \eta_{2H} &= k_2 \sqrt{\frac{\hbar(1+\beta)(\alpha+\beta)}{4\sqrt{V\mu}(1+\alpha)}}, \\ \eta_{2L} &= -k_2 \operatorname{sgn} C \sqrt{\frac{\hbar(1+\beta)(\alpha-\beta)}{4\sqrt{V\mu}(1-\alpha)}}.\end{aligned}$$

Another usage of the sideband transition is to read out the population distribution of the Fock states. For example, the Rabi frequency of the blue sideband transition for the Fock state $|n\rangle$ scales as $\eta\Omega\sqrt{n+1}$. So if the blue sideband operation is applied for time t and the fluorescence detection is applied at the end, the population of each Fock state P_n can be inferred by fitting the fluorescence signal,

$$P_{\uparrow}(t) = \frac{1}{2} \left(1 - \sum_n P_n \cos \frac{\eta\Omega t}{\sqrt{n+1}} \right). \quad (2.43)$$

An example of this fitting method is given in Fig. 2.5.

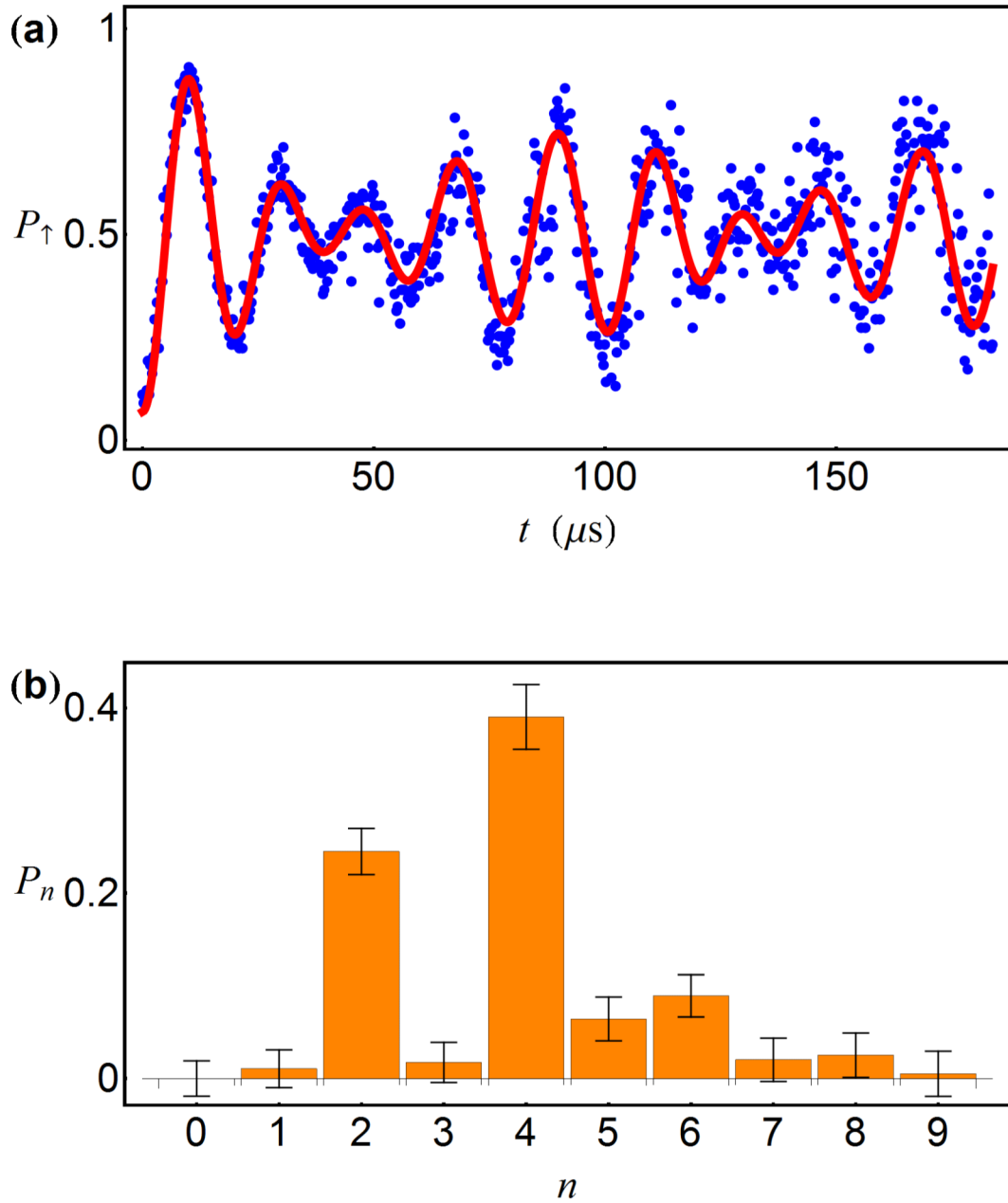


Fig. 2.5 An example of the measurement of the phonon distribution. (a) The fluorescence signal of the ion and its fitting. (b) The phonon distribution obtained from the fitting.

2.7 Cooling of the Phonon Modes

In order to perform sideband operations of phonons, the ions should first be cooled down to the Lamb-Dicke regime. Usually the first step of cooling is the Doppler cooling. The general idea of Doppler cooling is as follows. When a photon of a laser beam is scattered by an ion, the ion get a net momentum kick from the photon, because the scattering is omnidirectional and the ion gets no net momentum from the emission. If the laser beam is red-detuned, the scattering rate is slightly higher due to the Doppler effect if the ion moves towards the laser, which means on average the ion loses a small amount of momentum every time when the ion is moving towards the laser beam.

However, the Doppler cooling scheme cannot cool the ion all the way down to the ground state of motion. Although the net momentum gain from the emission of the photons is zero, the divergence is not. The recoil of the photon emission contributes to $\langle \hat{p}^2 \rangle$ rather than $\langle \hat{p} \rangle$. When the cooling effect is balanced by this heating effect, the Doppler cooling reaches its limit. To put it more intuitively, for a certain line shape of the spectrum and a certain detuning of the laser, the higher the scattering rate, the higher the limit, the steeper the slope of the spectrum, the lower the limit. For a simple spectrum of Lorentzian shape, such as $^{171}\text{Yb}^+$, the optimal value of the detuning is just the value that yields a scattering rate of half of the maximum. But for more complicated cases, such as $^{138}\text{Ba}^+$, this problem is not trivial. However the rule of thumb still holds, steeper slope and lower scattering.

The resolved sideband cooling is a technique that can cool the ion down from the Doppler cooling limit to near the ground state. The cooling mechanics of the resolved sideband cooling is basically a “going down the ladder” process [19]. Successive red sideband π -pulse for Fock states $|n\rangle$, $|n-1\rangle$, $|n-2\rangle$, ... are applied with optical pumping stages in between. Suppose the maximum occupied Fock state is $|n\rangle$, then after a red sideband π -pulse for that and an optical pumping stage, the population is transferred to $|n-1\rangle$, hence each step the maximum phonon number is reduced by one. Because this process has no heating mechanics, theoretically it can cool the ion all the way down to the vacuum state $|0\rangle$. But in experiment there are limiting factors like the heating effect from the environment and the infidelity of the sideband operation and the optical pumping.

Although the resolved sideband cooling can cool the ion down to the vacuum state with very high fidelity, the requirement for this protocol to apply is relatively demanding. If we consider all the higher order expansion of Hamiltonian (2.35), the coupling strength

of the red sideband transition for $|n > 0\rangle$ is

$$\Omega_R(n) = \frac{\mathcal{L}_{n-1}^1(\eta^2)}{\sqrt{n}} \Omega, \quad (2.44)$$

in which \mathcal{L} denotes the generalized Laguerre polynomial. The behavior of this function is as shown in Fig. 2.6. When n is too large, the coupling strength is effectively zero. So the resolved sideband cooling protocol can only be applied when the temperature of the ion is already pretty low.

Another drawback of the resolved sideband cooling protocol is that it can only cool down one mode each time, if multiple modes are required to be cooled down, the duration of the operation can become unfeasible. A less perfect but way more efficient cooling protocol is the electromagnetically induced transparency (EIT) cooling [21]. The EIT phenomena is one kind of coherent population trapping in a three level system. As shown in Fig. 2.2, in a Λ -type three level system, when a strong pump beam and a weak probe beam is applied simultaneously with a common detuning to the upper level, the scattering spectrum of the probe beam exhibits a Fano line shape (the blue curve in Fig. 2.7). The idea of EIT cooling is that, by arranging the power and the frequency of the probe and pump beam, the carrier of the electric dipole transition can be made vanishing, and the coupling to the red sideband transitions is much stronger than to the blue sideband transitions. In this way, the cooling limit is much lower than the Doppler cooling. The EIT cooling is very useful when the number of modes to be cooled down is large, since the peak can cover many modes at the same time (Fig. 2.7).

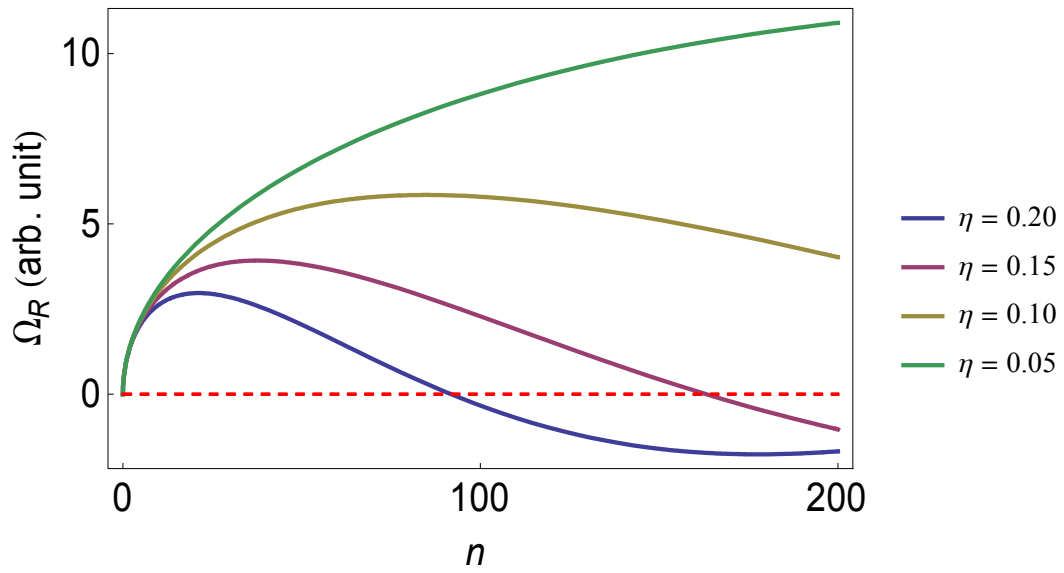


Fig. 2.6 The coupling strength of the red sideband transition related to n and η .

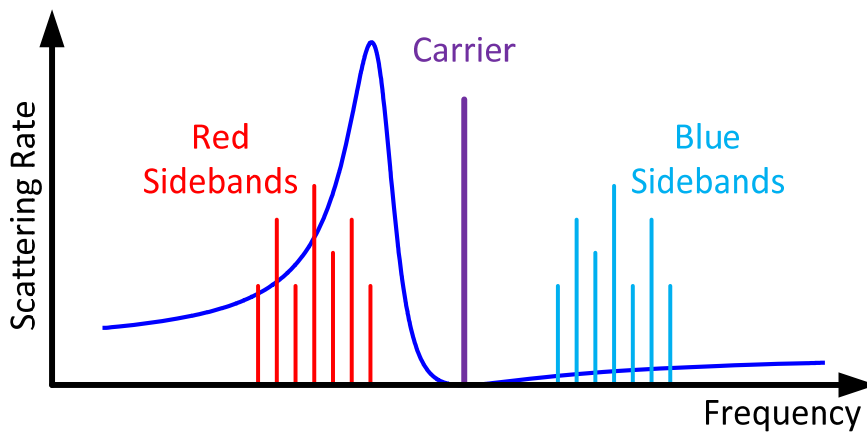


Fig. 2.7 The EIT cooling scheme.

2.8 Mølmer-Sørensen Interaction

The Mølmer-Sørensen (M-S) interaction is a two-ion entanglement operation mediated by phonons. This operation is first proposed by Anders Sørensen and Klaus Mølmer in 1999 [22] [23]. From the very beginning, the idea of the M-S interaction is something similar to a stimulated Raman transition. As shown in Fig. 2.8, by applying weak and off-resonant blue and red sideband couplings on both ions with identical coupling strength Ω and detuning δ from the sideband resonance,

$$\hat{H} = \frac{\Omega}{2} (\hat{\sigma}_y^{(1)} + \hat{\sigma}_y^{(2)}) (\hat{a}^\dagger e^{i\delta t} + \hat{a} e^{-i\delta t}), \quad (2.45)$$

only the energy conserving transitions, $|\downarrow\downarrow\rangle \leftrightarrow |\uparrow\uparrow\rangle$ and $|\downarrow\uparrow\rangle \leftrightarrow |\uparrow\downarrow\rangle$, are excited with Rabi frequency

$$\tilde{\Omega} = \frac{\Omega^2}{\delta}, \quad (2.46)$$

while all other paths of transition interfere destructively. One important advantage of the M-S interaction is that the Rabi frequency $\tilde{\Omega}$ is independent of the phonon occupation, hence the cooling condition of the ions is less demanding.

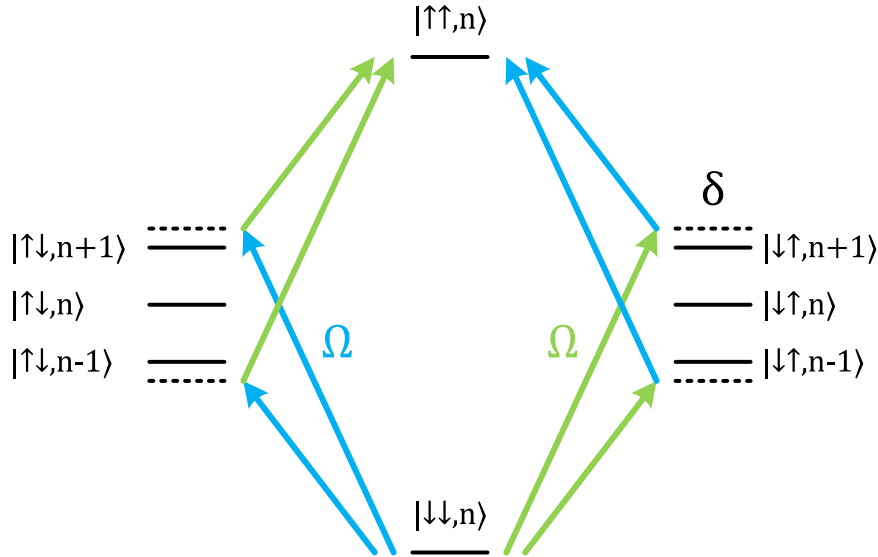


Fig. 2.8 The scheme of the Mølmer-Sørensen interaction.

However, the first version of the M-S interaction is basically a Raman transition of phonon sidebands which requires $\Omega \ll \delta$. The time required to entangle two ions is very long. So later the strong coupling scenario of this process is investigated and a fast version of the interaction is proposed [24]. Both strong and weak coupling can be modeled as spin-dependent evolution in the phase space of the phonon mode. The state of the ions acquires geometric phase when the ions are evolving in the phase space. If this evolution is a “round trip”, i.e. the initial and final state of phonon are identical, the state of the spins and the state of the phonons are decoupled. So the entanglement operation can be achieved by controlling the trace of the system in the phase space. Intuitively, for the weak coupling scenario the trace is just a tiny circle near the origin of the phase space along which the system trails many times, with each time contributing a small amount of geometric phase. A simulated time evolution of the weak coupling scenario is shown in Fig. 2.9(a). The tiny “round trips” in the phase space is revealed by the small oscillation of the green curve. For the strong coupling scenario, this circle is much bigger [Fig. 2.9(b)]. By controlling the coupling strength and the detuning, the required geometric phase can be obtained with less trips. For the fastest operation in this model, only one trip is enough. The detuning is given by $\delta = 2\Omega$. The time required to generate $|\downarrow\downarrow\rangle + |\uparrow\uparrow\rangle$ from $|\downarrow\downarrow\rangle$ is π/Ω .

But this is not yet the fastest. Even this fast version is in the adiabatic regime with respect to the secular motion of the ions. The analysis is actually performed in a rotating frame of reference with respect to the frequency of the phonon mode. Recently there have been many theory and experiment research of the ultrafast operation of phonons [25] [26] [27] [28]. The general idea is to model the system in a steady frame of reference and make use of the secular motion itself. Usually it requires complicated tailoring of the Hamiltonian to ensure the phase is correct and the trajectory in the phase space is a closed loop.

I implement the fast version of the M-S interaction in our system with one $^{171}\text{Yb}^+$ ion and one $^{138}\text{Ba}^+$ ion, but the ultrafast version still requires further study.

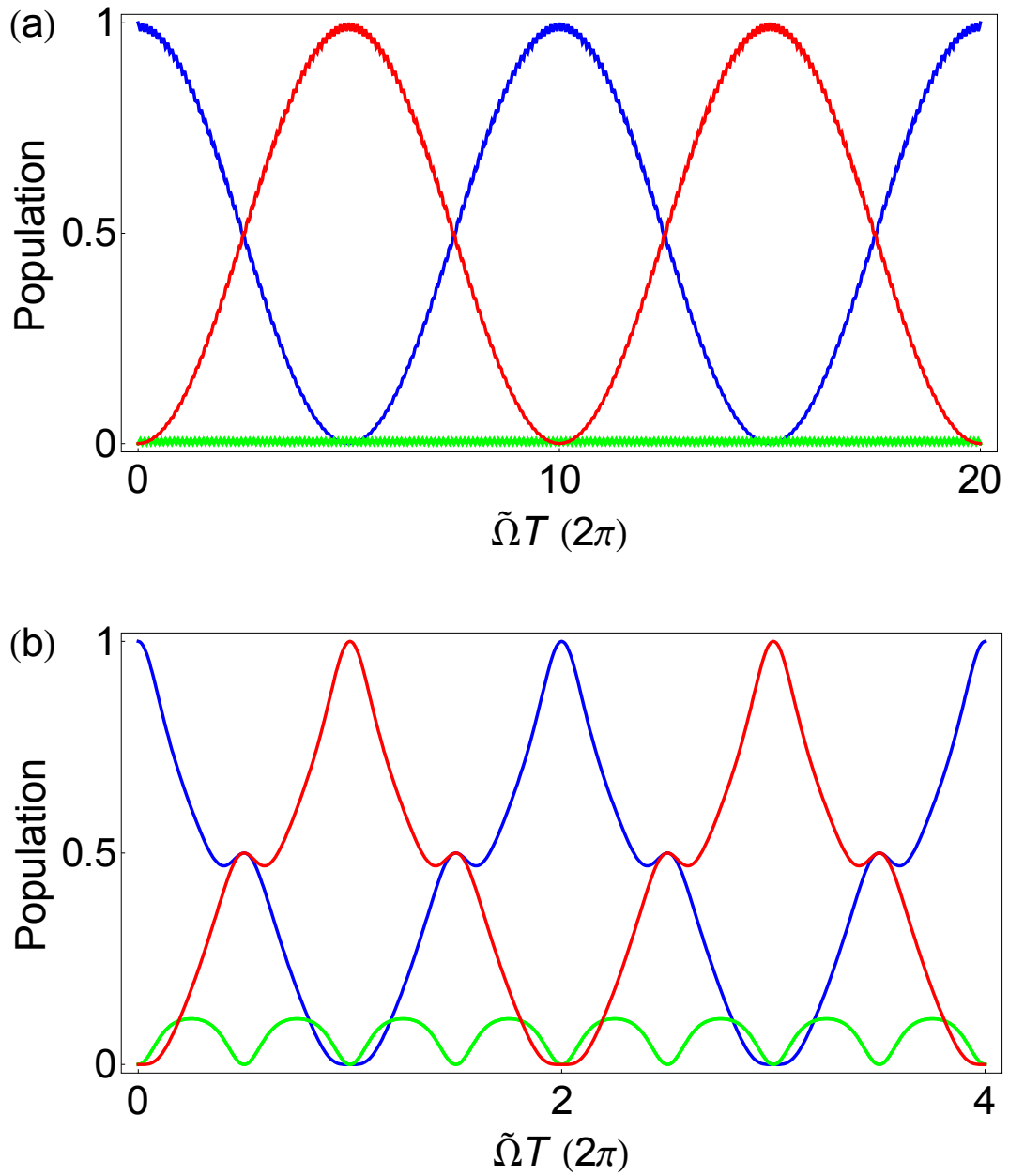


Fig. 2.9 The simulated time evolution of the Mølmer-Sørensen interaction. The red and blue curve denotes the population of $|\uparrow\uparrow\rangle$ and $|\downarrow\downarrow\rangle$ respectively. The populations of $|\downarrow\uparrow\rangle$ and $|\uparrow\downarrow\rangle$ are identical, and are both denoted as green. (a) The weak coupling scenario. (b) The strong coupling scenario.

Chapter 3 Laser Systems

The arrangement of all the laser beams entering the trap is shown in Fig. 3.1. The arrangement is primarily determined by the polarization requirement of each beam. The beams for the barium ion and stimulated Raman transitions will be discussed in detail in this chapter, while the information for lasers for the ytterbium ion can be found in [19].

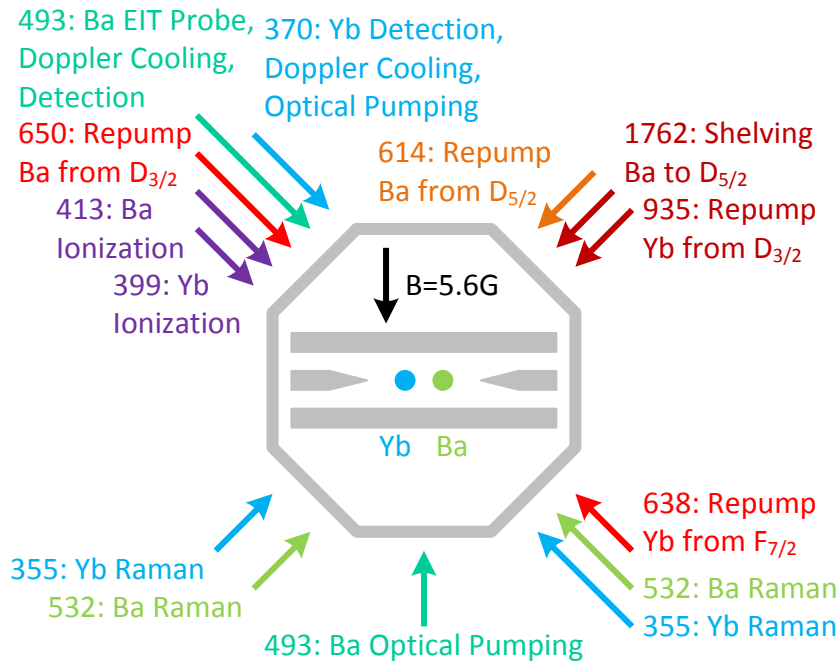


Fig. 3.1 The arrangement of all the laser beams entering the trap.

3.1 Lasers for Barium Ion

3.1.1 Alignment of 493 nm and 650 nm Diode Laser

The 493 nm diode laser is used to drive the transition between $S_{1/2}$ and $P_{1/2}$ levels of $^{138}\text{Ba}^+$ ion and implement Doppler cooling, EIT cooling, optical pumping and fluorescence detection operations. The laser is locked to a F-P cavity stabilized by a tellurium (Te) vapor cell with Doppler-free spectroscopy [29]. The alignment of the laser is in Fig. 3.2.

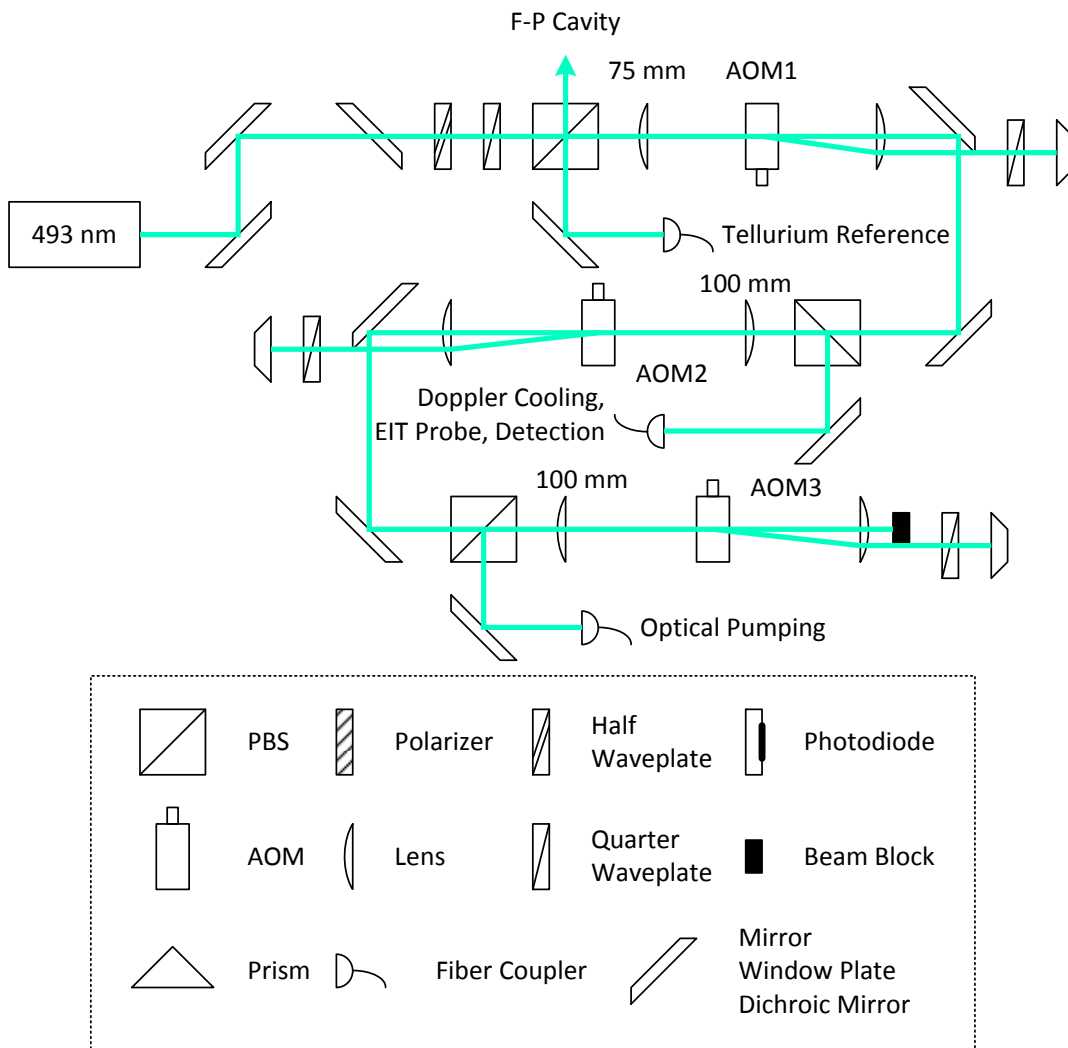


Fig. 3.2 The alignment of the 493 nm laser with the legend of the optical components used in this chapter.

In designing the alignment of the 493 nm laser, the following aspects are considered.

- We should be able to scan the frequency of the laser as far as possible without losing lock to the Te reference so that we can measure the spectral line shape of the beams. So the AOM1 is arranged in the double-pass scheme such that the power to the Te vapor cell is not significantly affected by the frequency scan.
- Aligning the beams to the trap and aiming them to the ion is a tedious work, while coupling beams to fibers is easy. So the beams are coupled to fibers before entering the trap, such that changes of the alignment on the laser side do not affect the trap side.
- The Doppler cooling beam, the detection beam and the probe beam for EIT cooling requires similar polarization configurations. It would save a lot of optical components and workload if they can be handled collectively. So in the alignment all the three beams are generated from a single AOM (AOM2) arranged also in double-pass scheme due to the frequency difference.
- By coupling lasers to fibers and using double-pass AOMs, a significant amount of laser power is lost. So all the AOMs are arranged serially to maximize the power usage.

The 650 nm diode laser is used to repump the population in $D_{3/2}$ metastable levels. The laser is locked to a F-P cavity and an iodine vapor cell reference with the same scheme as 493 nm laser. The alignment of the laser is in Fig. 3.3.

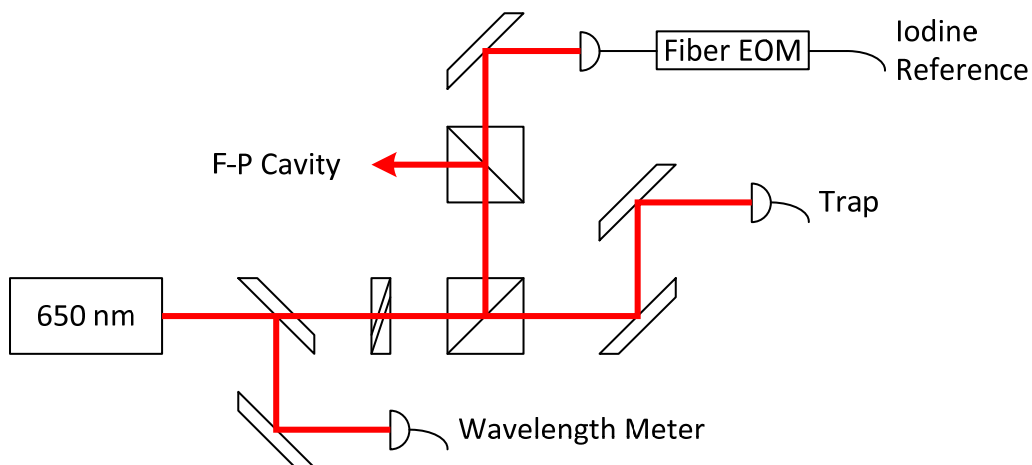


Fig. 3.3 The alignment of the 650 nm laser.

3.1.2 Frequency Arrangements of 493 nm and 650 nm Laser

For a $^{171}\text{Yb}^+$ ion in $P_{1/2}$ levels, the probability to decay to $D_{3/2}$ is only 0.5%, so the spectrum of 370 nm transition, $P_{1/2} \leftrightarrow S_{1/2}$, has a simple Lorentzian line shape. However, for $^{138}\text{Ba}^+$ ion, the probability to leak to $D_{3/2}$ states is 25%, so the line shape of 493 nm transition is strongly affected by the configuration of the 650 nm laser beam, and hence the determination of the laser parameters is not a trivial problem.

The interaction between 493nm, 650 nm lasers and the ion can be modeled by the optical Bloch equations [30]. The numerical analysis of the system can give some insight for the optimization of the laser parameters.

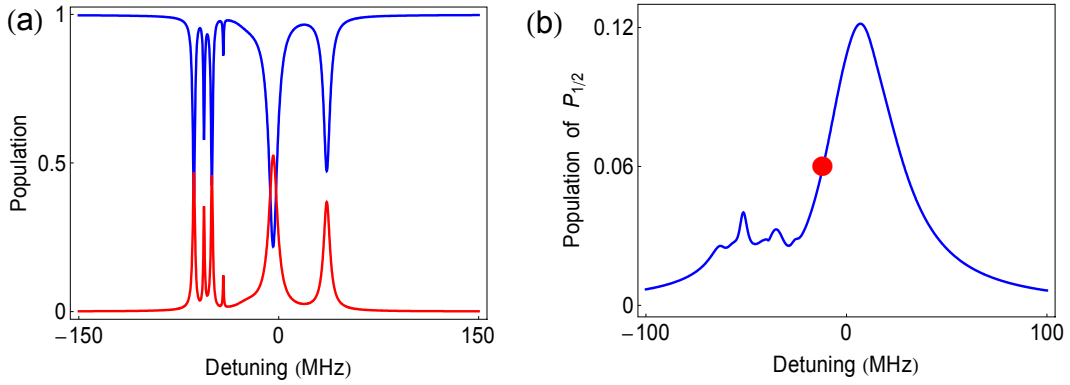


Fig. 3.4 The numerical simulation of the optical Bloch equations.

(a) The steady state solution for scanning the frequency of the optical pumping beam. The blue curve shows the population of the $|\downarrow\rangle$ state, the red curve shows the total population of $D_{3/2}$ levels. (b) The steady state solution for scanning the frequency of the Doppler cooling beam. The red spot indicates a typical frequency configuration of the beam.

For the optical pumping beam, ideally the polarization should purely be σ^+ , but in experiment this condition is very demanding, there are always a small amount of other polarization components remaining. As shown in Fig. 3.4(a), if there are 0.1% (power ratio) of π polarization and σ^- polarization remaining, the optical pumping fidelity can be poor around the resonance and the population mainly goes to $D_{3/2}$ levels. So for our system, the detuning of the optical pumping beam is set to around +120 MHz, where the optical pumping fidelity is insensitive to the polarization impurity, and the beam can be reused for the pumping beam of the EIT cooling. For the Doppler cooling beam, the rule of thumb is to maximize the slope of the scattering spectrum. As shown in Fig. 3.4(b), when the frequency of the Doppler cooling beam is near the dark resonance, the slope is steeper than the normal Lorentzian shape.

The frequency arrangements of all the 493 nm laser beams are in Fig. 3.5(a). The spectrum of the 493 nm transition is measured in experiment to verify the resonant frequency [Fig. 3.5(b)]. This spectrum is measured with the Doppler cooling beam by scanning the driving frequency of AOM1. It is clear that the resonant frequency is as depicted in Fig. 3.5(a).

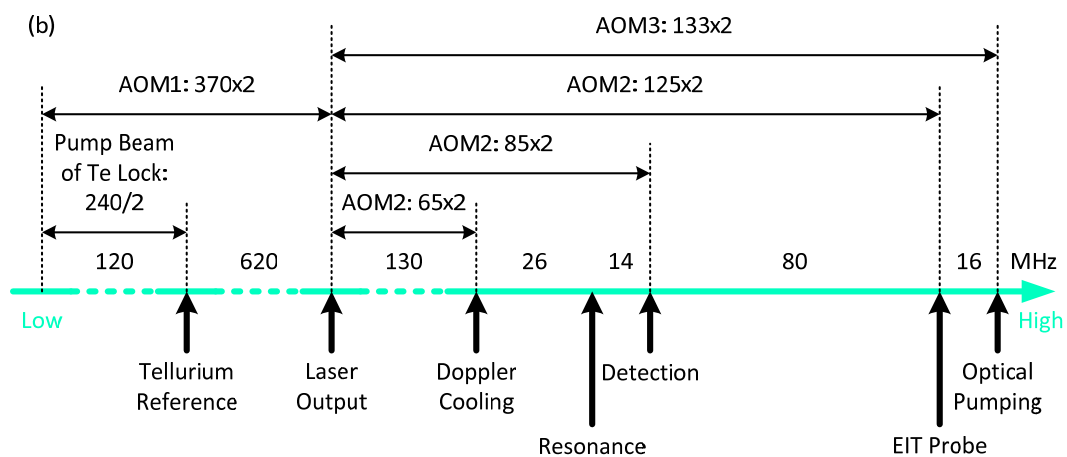
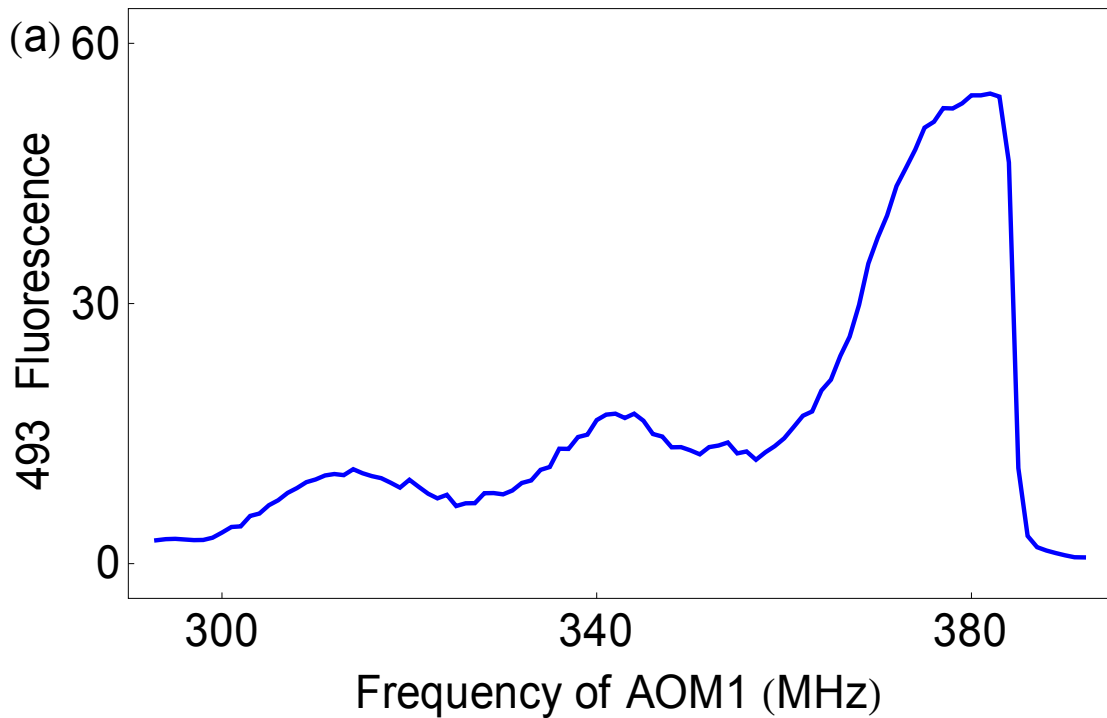


Fig. 3.5 The spectrum and frequency arrangements of the 493 nm laser beams. The numbers above the frequency axis is the frequency difference between each marked frequency.

The spectrum of the 650 nm transition are measured in a similar way, but with much lower intensities for both 493 nm and 650 nm beams to acquire a Lorentzian line shape [Fig. 3.6(a)]. The frequency arrangements of the 650 nm laser beams are in Fig. 3.6(b).

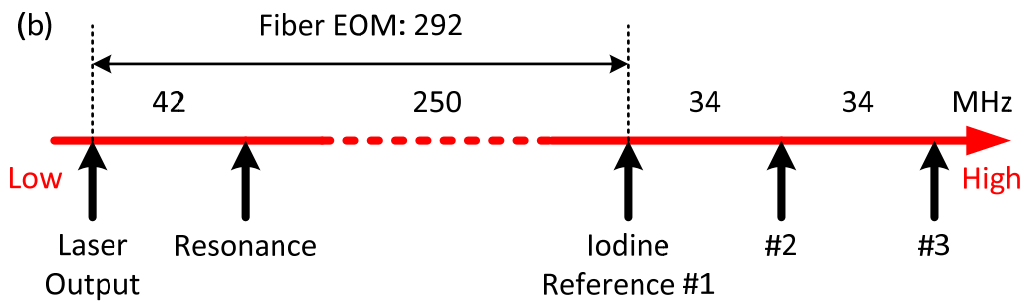
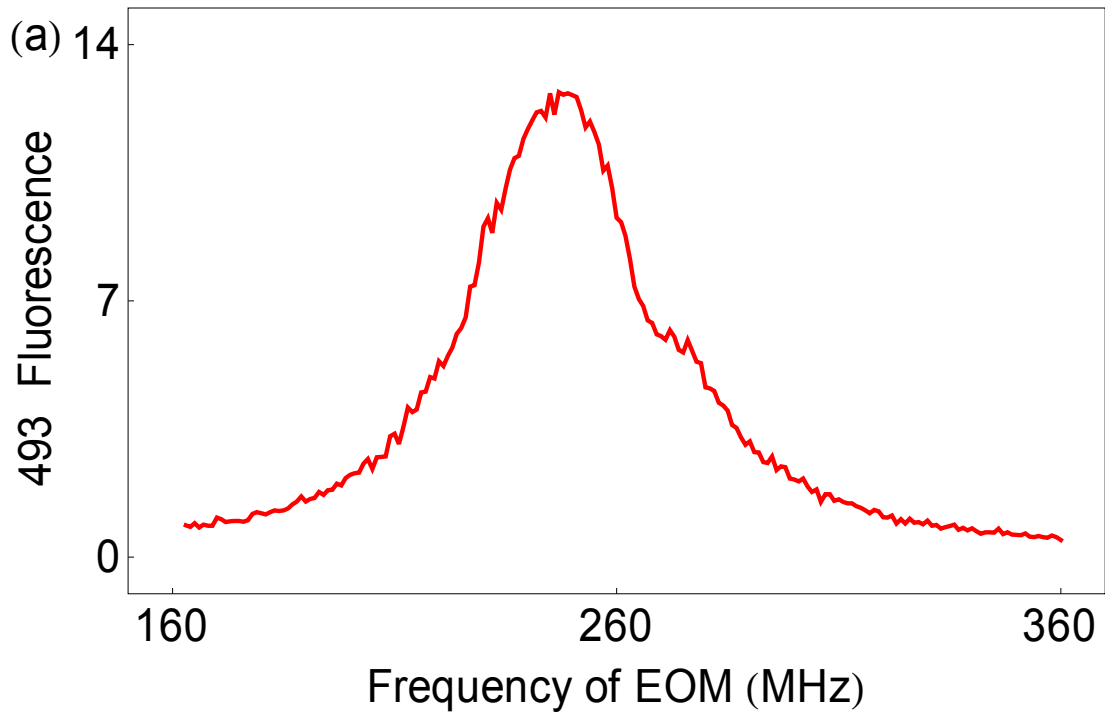


Fig. 3.6 The spectrum and frequency arrangements of the 650 nm laser beam.

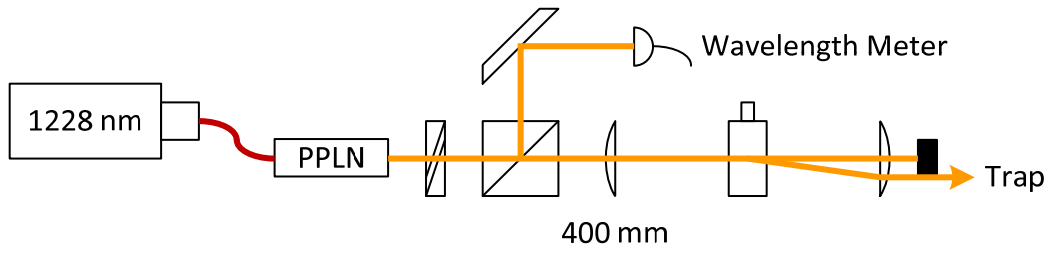


Fig. 3.7 The alignment of the 650 nm laser.

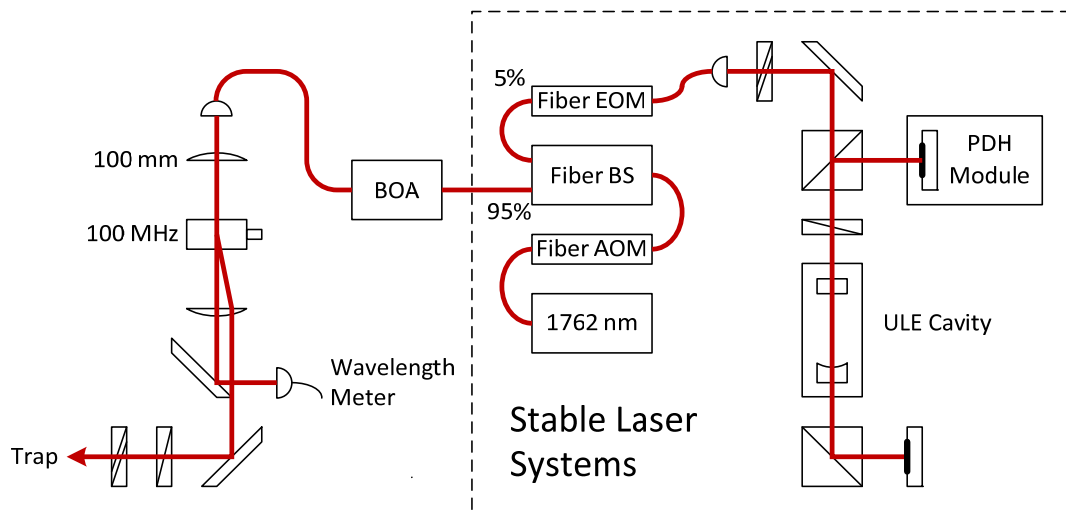
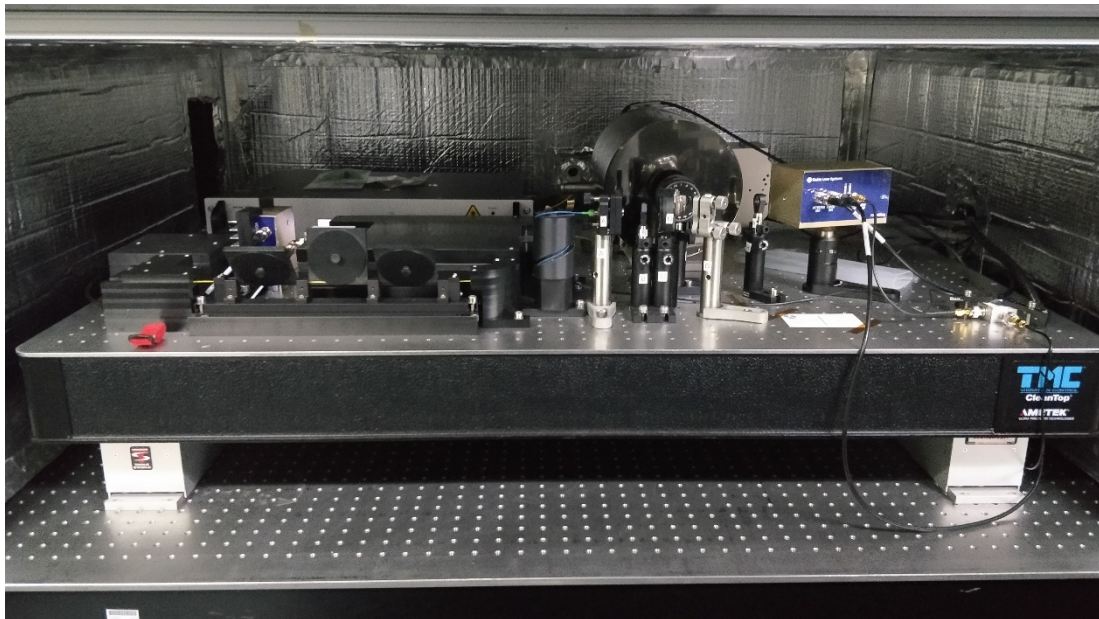


Fig. 3.8 The alignment of the 1762 nm laser.

3.1.3 1762 nm Fiber Laser and 614 nm Diode Laser

The 1762 nm fiber laser is used to shelve one of the $S_{1/2}$ levels to $D_{5/2}$ to enable the fluorescence detection of the qubit states. While the 614 nm laser is used to repump the population from $D_{5/2}$ levels.

The 614 nm laser is actually frequency-doubled from a 1228 nm diode laser with a periodically polarized lithium niobate (PPLN) crystal. The alignment is relatively simple (Fig. 3.7). The laser is locked to the wavelength meter after frequency-doubling.

The 1762 nm laser is a narrow linewidth fiber laser from NKT Photonics. It is locked to an ultra-low expansion (ULE) cavity system made by Stable Laser Systems. The locked linewidth of the laser is around 1 Hz. The alignment is in Fig. 3.8. The stabilized laser output is first amplified by a boosted optical amplifier (BOA) from Thorlabs (module: BOA1082P) before entering the trap. Actually the wavelength is out of the specified range of the module, but it works amazingly well. The power of the laser is amplified from about 15 mW to 75 mW, and the laser power into the trap is around 45 mW, with horizontal polarization to maximize the transition of $\Delta m = 0$. The Rabi frequency of the transition is around 50 kHz. A typical spectrum of the $\Delta m = 0$ quadrupole transition of a single $^{138}\text{Ba}^+$ ion with phonon sidebands is shown in Fig. 3.9.

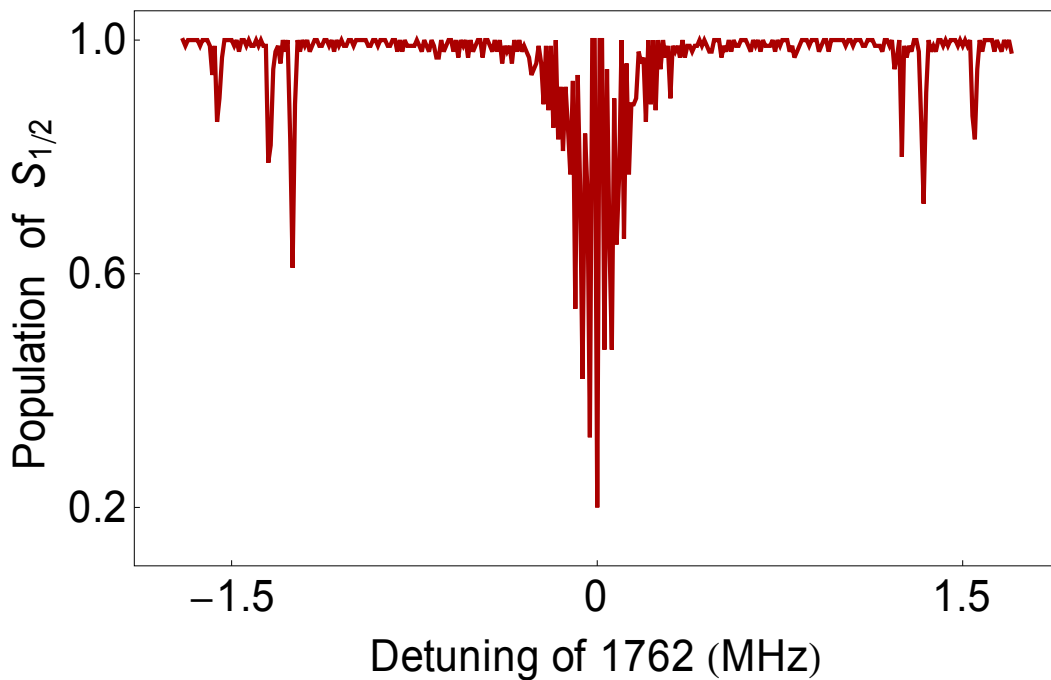


Fig. 3.9 A typical spectrum of the $\Delta m = 0$ quadrupole transition of a single $^{138}\text{Ba}^+$ ion with phonon sidebands.

3.2 Lasers for Stimulated Raman Transitions

3.2.1 Alignment of Raman Lasers

The 355 nm picosecond pulsed laser is used to drive the stimulated Raman transition for the $^{171}\text{Yb}^+$ ion, and 532 nm for the $^{138}\text{Ba}^+$ ion. The two wavelengths are frequency-doubled and tripled from the same 1064 nm pulsed laser. The alignment of the lasers is in Fig. 3.10. The repetition rate of the laser is detected by a fast photodiode (PD) and locked to a rubidium frequency reference. The polarizations of the 532 nm Raman beams are carefully adjusted to be linear. In this case, the AC-Stark shift of $|\downarrow\rangle$ and $|\uparrow\rangle$ caused by each Raman beams are exactly balanced, hence changing the power of the beam will not change the resonant frequencies of the operations. The decoherence caused by the fluctuation of the AC-Stark shift can be minimized in this way.

Usually aligning the Raman beams to the ion is a difficult job. Both beams should hit the ion, the two pulses should arrive at the ion simultaneously and the frequency should be resonant. All these requirements should be met to get the signal of the transition. The common way to align the Raman beams is to place a double-pass AOM in one of the beams to generate a sideband so that the Raman transition can be excited with one beam [19]. However, in this way the uncertainty of the alignment and the resonant frequency is also coupled together. In our system, the Ramsey fringe of 1762 nm transition is used to align the Raman beams. The 1762 nm laser excites the electric quadrupole transition between $|m = 1/2\rangle$ of $S_{1/2}$ and $|m = 1/2\rangle$ of $D_{5/2}$. When 532 nm or 355 nm Raman beams are applied, they introduce AC-Stark shift to both levels, and this can be measured with Ramsey measurement, so the alignment of each of the beams can be optimized by looking at the Ramsey fringes of the 1762 nm transition. In this way, the frequency of the AOM signal is irrelevant, so all the uncertainties of the Raman beams can be addressed one by one.

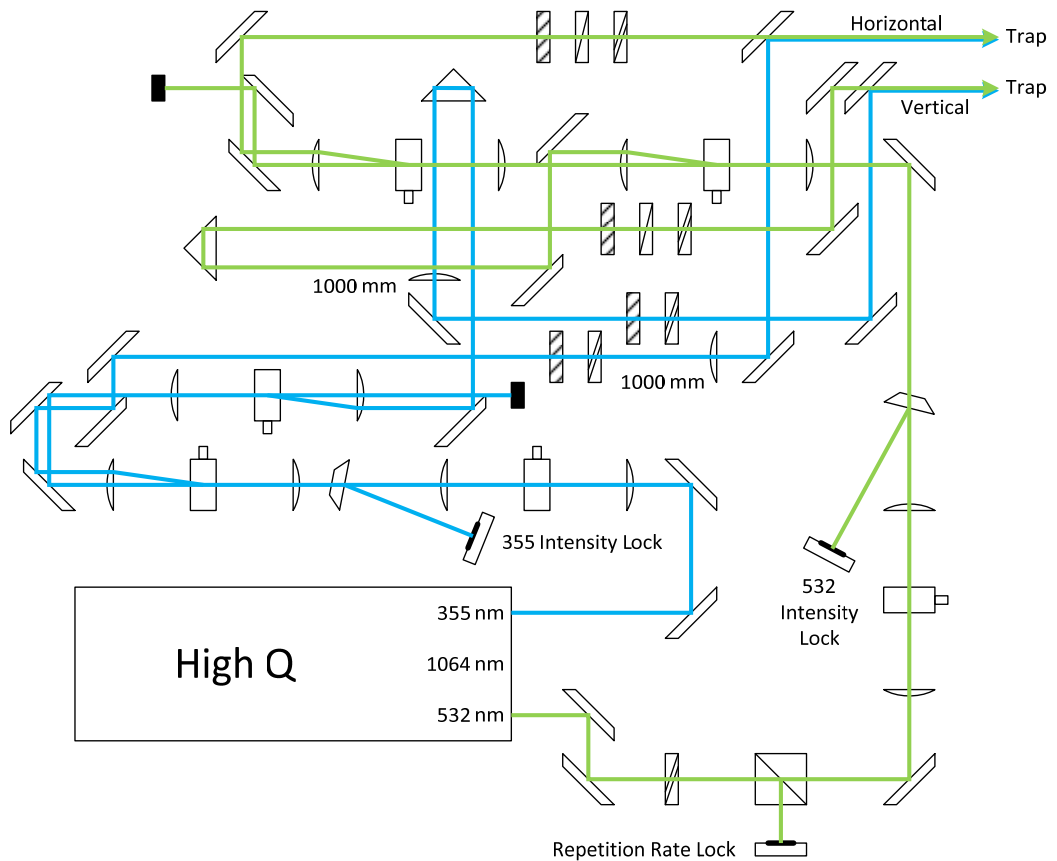
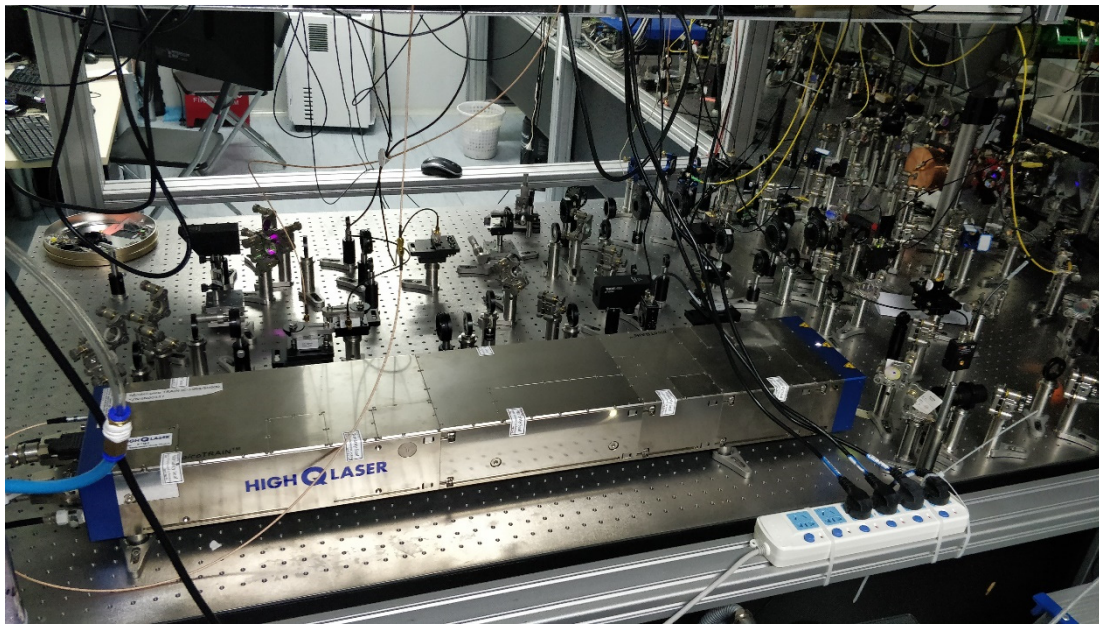


Fig. 3.10 The alignment of the 355 nm and 532nm pulsed lasers. The focal length of all the lenses in this figure is 250 mm, except for the two lenses marked as 1000 mm. These two lenses is used to compensate the focal length difference of the lens near the trap.

3.2.2 Frequency Arrangement of Raman Lasers

Other than the alignment, the driving frequencies of the AOMs for the Raman laser beams also require some consideration.

For the $^{138}\text{Ba}^+$ ion, the situation is the simplest. The qubit we use is the Zeeman qubit, the energy level splitting is just tens of MHz, which can be easily covered by the two AOMs. The pulsed laser is not necessarily required for the $^{138}\text{Ba}^+$ ion, a continuous-wave 532 nm laser will also do. A typical phonon sideband spectrum of two $^{138}\text{Ba}^+$ ions is shown in Fig. 3.11.

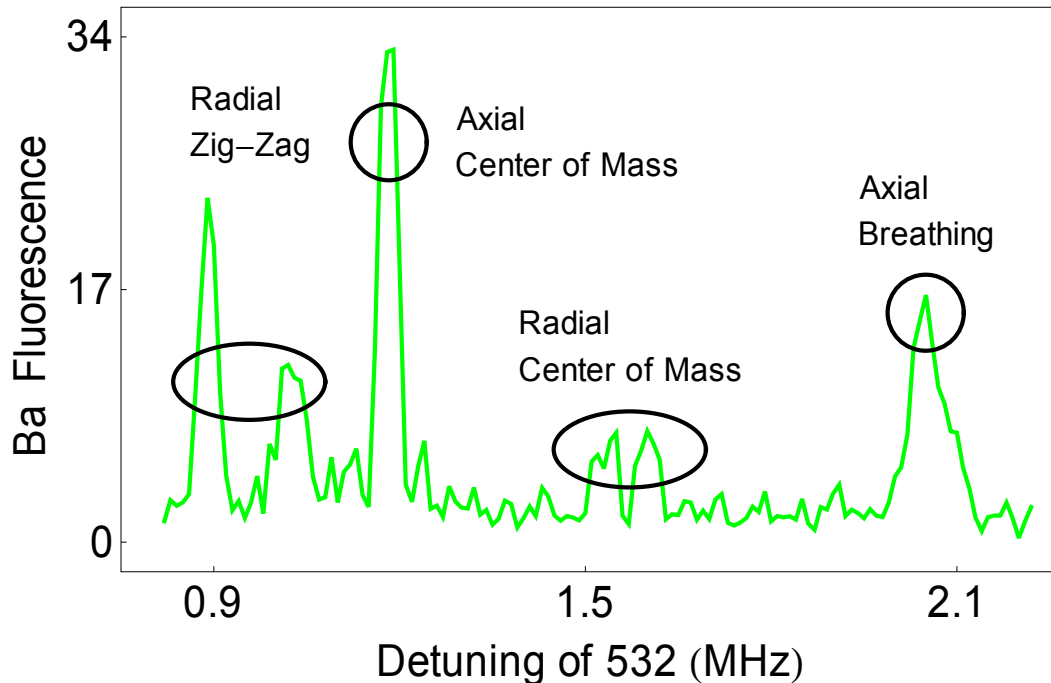


Fig. 3.11 A typical phonon sideband spectrum of two $^{138}\text{Ba}^+$ ions. The detuning is relative to the resonant frequency of the carrier transition.

For the $^{171}\text{Yb}^+$ ion, it is a bit more complicated. The qubit is a hyperfine qubit. The energy splitting is 12.64281212 GHz. This large gap cannot be covered by directly shifting the frequency of the laser beams. Instead, the frequency comb scheme [19] is used. For a pulsed laser, the shape of its spectrum is roughly a “comb” with Gaussian envelope. The span in the frequency domain is the inverse of the pulse width in the time domain, and the distance between neighboring “comb teeth” is the repetition rate of the pulses. So the GHz level energy gap can be covered by each tooth of one beam and another tooth of the other beam with higher order. For our HighQ laser, the pulse width

is around 8 ps, and the repetition rate is around 80 MHz. So this 12 GHz gap can be covered by one tooth and another 158 orders higher one. And the two AOMs just need to cover the remaining frequency difference of tens of MHz. More specifically, if the repetition rate is f_R , the driving frequency difference ω of the two AOMs is

$$\omega = \omega_0 - kf_R, \quad k = \left\lceil \frac{\omega_0}{f_R} \right\rceil, \quad \omega_0 = 12.64281212 \text{ GHz}. \quad (3.1)$$

A typical phonon sideband spectrum of two $^{171}\text{Yb}^+$ ions is shown in Fig. 3.12.

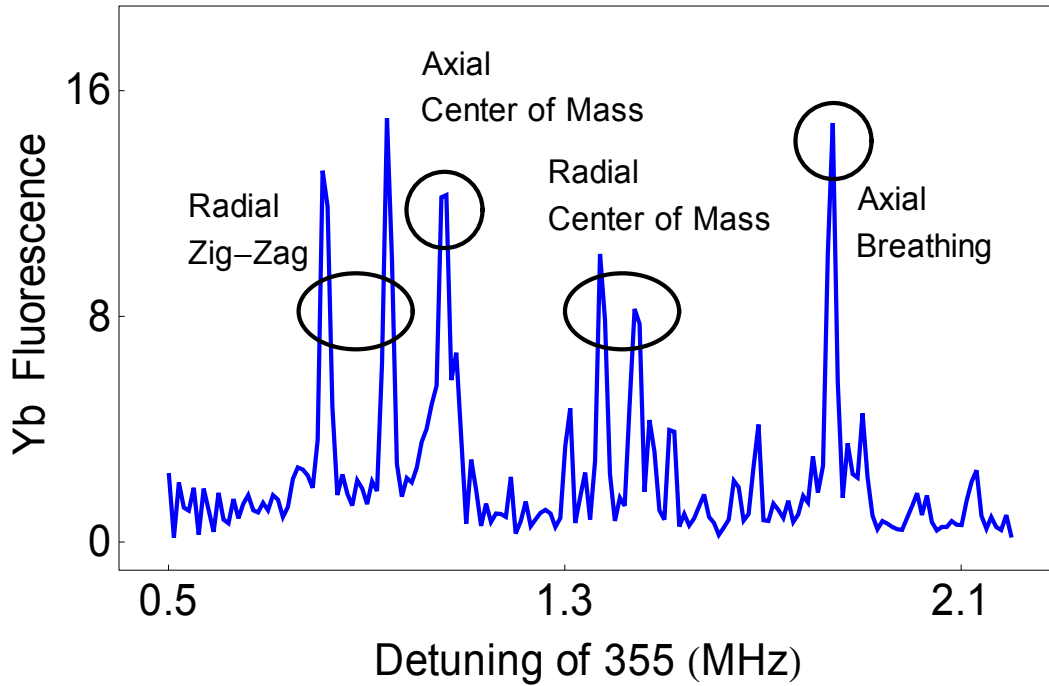


Fig. 3.12 A typical phonon sideband spectrum of two $^{171}\text{Yb}^+$ ions. The detuning is relative to the resonant frequency of the carrier transition.

When the two species of ions are involved at the same time, the problem gets tricky. The polarizations of the 355 nm laser beams cannot be both horizontal or both vertical, or the coupling strength of the Raman transition is effectively zero. So it has to be one horizontal one vertical. For 532 nm laser beams the situation is similar. One beam has to be horizontal to provide π component of polarization, while the other one should be linear and vertical to maximize the coupling strength and minimize the difference of the AC-Stark shift between the qubit levels. So the polarization configurations of both wavelengths are identical, and the detuning is not that large, as shown in Tab. 3.1. This means there will be crosstalk between the ions. An example of such crosstalk effect is shown in Fig. 3.13.

Tab. 3.1 The frequency detuning of the transitions with respect to the lasers.

(THz)	$^{138}\text{Ba}^+$		$^{171}\text{Yb}^+$	
	$S_{1/2} \leftrightarrow P_{1/2}$	$S_{1/2} \leftrightarrow P_{3/2}$	$S_{1/2} \leftrightarrow P_{1/2}$	$S_{1/2} \leftrightarrow P_{3/2}$
355 nm	-237	-186	-33	67
532 nm	44	95	248	348

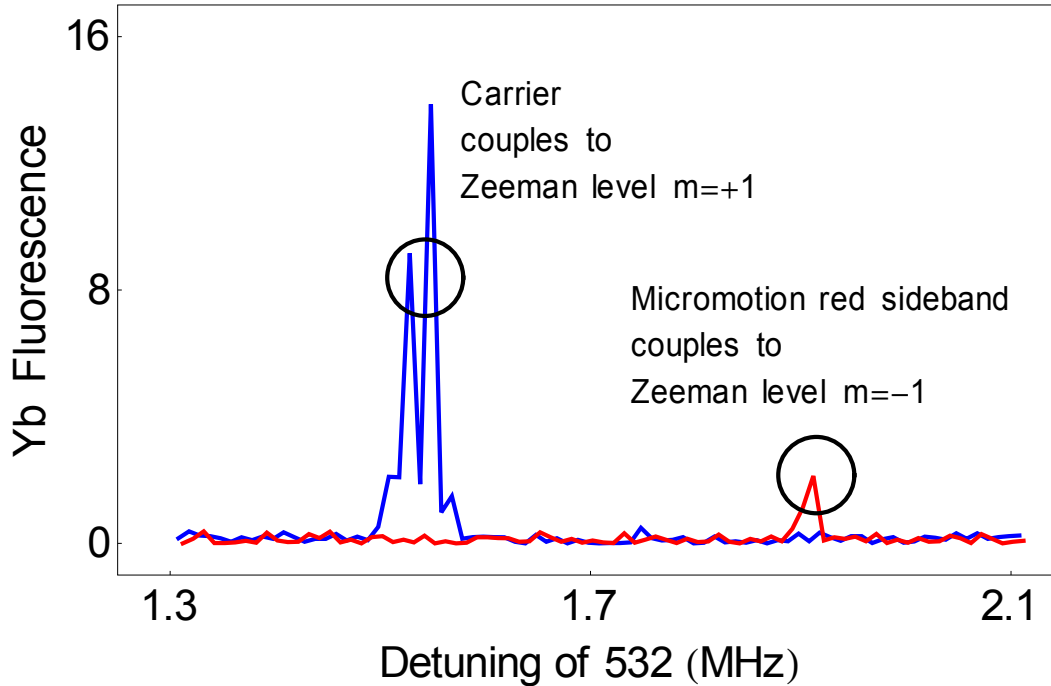


Fig. 3.13 The crosstalk effect of the 532 nm Raman beams to the $^{171}\text{Yb}^+$ ion. The detuning is relative to the resonant frequency of the $^{138}\text{Ba}^+$ ion's carrier transition. The red line is the spectrum to the red side of the carrier transition, so the detuning is actually negative.

So altogether, we have two different wavelengths that are both able to excite the Raman transitions of both ions, each laser has two different frequency components in order to drive the M-S interaction, both lasers have micromotion sidebands, both lasers are symmetric in frequency arrangement (as long as the frequency difference between the two Raman beams is correct, which one has higher frequency is irrelevant), the $^{171}\text{Yb}^+$ ion has Zeeman levels, and both ions have four phonon sidebands of axial modes. And all the unwanted couplings should be avoided in experiment. These are a tedious amount of different frequencies to be analyzed. Some visual aid is required to resolve this frequency mess (Fig. 3.14). The resonant driving frequency of the carrier transition of the $^{171}\text{Yb}^+$ ion is carefully chosen to avoid the excitation of the $^{171}\text{Yb}^+$ ion by the 532 nm laser

(the overlap of the green lines with the red lines in the lower spectrum), the excitation of the Zeeman levels of the $^{171}\text{Yb}^+$ ion by the 355 nm laser's micromotion sidebands (the overlap of the thin blue lines with the red lines in the lower spectrum), and the excitation of the $^{138}\text{Ba}^+$ ion by the 355 nm laser (the overlap of the blue lines with the red lines in the upper spectrum). And then the repetition rate of the pulsed laser is adjusted according to Equ. (3.1). The final frequencies used to implement the M-S interaction is listed in Tab. 3.2.

```

Spec[Clk_] :=
Module[{MM, Zm, Wid, Rect, Lin, BaSpec, YbSpec, L532, L355},
  MM = 12.4; (* Micromotion *)
  Zm = 7.88; (* Zeeman Splitting *)
  Wid = 0.1; (* the "safe distance" around major transitions *)
  BRF = 1.34; (* Breathing Mode Frequency *)

  Rect = Rectangle[{-# - Wid, -1}, {# + Wid, 1}] & /@
    (Abs[# + {-BRF, -BRF/√3, -0.1, 0, 0.1, BRF/√3, BRF}]) &;
  Lin = Rectangle[{-# - 0.1, -1.5}, {# + 0.1, 1.5}] &;
  BaSpec = {Rect[2 Zm]};
  YbSpec = Rect /@ {Clk - Zm, Clk, Clk + Zm};
  L532 = (Lin /@ ({# - MM, # - 0.1, #, # + 0.1, # + MM} & [2 Zm + #])) &;
  L355 = (Lin /@ ({Abs[# - MM], # - 0.1, #, # + 0.1, # + MM} & [Clk + #])) &;
  Grid[{
    {"Ba", Graphics[{Blue, L355[-BRF], L355[0], L355[BRF], Red, BaSpec},
      ImageSize → 500, PlotRange → {{-0.5, 30.5}, {-2, 2}}]},
    {"Yb", Graphics[{Green, L532[-BRF], L532[0], L532[BRF], Blue,
      L355[-BRF], L355[0], L355[BRF], Red, YbSpec}, ImageSize → 500,
      PlotRange → {{-0.5, 30.5}, {-2, 2}}]}]}];
Manipulate[Spec[Clk], {{Clk, 12.2}, 7.5, 35]}

```

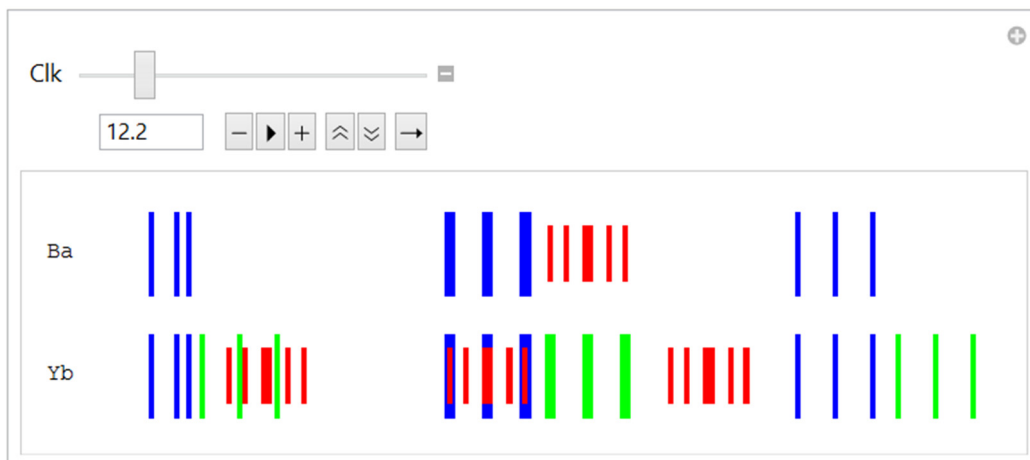


Fig. 3.14 A small tool used to analyze the crosstalk problem and arrange the frequencies.

Tab. 3.2 The final frequencies (in MHz) used to implement the M-S interaction.

Repetition Rate	Carrier Frequency		Sideband Frequency	
	$^{171}\text{Yb}^+$	$^{138}\text{Ba}^+$	Axial Breathing	Axial Center of Mass
80.095	12.2	15.7	1.34	0.774

3.3 Techniques for Alignment

3.3.1 AOM Alignment

Aligning an AOM is one of the starter's practice for students majored in AMO physics experiments. We all know that the input and output beams should be collimated, and the AOM should be on the focus of the beam. But in practice, these standards are usually not well met. If the AOM is located too far away from the focus, the first order beam of different driving frequency may not focus to the same position. This can be a problem if multiple frequencies is required in a single beam to address the ion and the intensity ratios of the different frequency components are important. So here I introduce a procedure which is helpful to align the AOM properly.

- **Step 1.** Place a reference on the laser beam path to mark the position of the beam.
- **Step 2.** Place two plano-convex lenses with the plane side facing each other. Roughly adjust their positions so that the output beam is roughly collimated and pointing at the mark in step 1.
- **Step 3.** Put the AOM roughly at the focus of the beam. Carefully adjust the position of the lenses so that the output beam is as collimated as possible, which can be checked by comparing the spot size right after the lens and several meters away. In this way, the extra length of the beam path introduced by the crystal of the AOM is taken into account.
- **Step 4.** Align the AOM to see the first order of the diffracted beam. Carefully adjust the position of the AOM along the beam so that the zeroth order and the first order are parallel to each other, which can be examined by comparing the distance between the two spots right after the lens and several meters away.
- **Step 5.** Align the AOM to maximize the power of the desired order.

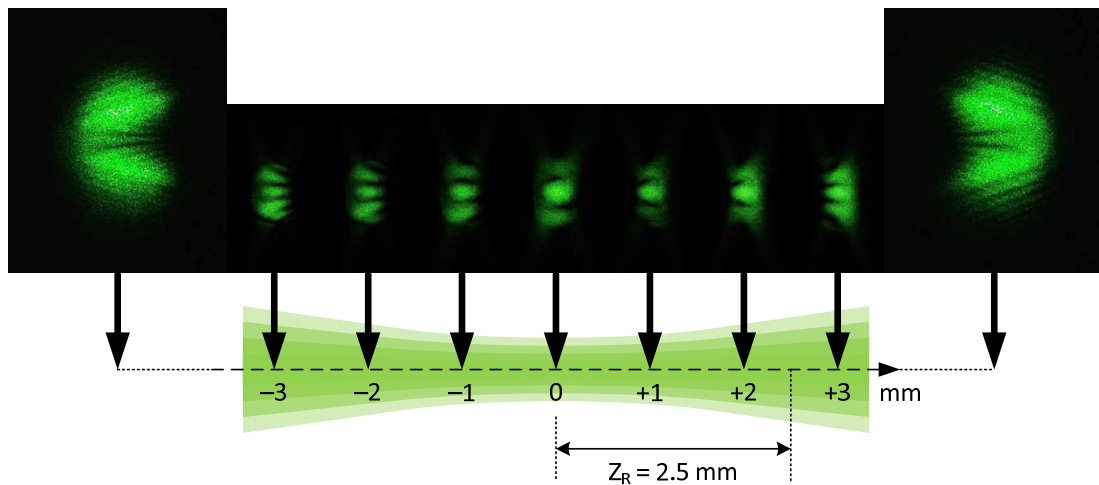


Fig. 3.15 The diffraction patterns of the laser beam hitting a needle tip, with varying position of the needle tip along the axis of the beam. The patterns for positions way before and way behind the focus are also shown. The beam used to demonstrate this and all the following diffraction patterns has Rayleigh length of $z_R = 2.5$ mm, and beam waist $w_0 = 20$ μm .

3.3.2 Diffraction Patterns

Aligning the laser beams into the trap is usually a tricky job. The structure of the trap is frequently used as a reference to put the beam at the geometric center of the trap by steering the beams to hit different parts of the trap. However, “hitting or not” can be a very inaccurate criterion, and it is unable to tell if the beam’s focus is also properly adjusted.

When the laser beam hits an obstacle, it generates diffraction patterns. And actually quite a lot of information can be inferred from the pattern. Take our four-rod trap as an example, the two needle tips of the DC electrodes are often used as the reference to determine the geometric center of the trap. Fig. 3.15 shows the diffraction patterns of the beam hitting a needle tip. The tip is positioned along the axis of the beam, while the distance between the tip and the focus of the beam varies from -3 mm to 3 mm. As can be seen in the figure, if the needle tip is at the focus of the beam, the diffraction pattern is symmetric, and by observing the direction of the pattern, it is able to distinguish whether the tip is before or behind the focus.

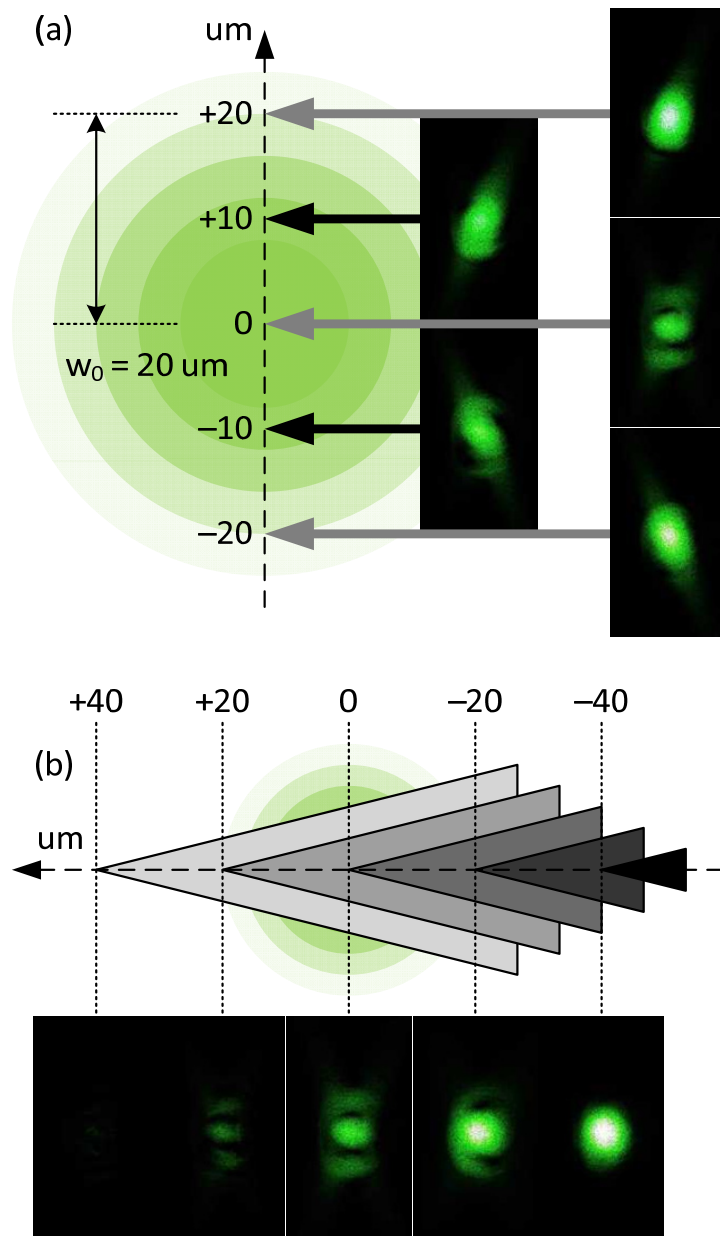


Fig. 3.16 The diffraction patterns of the laser beam hitting a needle tip, with varying position of the needle tip around the focus of the beam.
 (a) The patterns for moving the needle tip vertically. (b) The patterns for moving the tip horizontally.

The diffraction patterns for the positions of the tip around the focus is in Fig. 3.16. If the tip is vertically at the center of the beam, the pattern is symmetric. If it is not, the center of the beam is mainly blocked by one edge of the needle, and hence the pattern is perpendicular to the edge. In this way, the relative position of the tip and the center of the beam can be determined. While the horizontal position is relatively hard to determine, the brightness of the pattern can be used as a reference.

The diffraction patterns of the needle is useful when you try to align multiple beams into the trap and make sure their focuses are at the same position.

Another frequently used component is the pinhole. The pinhole can be used in 4-F system as a spacial filter to block unwanted scatterings. It can also be used as a reference of the position of the beam. The diffraction patterns of the pinhole have similar properties. As shown in Fig. 3.17(a), the symmetry of the pattern can be used to determine whether the pinhole is at the focus of the beam. While the patterns in Fig. 3.17(b) can be used to determine which part of the pinhole is blocking the beam. The direction of the pattern is perpendicular to the tangent of the edge. This is useful if you want to overlap multiple beams at the position of the pinhole.

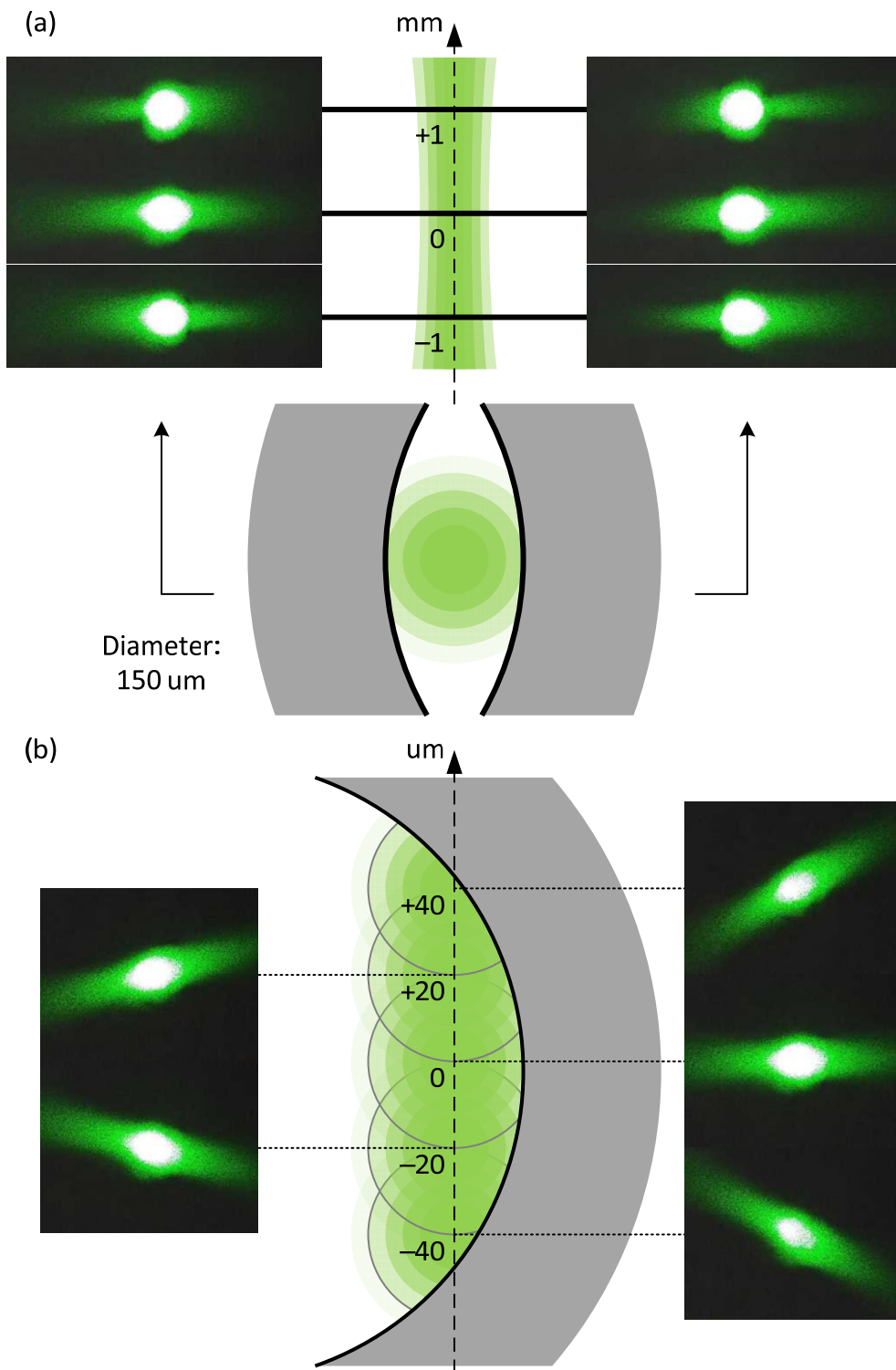


Fig. 3.17 The diffraction patterns of the laser beam hitting a pinhole with a diameter of 150 μm .

(a) The patterns when the beam is cut by left and right edges of the pinhole with varying position along the beam axis. (b) The patterns when the beam is cut by different part of the pinhole.

Chapter 4 Pulse Sequencer

4.1 Function and Performance Goals

A successful experiment requires coordinated operation of all the lasers, signal generators and detectors. There are logically complicated tasks like generating the control signal according to the experiment parameters. There are also logically simple but timing critical tasks like switching the signals on and off with microsecond timing precision. A typical experiment flow of our system is shown in Fig. 4.1 as an example. Usually, the complicated tasks are assign to a computer, while the timing critical tasks are handled by FPGA boards.

In our system, an FPGA based TTL pulse sequencer is implemented to fulfill these tasks. As the name suggests, a TTL pulse sequencer is able to generate TTL pulse sequences as instructed by the computer with high timing resolution (Fig. 4.2). The control structure of our system is shown in Fig. 4.3. The instructions to the signal generators and the pulse sequencer are issued by the computer, while the pulse sequencer schedules the execution of the experiment flow. The performance of the sequencer should fulfill the following requirements.

- The number of channels should be large enough to control all the related apparatus.
- The timing resolution should be as high as possible to minimize the infidelity of quantum operations due to timing errors.
- The maximum duration of timing should be long enough for demanding experiments.

As an example, the most demanding experiment our system has performed is to demonstrate the coherence time of $^{171}\text{Yb}^+$ qubit exceeding 10 minutes [31]. This experiment has sequences as long as 10 minutes while the π -time of microwave operations is as short as 10us.

The newest version of our pulse sequencer is made with an Altera Cyclone III EP3C25Q240C8 FPGA chip. Its performance is shown in Tab. 4.1.

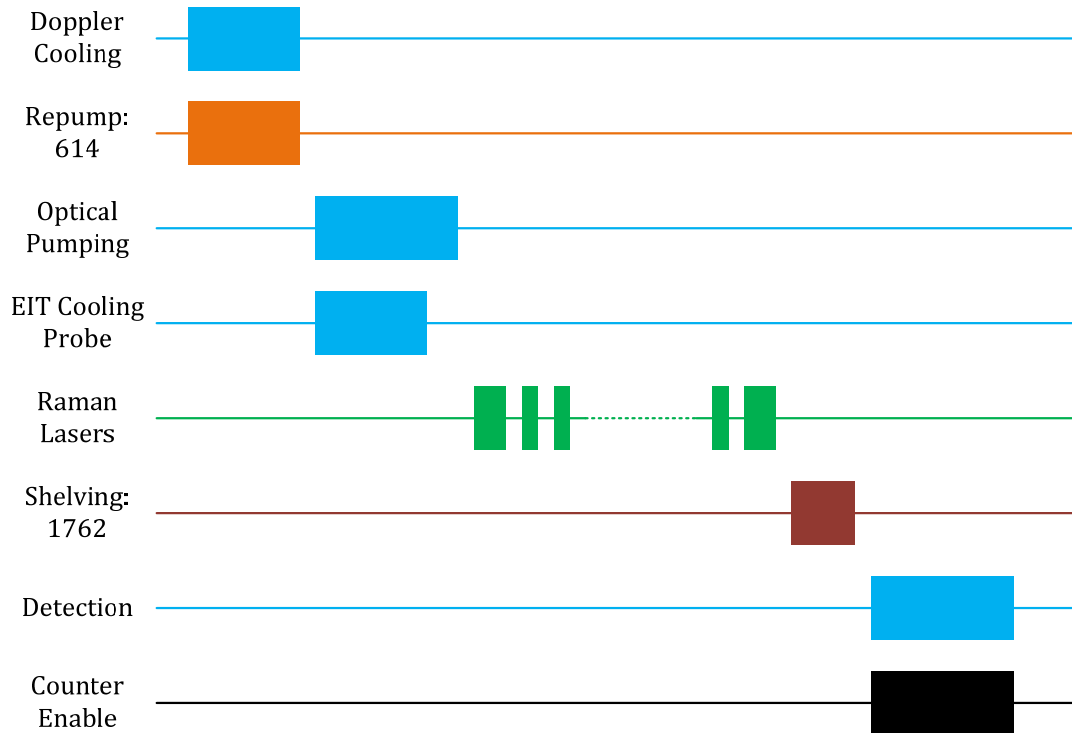


Fig. 4.1 A typical pulse sequence in experiment.

Tab. 4.1 The Performance of the pulse sequencer.

Clock Frequency	200 MHz
Timing Resolution	5 ns
Minimum Segment Duration	5 ns
Maximum Segment Duration	$5 * 2^{41}$ ns \approx 3.05 hours
Output Channels	32
Maximum Number of Segments	7680
Maximum Repetition of Sequence	$2^{24} - 1 = 16777215$
Other Functions	<p>External Trigger: The sequencer can be configured to synchronize the sequence with an external trigger. This function can be used to compensate the 50 Hz noise induced by AC lines.</p> <p>Embedded Gated Counter: Four 32-bit counters are also built into the chip that can be used to count the fluorescence photons collected by the PMT.</p>

Pulse Sequencer

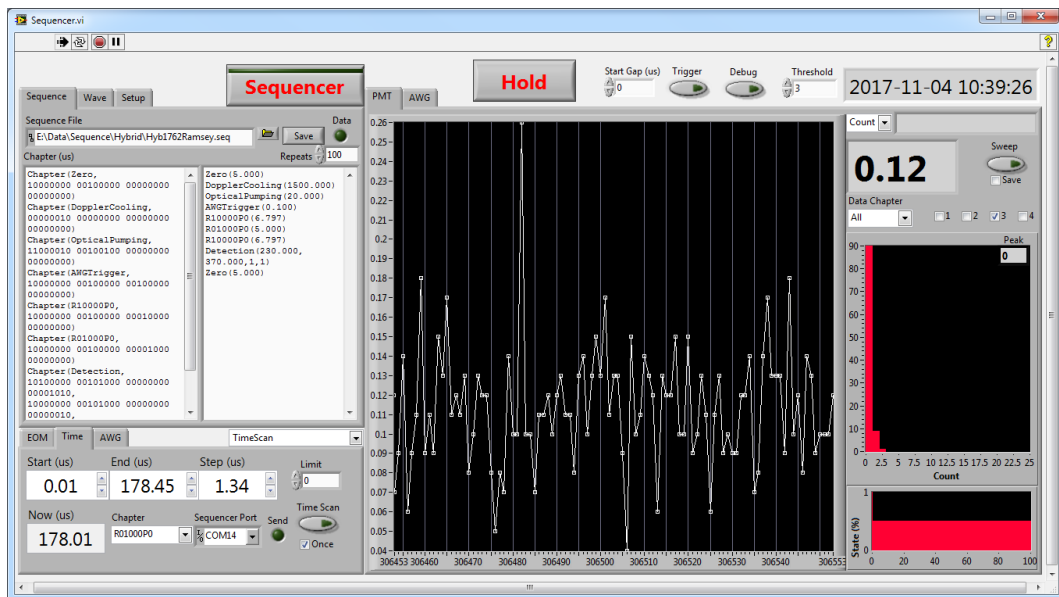


Fig. 4.2 The TTL pulse sequencer of our system and its user interface.

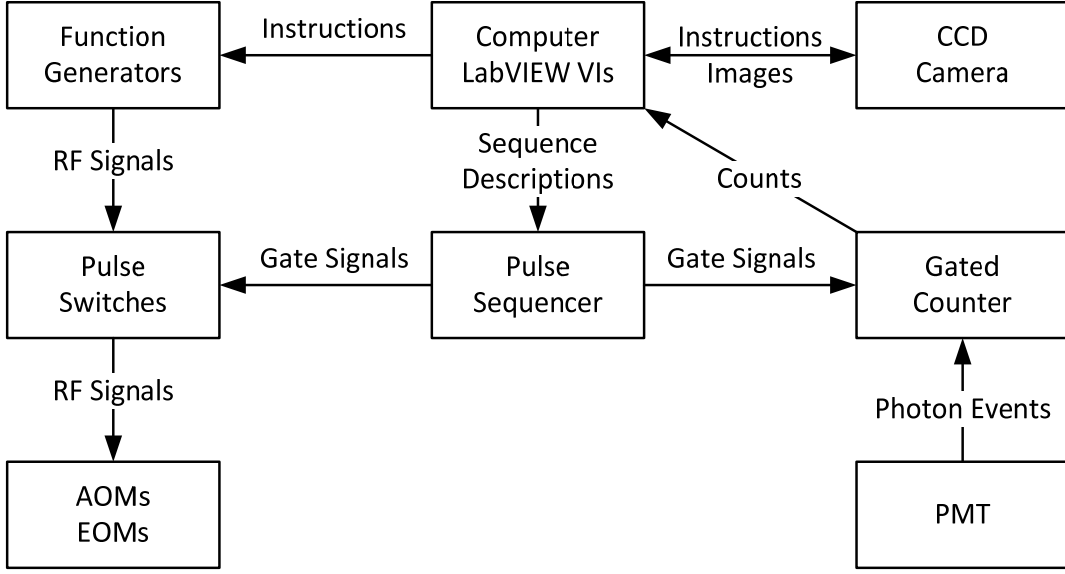


Fig. 4.3 The control structure of our system.

4.2 Pipeline Timer and Time Stamp Encoding

Unlike the arbitrary waveform generator (AWG), which generates the output by continuously pushing amplitude data of each sample point into the digital-to-analog converter (DAC), the sequencer generates the output discretely so that memory space has less limitation on the maximum duration of the sequence. Obviously, a TTL sequence can be decomposed into a number of segments, during which the levels of all the output channels hold unchanged. So a sequence can be defined by a list, whose each element contains the duration and output levels of each segment. In this way, the sequencer just need to count the time and change the output when a new segment starts. So the performance of the sequencer is determined by its timer module.

A timer is basically a counter T that counts the clock cycles. More specifically, for each rising edge of the clock signal,

$$T_t[0] = T_{t-1}[0] \oplus 1, \quad T_t[i] = T_{t-1}[i] \oplus \bigwedge_{j=0}^{i-1} T_{t-1}[j], \quad (5.1)$$

in which $T_t[i]$ denotes the i -th bit of T on clock cycle t . Note that $T_t[i]$ is computed through a chain of AND operation. For large i , this could take a considerably long time, limiting the clock frequency. So it seems that high timing resolution and long timing duration is mutually exclusive. However, rather than computing the whole combinatorial

logic chain in one clock cycle, it can be arranged in a pipeline manner,

$$\begin{aligned} T_t[i] &= T_{t-1}[i] \oplus C_{t-1}[i] \\ C_t[i] &= T_{t-1}[i-1] \wedge C_{t-1}[i-1], \quad C_t[0] = 1, \end{aligned} \quad (5.2)$$

in which $C[i]$ is the carry bit of $T[i]$. In this way, the clock frequency is no longer limited by the bit width of the timer, but in order to use this type of timer, a bit more analysis of its behavior is required.

From Equ. (5.2), it is easy to see that the carry propagates one bit further per clock cycle, so if we start with $T_0 = 0$, $C_0 = 1$ and look at $S_t = \{T_t[i], T_{t-1}[i-1], \dots, T_{t-i}[0]\}$, it is just the binary sequence we have for ordinary timer, 0, 1, 10, 11, 100 etc., as illustrated in Fig. 4.4. So generally

$$T_t[i] = (t - i)[i], \quad (5.3)$$

i.e., the i -th bit of number $t - i$. And similarly,

$$C_t[i] = \bigwedge_{j=1}^i T_{t-j}[i-j]. \quad (5.4)$$

t	C_t	T_t	S_t
0	0 0 0 1	0 0 0 0	0 0 0 0
1	0 0 0 1	0 0 0 1	0 0 0 1
2	0 0 1 1	0 0 0 0	0 0 1 0
3	0 0 0 1	0 0 1 1	0 0 1 1
4	0 0 1 1	0 0 1 0	0 1 0 0
5	0 1 0 1	0 0 0 1	0 1 0 1
6	0 0 1 1	0 1 0 0	0 1 1 0
7	0 0 0 1	0 1 1 1	0 1 1 1
8	0 0 1 1	0 1 1 0	1 0 0 0
9	0 1 0 1	0 1 0 1
10	1 0 1 1	0 0 0 0	
11	0 0 0 1	1 0 1 1	
...	

Fig. 4.4 The states of the T and C register of the pipeline timer.

Usually, the function of a timer is that when a specific number of clock cycles elapsed, it assert some signal. So it would be convenient if we set T and C to some initial value T^* and C^* so that after the specified number of cycles, the highest bit of T flips to 1. Keep to the previous example, we see that $T[3]$ flips to 1 on cycle 11.

According to Equ. (5.3), for a timer T of $W + 1$ bits, $T_t[W]$ first flips to 1 when

$$t^* = 2^W + W. \quad (5.5)$$

So if we set $T^* = T_{t^*-n}$ and $C^* = C_{t^*-n}$, then after n cycles the signal will be asserted.

The value of T^* and C^* can be computed by the computer and sent to the sequencer as time stamp of each sequence segment so that the sequencer can use them directly. However, from Equ. (5.4), we can see that in fact C^* can be computed from T^* and if this computation can be performed on the chip, it would reduce the memory consumption by half. Note that $T_t[i]$ flips if and only if $t = k * 2^i + i$ and these are the cycles that $C_{t-1}[i] = 1$. So $C^*[i] = 1$ if and only if

$$T^*[j] = T_{2^{i+j}-1}[j] \text{ for all } j < i. \quad (5.6)$$

This is also a combinatorial logic chain and can take quite long time. However, this computation is only required when a new segment is about to start. So we can arrange an arbiter module and several parallel lines to distribute this computation among multiple clock cycles and effectively the computation is finished in one clock cycle. With this pipeline configuration of the timer, the timing resolution is no longer limited by the bit width of the timer.

4.3 Structure of the Pulse Sequencer

A pulse sequencer requires supporting modules other than the timer to fulfill the task. The structure and signal flow of the pulse sequencer is depicted in Fig. 4.5.

The input dispatcher module is used to decode the instructions sent from the computer via a USB port. When a new transfer session is initiated by the computer, the input dispatcher module notifies the controller to halt the execution of current sequence and switch to the receiving state until the last instruction package is received. The received control parameters are sent to the controller and the descriptions of the segments are sent to the first-in-first-out (FIFO) array to be stored.

The controller module is used to control the state of the sequencer. When an instruction transfer session is initiated, it disables the timer and reset the address pointers of the FIFO array. The controller also counts the number of repetitions of current sequence. If the external trigger is enabled, the controller hold the sequencer and wait a trigger when an execution of the sequence is finished.

The FIFO array consists of five FIFO queues. It stores the TTL levels and time stamp of each segment and also calculate the initial values of carry bits from the time stamp. The segments are cyclically distributed among five parallel queues by an input arbiter during the transfer of a new sequence. Each time the “Tick” signal is asserted by the timer module, marking an end of current segment, the time stamp, the TTL levels and the carry bits are read from one of the five queues and that queue immediately initiates the calculation of the carry bits of the next segment stored in it. The output arbiter is used to arrange the order of output of the five queues. The FIFO array is designed in this parallel manner so that the time consuming calculation of the carry bits is effectively distributed among five clock cycles.

The timer module is as discussed in the last section. When a segment is over, it asserts a one clock cycle high pulse of “Tick” signal to inform the FIFO array and the output ports to act.

The output ports changes their levels when “Tick” signal is asserted, and are disabled during the initialization.

The complete Verilog source code of the pulse sequencer is in Appendix A.

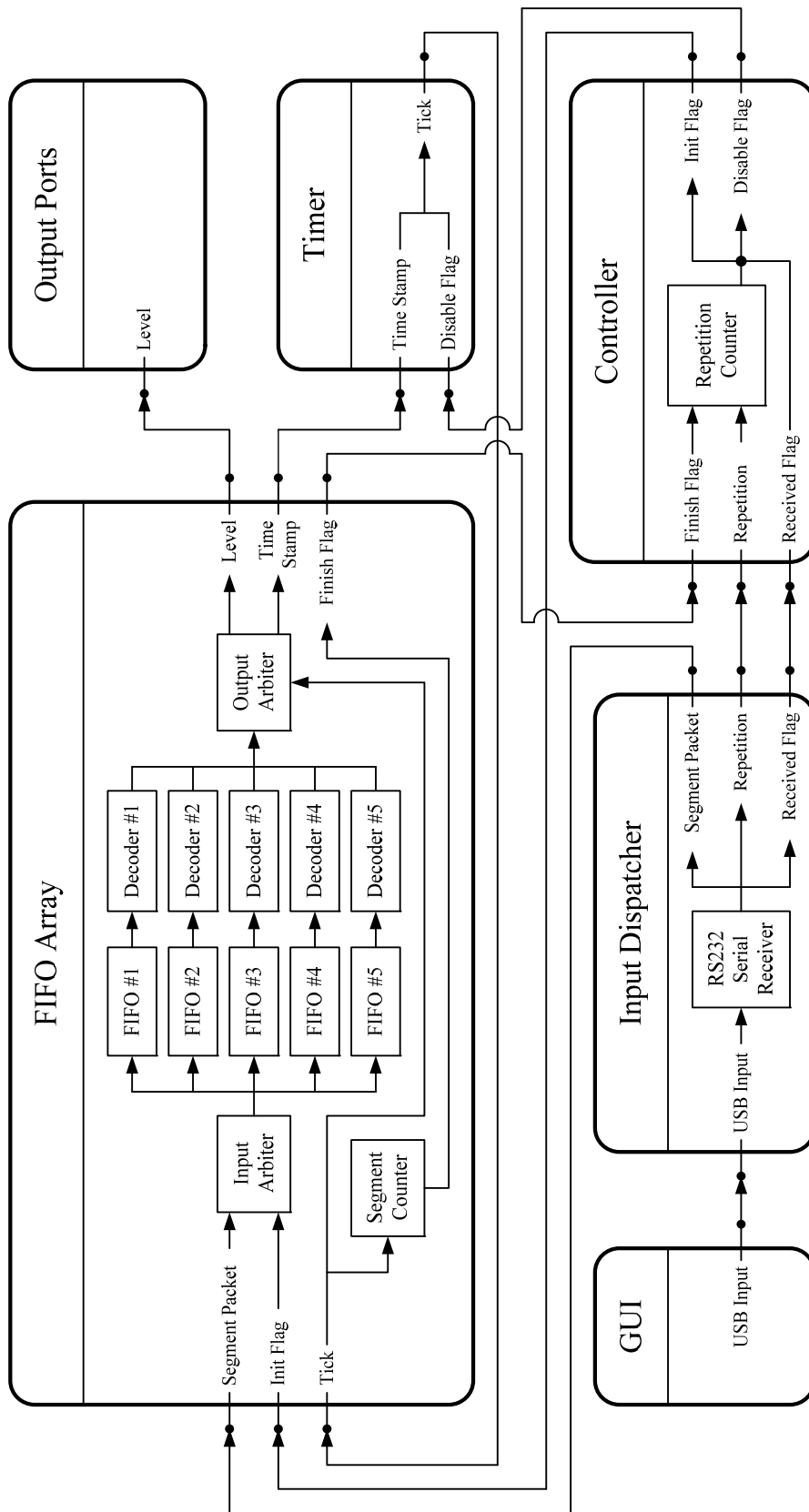


Fig. 4.5 The module structure and signal flow of the pulse sequencer.

Chapter 5 Geometric Landau-Zener-Stückelberg Interferometry

5.1 Introduction

The Landau-Zener (LZ) transition or Landau-Zener-Stückelberg (LZS) interferometry together with Rabi oscillation have been widely used to coherently control various quantum systems, including atomic or optical systems [32] [33], quantum dots [34] [35], superconducting qubits [36], nitrogen-vacancy-center systems [37], and spin transistors [38]. Related to the Rabi operation, composite pulses associated with dynamical decoupling [39] [40] or adiabatic manipulation with geometric phases [41] [42] have been extensively studied to reach error rates below the fault-tolerant level with reasonable limitations of control in feasible physical systems.

Generally, a quantum system subjected to adiabatic driving acquires a geometric phase (or Berry phase) as well as a dynamic phase. Unlike the dynamic phase, the geometric phase depends solely on the trajectory of the parameters in the Hamiltonian, and thus is stable against certain types of fluctuations; this has been experimentally observed in various systems [43] [44]. Composite-pulse schemes also have a geometric phase interpretation in nonadiabatic regimes [45]. However, the geometric phase and robust control in the context of LZ interferometry have not yet been experimentally investigated and demonstrated [46].

This project is an experimental realization of LZS interferometry controlled exclusively by the geometric phase. It is inspired by the proposal of Ref. [46] in a single trapped-ion system, which is capable of simulating other qubit systems. Although the original proposal is specifically for a superconducting system, I apply the scheme to a trapped-ion system and observe the robustness of the geometric phase against very great operational errors in all possible control parameters by artificially introducing noise into the system. The demonstrated strong immunity sheds light on the possibility of examining the geometric phase in more complex systems which might be subject to large fluctuations in control parameters.

5.2 Landau-Zener Transition

The LZ Transition happens in a quantum two level system described by Hamiltonian

$$\begin{aligned} H(t) &= \frac{\hbar}{2} \boldsymbol{\sigma} \cdot \mathbf{B}_{\text{eff}}(t), \quad \boldsymbol{\sigma} = (\sigma_x, \sigma_y, \sigma_z), \\ \mathbf{B}_{\text{eff}}(t) &= (\Omega(t) \cos \varphi, \Omega(t) \sin \varphi, \Delta(t)), \end{aligned} \quad (5.1)$$

when the system is driven through an avoided crossing where Δ is at minimum. According to the adiabatic-impulse approach, the transition is considered to happen only in a small vicinity around the avoided crossing, while the rest of the driving is adiabatic. In this way, the transition probability in the adiabatic basis $\{|\psi_-\rangle, |\psi_+\rangle\}$ is characterized by

$$P_{\text{LZ}} = \exp\left(-\frac{\pi \Delta_0^2}{2|v|}\right), \quad (5.2)$$

where $v = \left. \frac{d\Omega}{dt} \right|_{\Omega=0}$ and Δ_0 is the energy splitting at the avoided crossing. The transition is described by the time evolution operator $U_{\text{LZ}} = U_a N U_b$ with

$$N = \begin{pmatrix} e^{-i\varphi_S} \sqrt{1-P_{\text{LZ}}} & -\sqrt{P_{\text{LZ}}} \\ \sqrt{P_{\text{LZ}}} & e^{i\varphi_S} \sqrt{1-P_{\text{LZ}}} \end{pmatrix}, \quad (5.3)$$

where φ_S is the Stokes phase [47] and $U_{a(b)} = \exp(i\xi_{a(b)}\sigma_z)$ is the operator for dynamic phase $\xi_{a(b)}$ accumulated after (before) the avoided crossing.

In experiment, the hyperfine levels of the ground state of an $^{171}\text{Yb}^+$ ion is used as the two level system, and the control of the B_{eff} is implemented with microwave, as is mentioned in Chapter 2 of this thesis. The transition probability and transition dynamics is verified and observed for different speed of driving, as shown in Fig. 5.1.

5.3 Adiabatic Passage

In order to perform the LZ transition, the system should first be prepared in the eigenstate of the Hamiltonian, Equ. (5.1), with $\Omega \gg \Delta$. In this experiment, the state is prepared using adiabatic passage with

$$\begin{aligned} \Omega(t) &= B \sin \omega t, \quad \Delta(t) = B \cos \omega t, \\ B &= (2\pi)50 \text{ kHz} = |\mathbf{B}_{\text{eff}}|, \quad \omega = \frac{\pi}{200 \mu\text{s}}. \end{aligned} \quad (5.4)$$

To put it more intuitively, the effective magnetic field \mathbf{B}_{eff} just rotates around an axis on the equatorial plane with constant angular velocity ω and amplitude B . This is a simple

way to drive the system and yet with pretty good adiabaticity. The simulated trajectories of the system under such driving and the experiment verification is shown in Fig. 5.2.

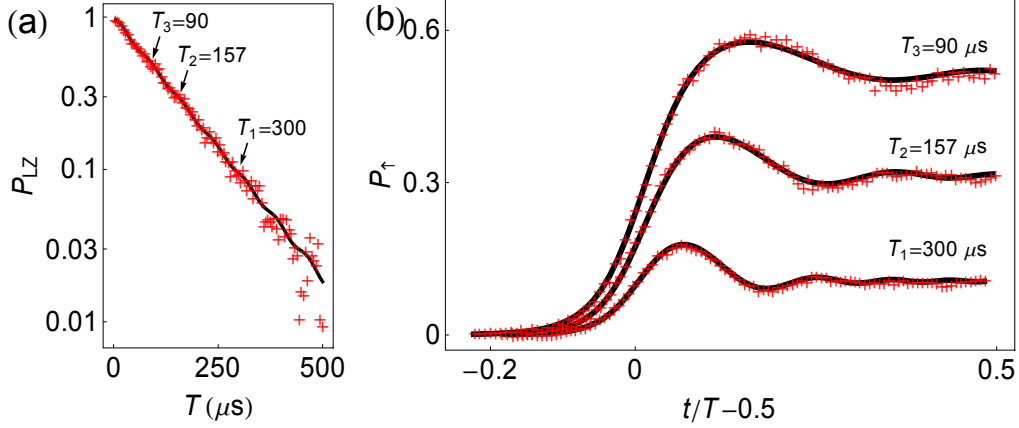


Fig. 5.1 The transition probability and dynamics of the Landau-Zener transition. (a) LZ transition probability P_{LZ} as a function of the total driving time T of linear sweep of Ω from $(2\pi)49.24$ kHz to $-(2\pi)49.24$ kHz with $\Delta_0 = (2\pi)8.68$ kHz. The red crosses in the figure are data points and the black curves are numerical simulation results. (b) The LZ transition dynamics for three exemplary cases, $T = 90 \mu\text{s}$, $157 \mu\text{s}$, $300 \mu\text{s}$, which provide tunneling probabilities of 0.5, 0.3, and 0.1 after the transitions. Oscillatory behaviors near the avoided crossing [37] [48] are clearly observed and precisely in agreement with the results of the numerical simulation.

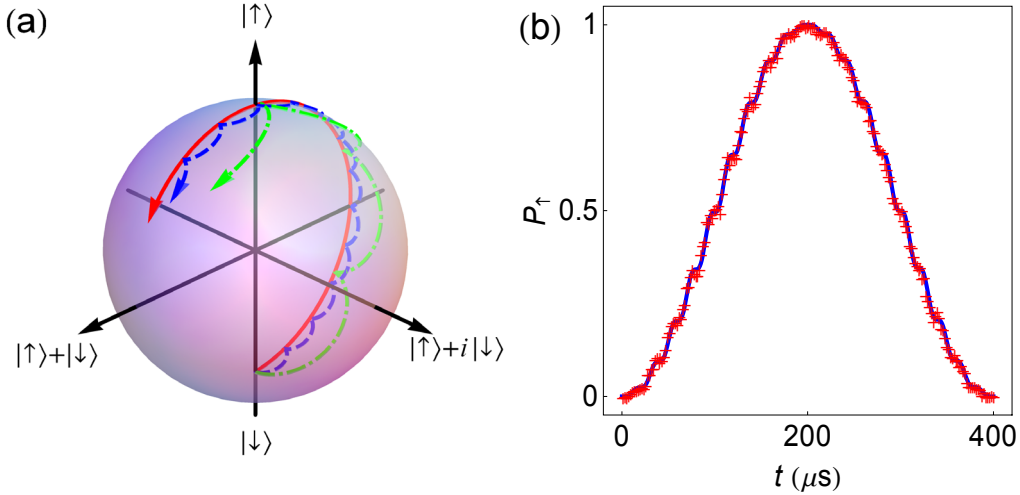


Fig. 5.2 The adiabatic passage. (a) The trajectories of the system under adiabatic evolutions of different ω , with the green one $\omega = \pi/(200 \mu\text{s})$, the blue one $\omega = \pi/(60 \mu\text{s})$ and the red one $\omega \rightarrow 0$. (b) The population of the $|\uparrow\rangle$ state during the adiabatic evolution with $\omega = \pi/(200 \mu\text{s})$.

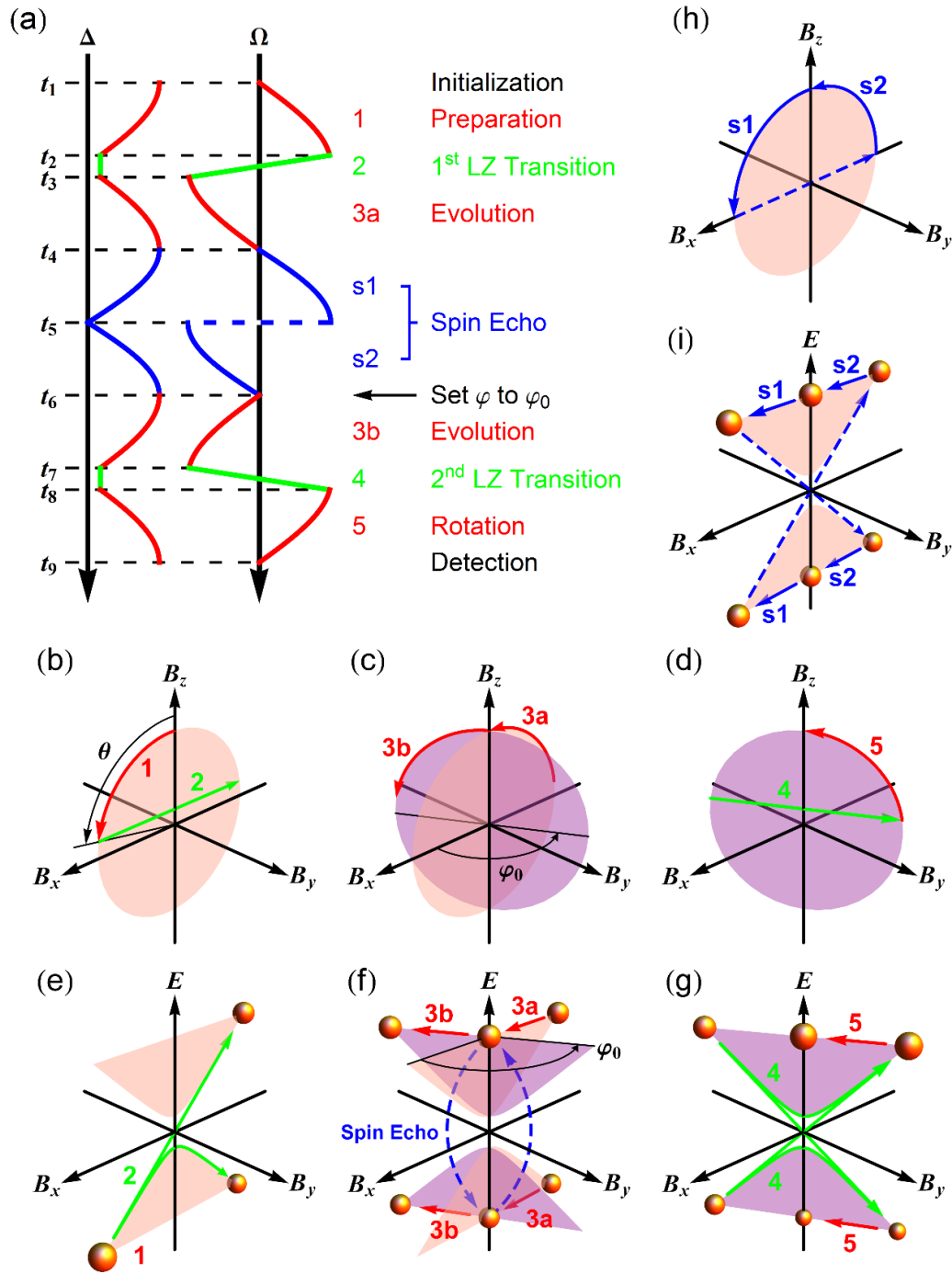


Fig. 5.3 The procedure of a LZS interferometry.

(a) The control sequences of Ω and Δ in $\mathbf{B}_{\text{eff}} = (\Omega \cos \varphi, \Omega \sin \varphi, \Delta)$ for the realization of geometric LZS interferometry. The coloring and numbering of the stages are the same in (b) – (i). (b) – (d) The trajectories of \mathbf{B}_{eff} during the operation in (B_x, B_y, B_z) space. (e) – (g) The evolution of the system in (B_x, B_y, E) space, where the hyperbolic curves indicate the energy of the adiabatic eigenstates. In contrast to the standard energy diagram for the LZ transition, the geometric LZS interferometer should be illustrated in 3-D due to the phase information. The volume of the orange spheres corresponds to the population of the adiabatic eigenstates. (h), (i) The trajectories of \mathbf{B}_{eff} and the system for the adiabatic spin-echo sequences.

5.4 Geometric Landau-Zener-Stückelberg Interferometry

The interference of the two adiabatic eigenstates takes place when two LZ transitions happen successively, similar to the Mach-Zehnder interferometry. In this experiment, the interference fringes are solely determined by the geometric phase acquired between the LZ transitions, while the dynamic phase is cancelled out by the symmetric arrangement of the experiment sequence with a spin-echo stage in the middle.

The complete sequence of the interferometry is shown in Fig. 5.3. The system is first adiabatically prepared for the LZ transition in stage 1 with Equ. (5.4), as is the same in stage 3a, 3b, s1, s2 and 5. Then the system is driven through the first LZ transition by linearly sweeping the value of Ω , as shown in Fig. 5.3(b)(e). The geometric phase is acquired in stage 3 with adiabatic driving and phase change φ_0 of the control parameter [Fig. 5.3(c)(f)]. And finally the second LZ transition which is identical to the first one is performed to complete the interferometry [Fig. 5.3(d)(g)]. In order to make the phase of the interferometry purely geometric, a spin-echo sequence that swaps the two adiabatic eigenstates is performed right in the middle of stage 3 [Fig. 5.3(h)(i)], so that for each adiabatic eigenstate, the dynamic phase and Stokes phase gained during the adiabatic evolution and the LZ transition in the first half of the experiment sequence exactly cancelled out with that of the second half.

5.5 Robustness of the Interferometry

With Equ. (5.3), it is easy to calculate the population of the $|\uparrow\rangle$ state,

$$P_{\uparrow} = P_{LZ}^2 + (1 - P_{LZ})^2 - 2P_{LZ}(1 - P_{LZ}) \cos \varphi_0. \quad (5.5)$$

In the experiment, we set P_{LZ} to $1/2$, so in this case

$$P_{\uparrow} = \frac{1 - \cos \varphi_0}{2}. \quad (5.6)$$

One cycle of the interference fringes is demonstrated in Fig. 5.4(a).

The robustness of the contrast of the interference fringes against the deviations of the control parameters is also experimentally tested by artificially introducing errors into the parameters. For the strength of the driving field, we assume a scaling error,

$$\Omega' = (1 + \epsilon)\Omega, \quad (5.7)$$

simulating the case of an inhomogeneous driving field. While for the driving frequency,

we assume a bias error in the unit of the energy splitting at the avoided crossing,

$$\Delta' = \Delta + \delta\Delta_0. \quad (5.8)$$

Both kinds of errors are assumed to be slow enough so that in each run of the experiment sequence, the values of ϵ and δ hold the same. The experiment test of the robustness is performed by randomly choosing 1139 pairs of $\{\epsilon, \delta\}$ in the range of $-0.5 \leq \epsilon \leq 0.5$, $-0.3 \leq \delta \leq 0.3$ and measure the value of $1 - P_{\uparrow}(\varphi_0 = 0)$ for each pair. The experiment result is shown in Fig. 5.4(b), and the corresponding numerical simulation result is in Fig. 5.4(c).

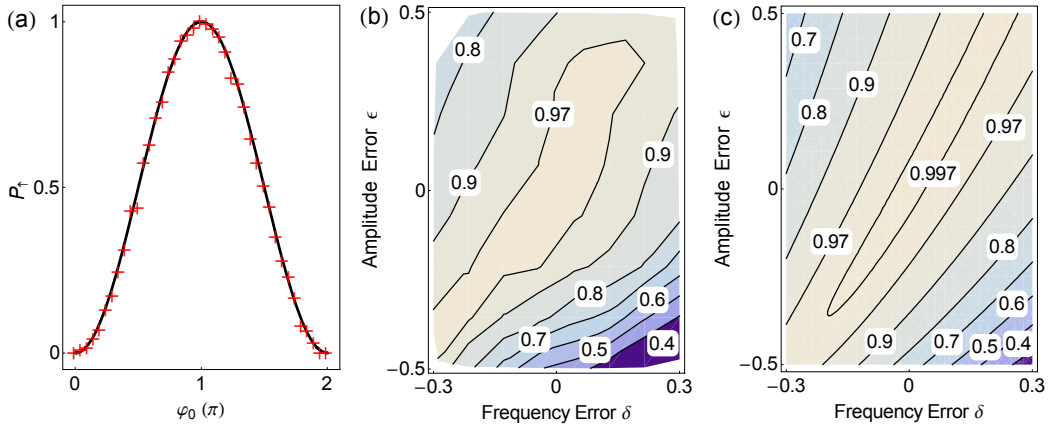


Fig. 5.4 The interference fringe and its robustness of the geometric LZS interferometry. (a) The interference fringe. (b) The experiment result of the robustness test. (c) The numerical simulation result.

Chapter 6 Arithmetic Operations of Phonons

6.1 Introduction

In quantum mechanics, bosonic creation \hat{a}^\dagger and annihilation \hat{a} operators bear the following operator relations,

$$\hat{a}^\dagger = \sum_{n=0} \sqrt{n+1} |n+1\rangle\langle n|, \quad \hat{a} = \sum_{n=0} \sqrt{n} |n-1\rangle\langle n|, \quad (6.1)$$

where $|n\rangle$ stands for a Fock state of n bosons. The proportionality factors $\sqrt{n+1}$ and \sqrt{n} appear due to the symmetric indistinguishable nature of bosons. Thus, the addition or subtraction in quantum domain involves the modification of the probability amplitude of state due to the excitation n -dependent factor. The bosonic annihilation and creation operations have been proposed to be a building block to generate an arbitrary quantum state [49], to distill entanglement or non-locality [50] and to transform a classical state to a nonclassical state [51]. In recent times, there have been seminal works to realize the bosonic operations at the single-boson level for the test of foundations and applications of quantum mechanics [52] [53] [54] [55] [56] [57]. However, such bosonic operations are not trace preserving and inherently probabilistic. The probability of success has so far been extremely low in their implementation for photonic fields. A higher probability may be obtained at the expense of lowering the performance fidelity [58]. Owing to this, the number of these operations that can be successively applied has been limited.

The conventional addition and subtraction of a particle can be written as

$$\hat{S}^+ = \sum_{n=0} |n+1\rangle\langle n|, \quad \hat{S}^- = \sum_{n=0} |n-1\rangle\langle n|. \quad (6.2)$$

The addition \hat{S}^+ takes the n particle state to the $|n+1\rangle$ state, whereas the subtraction operation \hat{S}^- brings the $|n\rangle$ state to the $|n-1\rangle$ state without incurring additional factors. Seeing the form of the operations in Equ. (6.2), we immediately recognize that \hat{S}^+ is a deterministic process while \hat{S}^- may not be, as it is not possible to subtract a particle from the vacuum state $|0\rangle$. When the vacuum component of the initial state is small, the subtraction can be done near-deterministically. In recent times, there have been theoretical proposals of the operations [Equ. (6.2)] for the generation of an arbitrary quantum state [59], the measurement of vacuum [60], the transformation to a non-

classical state [61] and the amplification of a quantum state [62]. In particular, such arithmetic operations form an important component of a qubit gate operation for ions in a harmonic potential [63]. The operations were also suggested as the elements of a phase operator [64].

In this project, the deterministic addition and near-deterministic subtraction protocols of a phonon is developed and demonstrated. Its application in the projective measurement of phonons is also explored.

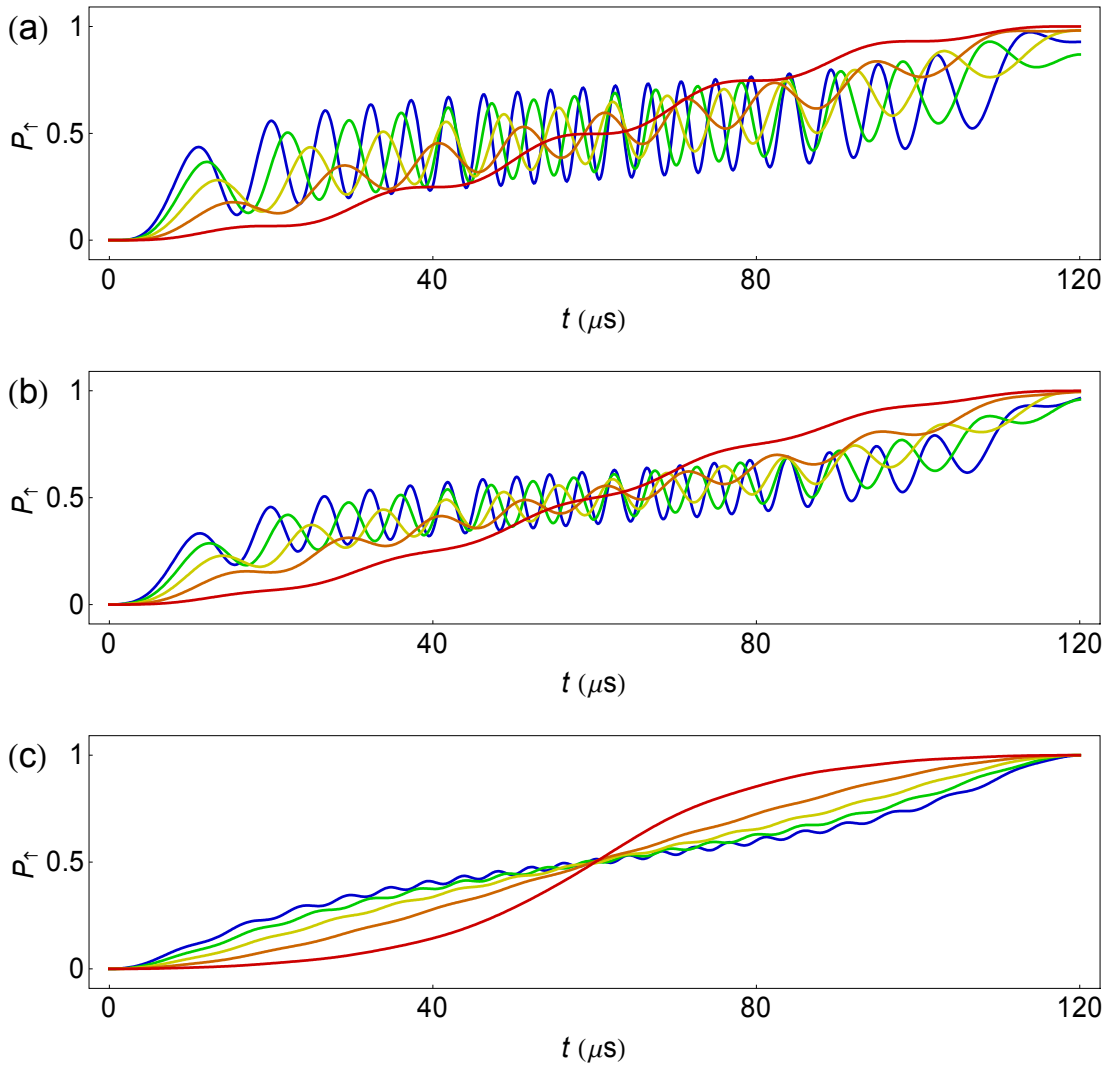


Fig. 6.1 The numerical simulations of the adiabatic driving. (a) Equ. (6.4) without any optimization, with the red, orange, yellow, green and blue curve corresponding to $k = 1, \sqrt{2}, \sqrt{3}, \sqrt{4}, \sqrt{5}$ respectively. (b) With only counter-diabatic term $b = \omega/2$. (c) With scaling factor $a = \sqrt{3}$ and counter-diabatic term $b = \omega/2$.

6.2 Uniform Driving of the Phonons

The Rabi frequency of phonon sideband transitions has a factor of \sqrt{n} , so there is no simple way to drive π -transitions uniformly for different Fock states at the same time. However, as demonstrated in Fig. 5.2, an adiabatic process is able to drive the system around by slowly changing the Hamiltonian. So a straight forward way to implement such uniform driving is to control the parameters in a similar manner. But first, for the simplicity of the notation, we can analyze the problem in a two level system with Hamiltonian

$$\hat{H}(t) = \frac{\Delta(t)}{2} \hat{\sigma}_z + \frac{k\Omega(t)}{2} \hat{\sigma}_x, \quad (6.3)$$

since the blue sideband transitions are just multiple independent transitions between $|\downarrow, n\rangle$ and $|\uparrow, n+1\rangle$, and the coefficient k characterize the \sqrt{n} factor of the Rabi frequency. So the parameters are controlled similarly as in Chapter 5,

$$\Delta(t) = \mathcal{E} \cos \omega t, \quad \Omega(t) = \mathcal{E} \sin \omega t. \quad (6.4)$$

The result of numerical simulation for $\mathcal{E} = (2\pi)50$ kHz, $\omega = \mathcal{E}/12$, and $k = 1, \sqrt{2}, \sqrt{3}, \sqrt{4}, \sqrt{5}$ is shown in Fig. 6.1(a). It is obvious that when k gets larger, the adiabaticity of the process gets drastically worse and the system is not properly driven to $|\uparrow\rangle$.

However, this can be improved. Since in the case of $k = 1$, the state of the system is basically rotating around with a constant angular velocity, so it would be better if a weak counter-diabatic term is applied to drive the rotation dynamically,

$$\hat{H}(t) = \frac{\Delta(t)}{2} \hat{\sigma}_z + \frac{k\Omega(t)}{2} \hat{\sigma}_x + \frac{kb}{2} \hat{\sigma}_y. \quad (6.5)$$

The numerical simulation for $b = \omega/2$ [Fig. 6.1(b)] shows that the adiabaticity is better. But for large k the oscillation in the middle is still pretty big, since this optimization only works when $k \approx 1$. So we can add a scaling factor a for Δ to make $k/a \approx 1$,

$$\Delta(t) = a\mathcal{E} \cos \omega t. \quad (6.6)$$

And this time the result of the numerical simulation for $a = \sqrt{3}$ and $b = \omega/2$ is way better than the previous two cases [Fig. 6.1(c)]. The populations of $|\downarrow\rangle$ at the end of the evolution for all the three cases are listed in Tab. 6.1 for reference. To put it more intuitively, the general idea of this protocol is to take the advantage of both dynamic driving and adiabatic driving. The weak counter-diabatic term drives the system

dynamically to improve the adiabaticity of the evolution, while the adiabatic driving keeps the evolution of the system on track should there be any deviations of the parameters.

Tab. 6.1 The infidelity of population transfer of the adiabatic process

k	1	$\sqrt{2}$	$\sqrt{3}$	$\sqrt{4}$	$\sqrt{5}$
(a)	2.9×10^{-5}	1.9×10^{-2}	1.9×10^{-2}	1.3×10^{-1}	7.2×10^{-2}
(b)	4.6×10^{-7}	5.1×10^{-3}	5.0×10^{-3}	4.1×10^{-2}	3.5×10^{-2}
(c)	2.6×10^{-5}	2.1×10^{-5}	1.4×10^{-4}	3.6×10^{-5}	6.4×10^{-4}

The rule of thumb to determine the optimal value of a and b can be derived straightforwardly from the analysis above. Suppose we want this operation to cover a range of k from \sqrt{m} to \sqrt{n} , then the value of a should guarantee that at both ends the ratio k/a be around 1, which leads to

$$\frac{\sqrt{m}}{a} \cdot \frac{\sqrt{n}}{a} = 1, \quad a = \sqrt[4]{mn}. \quad (6.7)$$

Similar for b , at both ends the deviation of the counter-diabatic term kb from the ideal value ω should be as small as possible, which means b should take the value that

$$(\sqrt{m}b - \omega)^2 + (\sqrt{n}b - \omega)^2 \quad (6.8)$$

is minimal, and that is

$$b = \frac{\sqrt{m} + \sqrt{n}}{m + n} \cdot \omega. \quad (6.9)$$

For the example above, $a = \sqrt[4]{5} \approx 1.495$, $b = (1 + \sqrt{5})\omega/6 \approx 0.539\omega$.

6.3 Arithmetic Operations of the Phonons

The uniform driving operation mentioned in the last section will introduce huge dynamic phase into the states. However, the addition and subtraction operators in the form of Equ. (6.2) require also phase coherence. Considering the uniform driving operation being a symmetric process, the same spin-echo technique can be used, that is, inverting the sign of Δ and Ω right in the middle of the process [Fig. 6.2(a)], but typically this will have a negative impact on the quality of the operation. The numerical simulation and experiment demonstration of this operation is shown in Fig. 6.2(b).

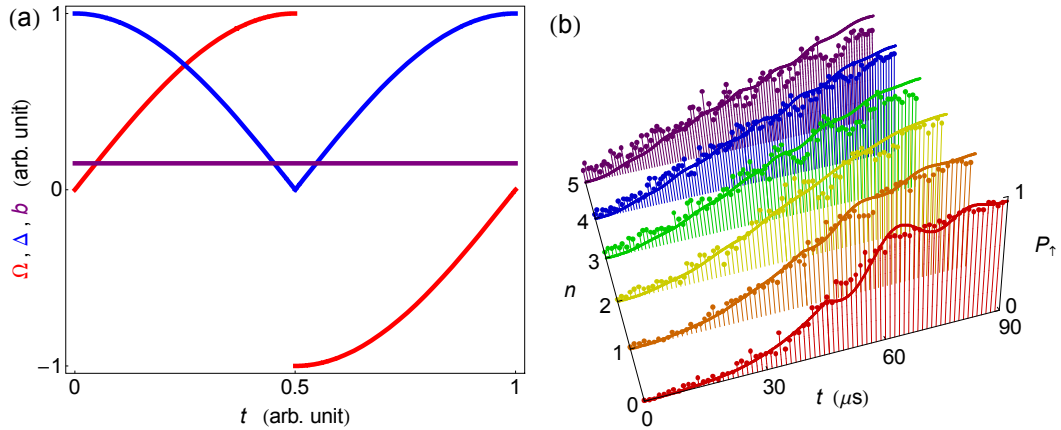


Fig. 6.2 The uniform driving with a spin-echo in the middle. (a) The control parameters. (b) The numerical simulation and experiment demonstration of the uniform driving with spin-echo for Fock states of $n = 0$ to 5, with $\mathcal{E} = (2\pi)38$ kHz, $\omega = (2\pi)5.5$ kHz, $a = 1.6$, $b = (2\pi)2.9$ kHz. The experiment is performed in a radial mode of the ion with trap frequency of 2.8 MHz.

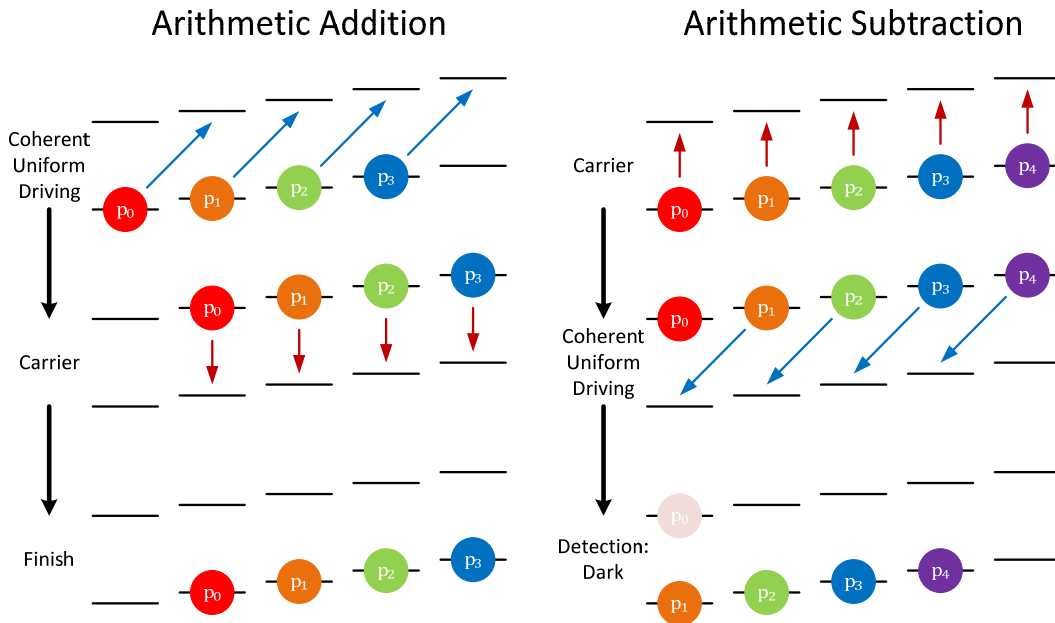


Fig. 6.3 The procedure of the arithmetic addition and subtraction operations.

With this coherent uniform driving operation, the arithmetic addition and subtraction operation of phonons can be implemented. As shown in Fig. 6.3, an addition operation consists of a uniform driving operation of blue sideband and a π -pulse of carrier transition, and the subtraction operation is just the same operations with reversed order

and with a fluorescence detection stage at the end to eliminate the population in $|\uparrow\rangle$. Of course, if the detection stage yields bright, the subtraction operation fails, so this is a probabilistic process.

The effect of the arithmetic operations on different states is tested in experiment. The result for coherent state $|\alpha = 0.8\rangle$ is in Fig. 6.4. Although the fidelity is not ideal, the preservation of the coherence can still be seen from the fringes of the Wigner function. The ability to transform a Gaussian state to a non-Gaussian state is also demonstrated, as there are negative regions in the Wigner function of the states after addition operations. The results for superposition states are in Fig. 6.5 and Fig. 6.6. The parameters used for the uniform driving operations are the same as in Fig. 6.2. The purities of the initial and added/subtracted states are in Tab. 6.2.

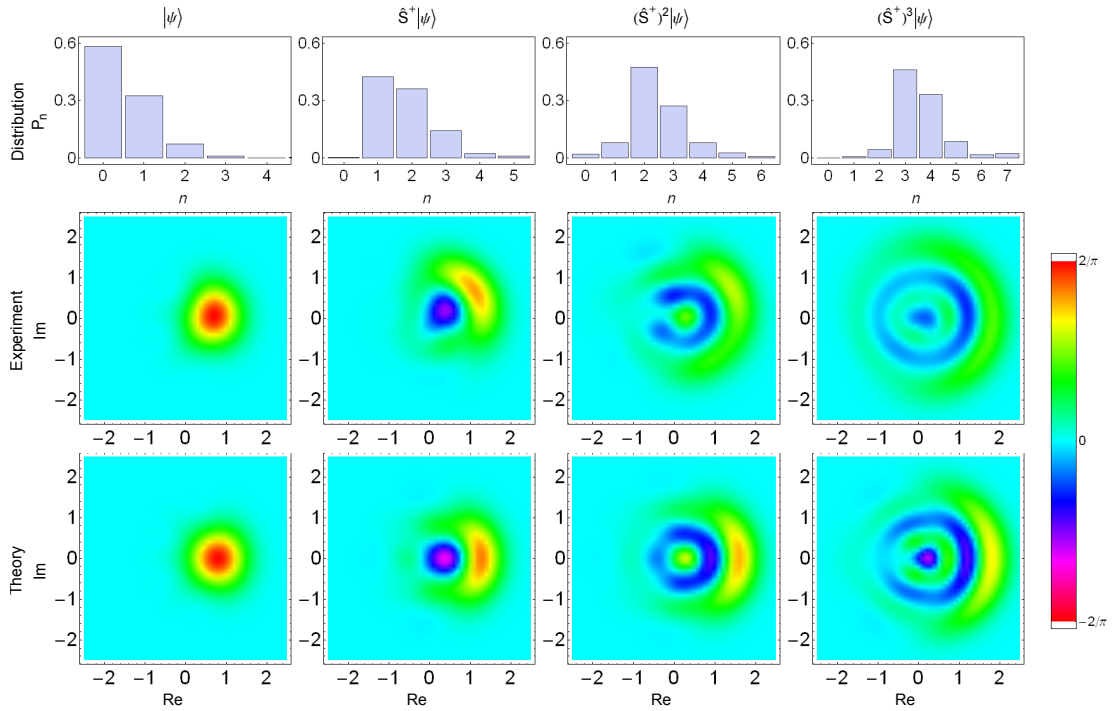
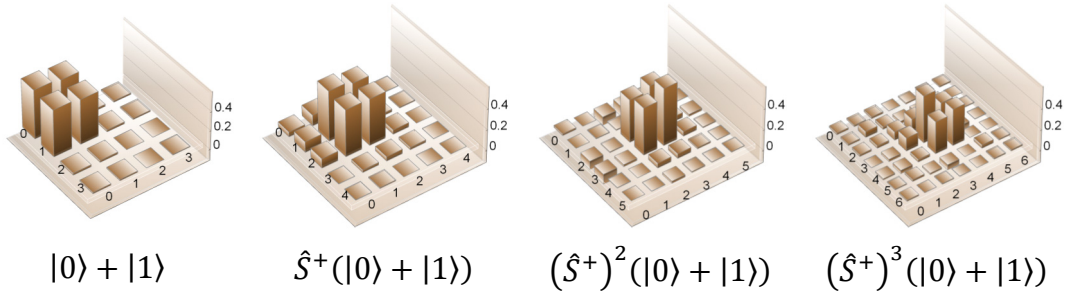
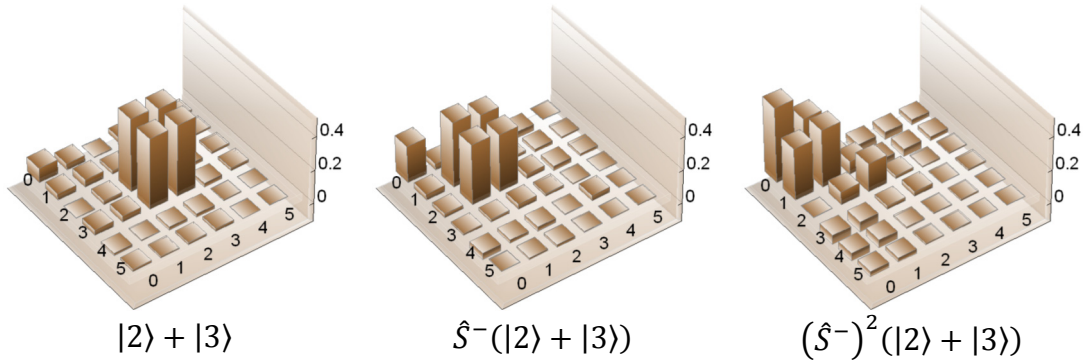


Fig. 6.4 The Wigner function and phonon distribution of coherent state $|\alpha = 0.8\rangle$ after 1, 2, 3 times of arithmetic addition operation.

Tab. 6.2 The purities of the initial and added/subtracted states.

Number of Operations	0	1	2	3
$ \alpha = 0.8\rangle$	0.99	0.93	0.93	0.80
$ 0\rangle + 1\rangle$	0.99	0.92	0.81	0.71
$ 2\rangle + 3\rangle$	0.73	0.65	0.75	—


 Fig. 6.5 The real component of the density matrix of superposition state $|0\rangle + |1\rangle$ after 1, 2, 3 times of arithmetic addition operation.

 Fig. 6.6 The real component of the density matrix of superposition state $|2\rangle + |3\rangle$ after 1, 2 times of arithmetic subtraction operation.

The method used to reconstruct the density matrices and Wigner functions of the states is a maximum-likelihood estimation method introduced in [65]. The general idea of this method is that we start with an initial guess of the density matrix of the system, and try to correct its eigenvalues and eigenstates iteratively so that the results of certain measurements performed on it are as close to the experiment results as possible. In this experiment, a state to be analyzed is displaced along each of the 8 directions with distance $|\alpha| = 0.8$, and the phonon distribution is measured after the displacement by fitting the

blue sideband fluorescence signal, as shown in Fig. 6.7. And the 8 distributions serve as the reference measurements to reconstruct the density matrix, from which the Wigner function can then be calculated. The significant advantage of this method is that the estimated density matrix is bound to be physical, otherwise the quantitative analysis such as calculating the fidelity and purity can be very tricky for a non-physical estimation.

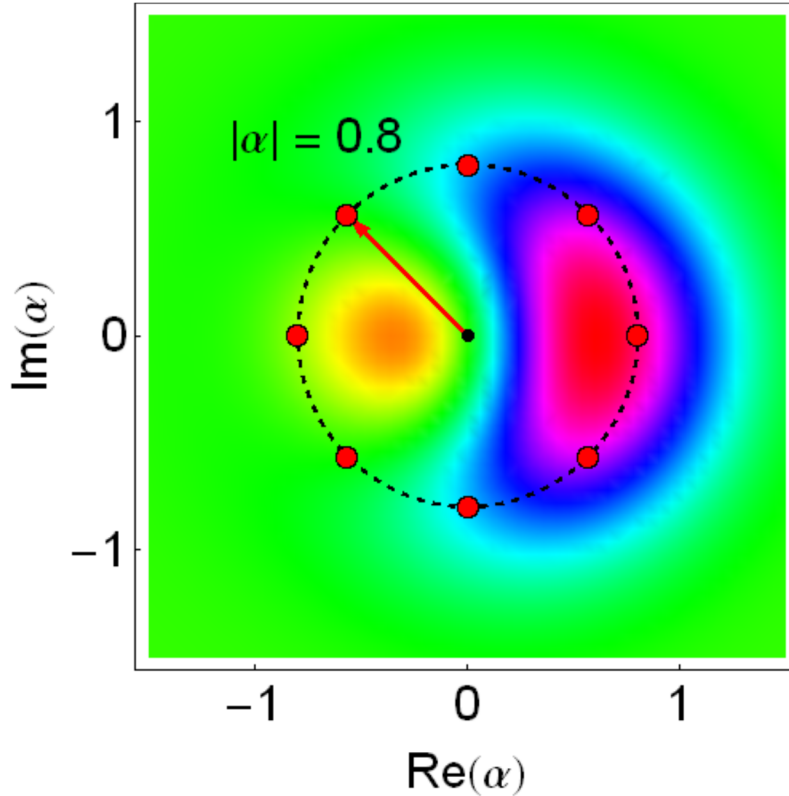


Fig. 6.7 The protocol to reconstruct the density matrix and the Wigner function. The state is displaced to each of the 8 positions equally spaced on a circle in the phase space, and then the phonon distribution is measured.

6.4 Projective Measurement of the Fock States

The common way to determine the phonon distribution of a state is to fit the fluorescence signal of a sideband transition, as mentioned in Chapter 2, and it is not projective. However, with the uniform driving operation, the projective measurement of the Fock states can be implemented. As shown in Fig. 6.8, the procedure is very similar to the arithmetic subtraction operation. Only this time if the detection stage yields bright, we know that the state is projected to $|0\rangle$. Although the state is destroyed for sure after the detection stage, due to the scattering of the photons, we can always generate the

projected state after that, so effectively this is a successful projection. And if the detection stage yields dark, which means the population of $|0\rangle$ is eliminated, we can repeat the procedure to project the state to $|1\rangle$, $|2\rangle$, $|3\rangle$, etc. Intuitively, it is just like keep asking “Is it this one?” until we get answer “Yes”.

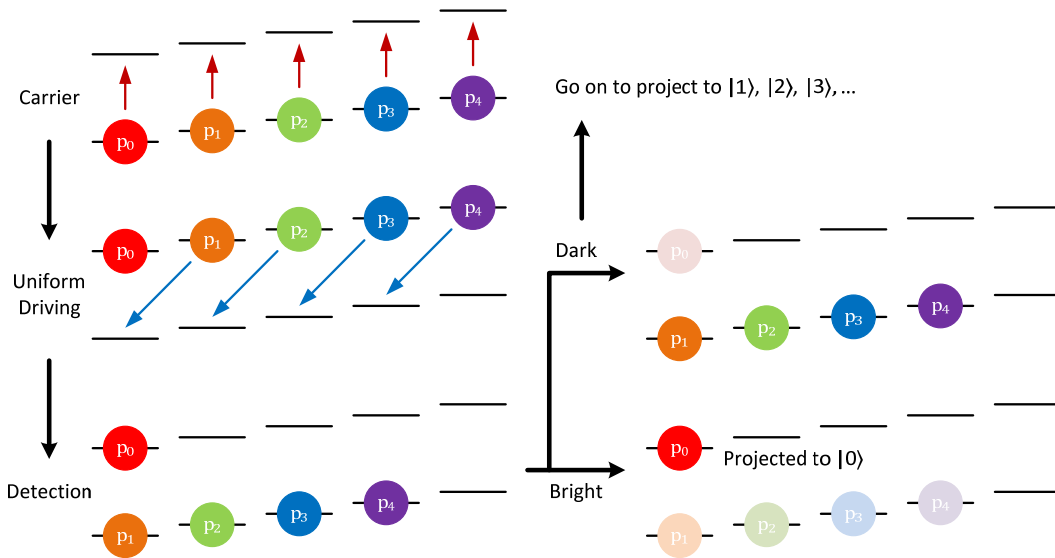


Fig. 6.8 The protocol of the projective measurement. Note that phase coherence is not required, so the spin-echo stage can be removed to improve the population transfer of the uniform driving operation.

Chapter 7 Deterministic Generation of High NOON States of Phonons

7.1 Introduction

Entanglement is an essential resource for quantum computation and quantum metrology. Classically, a parameter can be estimated more precisely by using more particles in the measurement, and the reduction of the statistical error is proportional to the square root of the particle number. In quantum metrology, the reduction factor can be improved to be linearly proportional to the particle number, which is called the Heisenberg limit, by using many-particle entangled states [66] [67] [68]. The ultimate Heisenberg limit can be achieved with the NOON state for identical indistinguishable bosons [66] [67], which can be understood by the superposition of two modes with only one of them occupied by N bosons. The NOON state has the form [69]

$$|\Psi_{\text{NOON}}\rangle = \frac{1}{\sqrt{2}} (|N, 0\rangle + e^{iN\varphi_S}|0, N\rangle), \quad (7.1)$$

where the relative phase φ_S between two modes is linearly proportional to N , showing the Heisenberg scaling for parameter estimation through the interferometric measurement. For photonic systems [70], experiments have demonstrated NOON states with particle numbers up to $N = 5$ [71] [72] [73] [74]. For distinguishable particles, up to 10 photons [75] [76] [77] and 14 ions have been prepared into the closely-related GHZ states [78] [79] [80]. NOON states have also been demonstrated in nuclear spins (NMR) [81], atomic spin waves [82], and microwave photons in superconducting systems [83].

On the other hand, the phonons have recently received increasing attention beyond the standard role as the mediator of quantum operations between internal states of ions. Phonons are proposed as the information carrier for quantum simulation [84] [85], Boson sampling [12], and quantum computation with continuous variables [86]. Recently, the NOON state with $N = 2$ has been generated through interference of phonons in each localized harmonic potential [87]. The phonons in the trapped ion system can also be manipulated through the interaction with the internal degree of freedom of an atom, similar to manipulating photons through an atom in a cavity [88]. In this project, a generic and deterministic scheme to generate phononic NOON states with arbitrary number of

bosons N for any two vibrational modes of ions is developed and demonstrated. Experimental generation of the NOON state with phonon numbers up to $N = 9$ is demonstrated and the Heisenberg scaling in the lower bound of the sensitivity in the phase estimation is clearly observed.

7.2 Generation Sequence of the NOON State

The NOON state is generated in a composite-pulse way in two phonon modes denoted as X mode and Y mode in this experiment. Taking the generation sequence of $N = 3$ as an example [Fig. 7.1], the state of the system is first initialize to $|\downarrow, n_X = 0, n_Y = 0\rangle$ by optical pumping and sideband cooling, with the first arrow being the state of the spin and the latter two number being the phonon number of the X and Y mode. By applying π -pulses of blue sideband and carrier transition successively, the state is transferred to $|\downarrow, 1, 1\rangle$. Then a $\pi/2$ -pulse is applied to change the state to $|\uparrow, 2, 1\rangle + |\downarrow, 1, 1\rangle$. Finally, two composite-pulse operations followed by a blue sideband π -pulse on Y mode and a carrier π -pulse are performed to generate the state $|\downarrow, 3, 0\rangle + |\downarrow, 0, 3\rangle$.

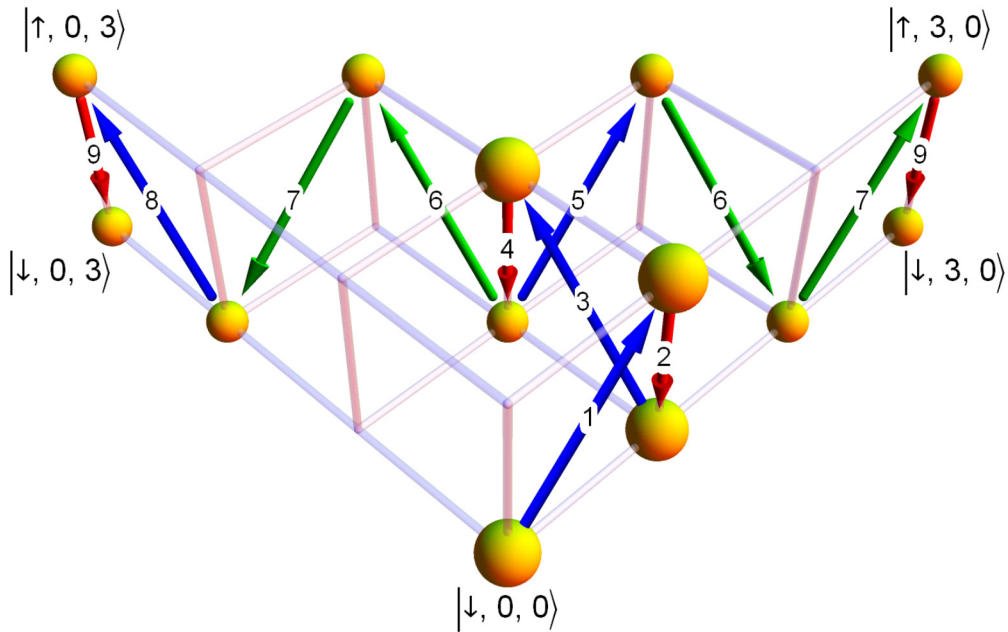


Fig. 7.1 The generation sequence of $|3003\rangle$ state. Each node of the grid denotes a Fock state. The blue, red and green arrows indicate the blue sideband, carrier and composite-pulse operations respectively. The numbers on the arrows correspond to the order of the operations.

The composite-pulse operation is inspired by Ref. [89] and is capable of driving π -transitions of blue sideband on two different Fock states, which have different Rabi frequencies. One such operation consists of three pulses. Suppose we want to drive the π -transition of $|\uparrow, 1, 0\rangle \rightarrow |\downarrow, 0, 0\rangle$ and $|\downarrow, 1, 0\rangle \rightarrow |\uparrow, 2, 0\rangle$ simultaneously, we first apply a $\pi/2$ -pulse of $|\uparrow, 1, 0\rangle \rightarrow |\downarrow, 0, 0\rangle$ transition [Fig. 7.2(a)], which is also a $\pi/\sqrt{2}$ -pulse of $|\downarrow, 1, 0\rangle \rightarrow |\uparrow, 2, 0\rangle$ transition. Then we apply a π -pulse of $|\downarrow, 1, 0\rangle \rightarrow |\uparrow, 2, 0\rangle$ transition with a $\pi/2$ phase difference than the previous pulse [Fig. 7.2(b)], and the other transition is not affected since the state is the eigenstate of this operation. Finally another $\pi/2$ -pulse of $|\uparrow, 1, 0\rangle \rightarrow |\downarrow, 0, 0\rangle$ transition is applied which concludes the composite-pulse operation [Fig. 7.2(c)].

With the composite-pulse operation introduced in detail, a generalized description of the generation sequence of arbitrary NOON states is in Tab. 7.1. The following terms are defined for notation convenience: R_C denotes a carrier π -pulse, $R_X(\theta, \varphi, n)$ denotes a blue-sideband pulse of the X mode such that the transition between $|\downarrow, n_X, n_Y\rangle$ and $|\uparrow, n_X + 1, n_Y\rangle$ has rotation angle θ and phase φ , $R_Y(\theta, \varphi, n)$ is similarly defined,

$$C_M(a, b) \equiv R_M(\pi/2, 0, a), R_M(\pi, \pi/2, b), R_M(\pi/2, 0, a) \quad (7.2)$$

denotes a composite-pulse operation on mode M, and finally $k_X = \lfloor (N - 1)/2 \rfloor$, $k_Y = \lfloor N/2 \rfloor$. It requires a total number of $5N - 2$ pulses to generate the NOON state from $|\downarrow, 0, 0\rangle$.

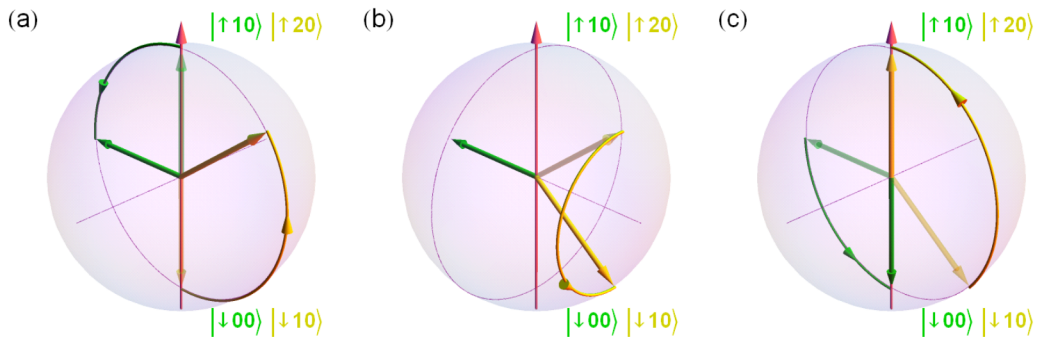


Fig. 7.2 The procedure of the composite-pulse operation. The evolutions of the two transitions are shown simultaneously. (a) a $\pi/2$ -pulse of $|\uparrow, 1, 0\rangle \rightarrow |\downarrow, 0, 0\rangle$ transition. (b) a π -pulse of $|\downarrow, 1, 0\rangle \rightarrow |\uparrow, 2, 0\rangle$ transition with a $\pi/2$ phase difference. (c) another $\pi/2$ -pulse of $|\uparrow, 1, 0\rangle \rightarrow |\downarrow, 0, 0\rangle$ transition.

Tab. 7.1 The generation sequence of arbitrary NOON states.

Step	Operation	Final State
Start	Initialization	$ \downarrow, 0, 0\rangle$
1	$R_X(\pi, 0, 0), R_C$	$ \downarrow, 1, 0\rangle$
2	$R_X(\pi, 0, 1), R_C$	$ \downarrow, 2, 0\rangle$
...
k_X	$R_X(\pi, 0, k_X - 1), R_C$	$ \downarrow, k_X, 0\rangle$
$k_X + 1$	$R_Y(\pi, 0, 0), R_C$	$ \downarrow, k_X, 1\rangle$
...
$N - 1$	$R_Y(\pi, 0, k_Y - 1), R_C$	$ \downarrow, k_X, k_Y\rangle$
N	$R_X(\pi/2, 0, k_X)$	$ \uparrow, k_X + 1, k_Y\rangle + \downarrow, k_X, k_Y\rangle$
$N + 1$	$C_Y(k_Y - 1, k_Y)$	$ \downarrow, k_X + 1, k_Y - 1\rangle + \uparrow, k_X, k_Y + 1\rangle$
$N + 2$	$C_X(k_X + 1, k_X - 1)$	$ \uparrow, k_X + 2, k_Y - 1\rangle + \downarrow, k_X - 1, k_Y + 1\rangle$
$N + 3$	$C_Y(k_Y - 2, k_Y + 1)$	$ \downarrow, k_X + 2, k_Y - 2\rangle + \uparrow, k_X - 1, k_Y + 2\rangle$
$N + 4$	$C_X(k_X + 2, k_X - 2)$	$ \uparrow, k_X + 3, k_Y - 2\rangle + \downarrow, k_X - 2, k_Y + 2\rangle$
...
$N + 2k_X - 1$	$C_Y(k_Y - k_X, N - 2)$	$ \downarrow, 2k_X, k_Y - k_X\rangle + \uparrow, 1, N - 1\rangle$
$N + 2k_X$	$C_X(2k_X, 0)$	$ \uparrow, 2k_X + 1, k_Y - k_X\rangle + \downarrow, 0, N - 1\rangle$
For odd N , $k_Y - k_X = 0$ and $2k_X = N - 1$		
$2N$	$R_Y(\pi, 0, N - 1), R_C$	$ \downarrow, N, 0\rangle + \downarrow, 0, N\rangle$
For even N , $k_Y - k_X = 1$ and $2k_X = N - 2$		
$2N - 1$	$C_Y(0, N - 1)$	$ \downarrow, N - 1, 0\rangle + \uparrow, 0, N\rangle$
$2N$	$R_X(\pi, 0, N - 1), R_C$	$ \downarrow, N, 0\rangle + \downarrow, 0, N\rangle$

7.3 Fidelity and Quantum Fisher Information

If each phonon is considered to be a distinguishable particle that can either be in X mode or in Y mode, the NOON state can be written as

$$|\Psi_{\text{NOON}}\rangle = \frac{1}{\sqrt{2}}(|\text{XXX} \dots \text{X}\rangle + |\text{YYY} \dots \text{Y}\rangle). \quad (7.3)$$

Although this not a strict notation, you can immediately see the similarity between the NOON states and the GHZ states of the spins,

$$|\Psi_{\text{GHZ}}\rangle = \frac{1}{\sqrt{2}}(|\uparrow\uparrow\uparrow \dots \uparrow\rangle + |\downarrow\downarrow\downarrow \dots \downarrow\rangle). \quad (7.4)$$

Since the density matrix of an ideal GHZ state contains only four terms, the fidelity of the GHZ state can be determined by measuring these terms [78]. The two diagonal terms are just the populations of the “all up” and “all down” components, and are easy to measure. While the two off-diagonal terms is evaluated by measuring the contrast of the parity oscillation of the spins after a global $\pi/2$ -pulse with varying phase φ . The parity of the spins is defined as the expectation value of the parity operator,

$$\hat{\Pi}_s = \prod_i \hat{\sigma}_z^{(i)}. \quad (7.5)$$

According to this similarity, we should be able to determine the fidelity of the generated NOON state in the same way, if it is possible to rotate the mode of each phonon to something like a “ $X + e^{i\varphi}Y$ ” mode and then measure the parity of the phonons.

The parity operator of a phonon mode is defined as

$$\hat{\Pi} = \exp[i\pi\hat{a}^\dagger\hat{a}]. \quad (7.6)$$

And the parity of a given state $|\Psi\rangle$ is just the difference between the total population of even and odd Fock states,

$$\langle\Psi|\hat{\Pi}|\Psi\rangle = \sum_i P_{2i} - P_{2i+1}. \quad (7.7)$$

So if we define the creation and annihilation operators for this “ $X + e^{i\varphi}Y$ ” mode as the linear combinations of those of X and Y mode,

$$\hat{a}_0^\dagger = \frac{1}{\sqrt{2}}(\hat{a}_X^\dagger + e^{i\varphi}\hat{a}_Y^\dagger), \quad \hat{a}_0 = \frac{1}{\sqrt{2}}(\hat{a}_X + e^{-i\varphi}\hat{a}_Y), \quad (7.8)$$

we should be able to derive the fidelity.

For now, all the conclusions are just based on analogy and speculations, but they can be justified theoretically in the following way.

Suppose the density matrix of the generated NOON state is

$$\begin{aligned} \rho_{\text{exp}} = & \rho_{\text{noise}} + P_{N,0}|N, 0\rangle\langle N, 0| + P_{0,N}|0, N\rangle\langle 0, N| \\ & + e^{-iN\phi}\rho_{N0,0N}|N, 0\rangle\langle 0, N| + e^{iN\phi}\rho_{0N,N0}|0, N\rangle\langle N, 0|, \end{aligned} \quad (7.9)$$

where ρ_{noise} stands for the irrelevant part of the density matrix and is independent of ϕ . Then the fidelity of the generated state to the ideal NOON state

$$|\Psi_{\text{NOON}}\rangle = \frac{1}{\sqrt{2}}(|N, 0\rangle + e^{iN\phi}|0, N\rangle) \quad (7.10)$$

is

$$\begin{aligned} F & \equiv \langle \Psi_{\text{NOON}} | \rho_{\text{exp}} | \Psi_{\text{NOON}} \rangle \\ & = \frac{1}{2} (\langle N, 0 | \rho_{\text{exp}} | N, 0 \rangle + \langle 0, N | \rho_{\text{exp}} | 0, N \rangle \\ & \quad + e^{iN\phi} \langle N, 0 | \rho_{\text{exp}} | 0, N \rangle + e^{-iN\phi} \langle 0, N | \rho_{\text{exp}} | N, 0 \rangle) \\ & = \frac{1}{2} [P_{N,0} + P_{0,N} + e^{iN(\phi-\phi)}\rho_{N0,0N} + e^{-iN(\phi-\phi)}\rho_{N0,0N}] \\ & = \frac{1}{2} [P_{N,0} + P_{0,N} + 2\rho_{N0,0N} \cos N(\phi - \phi)]. \end{aligned} \quad (7.11)$$

In experiment, the phase can be calibrated so that $\phi = \varphi = 0$. The fidelity is then

$$F = \frac{1}{2} (P_{N,0} + P_{0,N} + 2\rho_{N0,0N}). \quad (7.12)$$

The values of the two diagonal terms, $P_{N,0}$ and $P_{0,N}$, can be directly measured by projective measurement, which will be discussed in detail in the next section. While for the off-diagonal term $\rho_{N0,0N}$, in order to show its relation to the parity oscillation, we first introduce Schwinger's oscillator model of angular momentum,

$$\begin{aligned} \hat{J}_X & = \frac{1}{2} (\hat{a}_X^\dagger \hat{a}_Y + \hat{a}_X \hat{a}_Y^\dagger), \\ \hat{J}_Y & = \frac{1}{2i} (\hat{a}_X^\dagger \hat{a}_Y - \hat{a}_X \hat{a}_Y^\dagger), \\ \hat{J}_Z & = \frac{1}{2} (\hat{a}_X^\dagger \hat{a}_X - \hat{a}_Y^\dagger \hat{a}_Y). \end{aligned} \quad (7.13)$$

Then the density matrix of the system can be expressed in the angular momentum basis $|J = N/2, M_Z\rangle$ as

$$\begin{aligned} \rho_{\text{exp}} = & P_{N,0}|J, J\rangle\langle J, J| + P_{0,N}|J, -J\rangle\langle J, -J| \\ & + \rho_{N0,0N}|J, J\rangle\langle J, -J| + \rho_{N0,0N}|J, -J\rangle\langle J, J| + \rho_{\text{noise}}. \end{aligned} \quad (7.14)$$

First we consider the form of the parity operator in the X mode,

$$\hat{\Pi} = \exp[i\pi\hat{a}_X^\dagger\hat{a}_X] = \exp\left[\frac{i\pi}{2}(\hat{a}_X^\dagger\hat{a}_X - \hat{a}_Y^\dagger\hat{a}_Y + N)\right] = \exp[i\pi\hat{J}] \exp[i\pi\hat{J}_Z]. \quad (7.15)$$

And then transform it into the “ $X + e^{i\varphi}Y$ ” mode with the following operator,

$$\begin{aligned} \hat{U} &= \exp\left[-\frac{i\pi}{4}(\hat{a}_X^\dagger\hat{a}_Y e^{i\varphi} - \hat{a}_X\hat{a}_Y^\dagger e^{-i\varphi})\right] \\ &= \exp\left[-\frac{i\pi}{2}(\hat{J}_X \cos\varphi - \hat{J}_Y \sin\varphi)\right], \end{aligned} \quad (7.16)$$

$$\hat{U}^\dagger(\varphi)\hat{\Pi}\hat{U}(\varphi) = e^{i\pi N} \sum_{M=-J}^J e^{2iM(\varphi-\pi/2)} |J, M\rangle\langle J, -M|.$$

The parity measured in the “ $X + e^{i\varphi}Y$ ” mode is thus

$$\langle \hat{\Pi}(\varphi) \rangle = \text{Tr}[\rho_{\text{exp}} \hat{U}^\dagger(\varphi) \hat{\Pi} \hat{U}(\varphi)] = 2\rho_{N0,0N} e^{i\pi N} \cos N(\varphi - \pi/2). \quad (7.17)$$

Finally, we have the oscillation of the parity with phase φ and the contrast of this oscillation is

$$C_P = 2\rho_{N0,0N}. \quad (7.18)$$

Another closely related quantity is the quantum Fisher information F_Q of the NOON state, which provides the best possible precision on a parameter estimation given by $1/\sqrt{F_Q}$ [90] [91], known as the Cramér-Rao bound. For N particles without entanglement, the best possible measurement scales as $1/\sqrt{N}$ but for the NOON state, the lower bound of the precision scales as $1/N$, the Heisenberg limit.

The quantum Fisher information of the NOON state can be calculated as follows. First, we use the diagonal form of ρ_{exp} ,

$$\rho_{\text{exp}} = \lambda_1 |\Psi_1\rangle\langle\Psi_1| + \lambda_2 |\Psi_2\rangle\langle\Psi_2| + \rho_{\text{noise}}, \quad (7.19)$$

where

$$\begin{aligned} |\Psi_1\rangle &= \cos\frac{\theta}{2} |N, 0\rangle + e^{iN\phi_s} \sin\frac{\theta}{2} |0, N\rangle, \\ |\Psi_2\rangle &= \sin\frac{\theta}{2} |N, 0\rangle - e^{iN\phi_s} \cos\frac{\theta}{2} |0, N\rangle, \\ \rho_{\text{noise}} &= \sum_{n>2} \lambda_n |\Psi_n\rangle\langle\Psi_n|, \\ P_{N,0} + P_{0,N} &= \lambda_1 + \lambda_2, \\ 2\rho_{N0,0N} &= |\lambda_1 - \lambda_2| \sin\theta \equiv C_P. \end{aligned} \quad (7.20)$$

The definition of quantum Fisher information is written as

$$F_Q = \text{Tr}[\rho_{\text{exp}}(\phi_S)A^2], \quad (7.21)$$

where A is the symmetric logarithmic derivative operator defined by

$$\frac{\partial \rho_{\text{exp}}(\phi_S)}{\partial \phi_S} = \frac{1}{2}[A\rho_{\text{exp}}(\phi_S) + \rho_{\text{exp}}(\phi_S)A]. \quad (7.22)$$

With this definition, we can calculate the matrix elements of A in the basis expanded by $|\Psi_i\rangle$,

$$\begin{aligned} \left\langle \Psi_i \left| \frac{\partial \rho_{\text{exp}}(\phi_S)}{\partial \phi_S} \right| \Psi_j \right\rangle &= \frac{1}{2}(\lambda_j \langle \Psi_i | A | \Psi_j \rangle + \lambda_i \langle \Psi_i | A | \Psi_j \rangle), \\ \langle \Psi_i | A | \Psi_j \rangle &= \frac{2}{\lambda_i + \lambda_j} \left\langle \Psi_i \left| \frac{\partial \rho_{\text{exp}}(\phi_S)}{\partial \phi_S} \right| \Psi_j \right\rangle. \end{aligned} \quad (7.23)$$

Note that all λ_n and $|\Psi_n\rangle$ with $n > 2$, which form ρ_{noise} , are independent of ϕ_S , therefore the only non-zero terms are

$$\langle \Psi_1 | A | \Psi_2 \rangle = -\langle \Psi_2 | A | \Psi_1 \rangle = i \frac{\lambda_1 - \lambda_2}{\lambda_1 + \lambda_2} N \sin \theta. \quad (7.24)$$

And hence

$$F_Q = \lambda_1 \langle \Psi_1 | A^2 | \Psi_1 \rangle + \lambda_2 \langle \Psi_2 | A^2 | \Psi_2 \rangle = \frac{N^2 C_P^2}{P_{N,0} + P_{0,N}}. \quad (7.25)$$

7.4 Experiment Protocol to Measure the Fidelity

From the theoretical analysis we derive the fidelity of the generated state [Equ. (7.12)]. In experiment, the values of $P_{N,0}$ and $P_{0,N}$ are measured with an extended version of the projective measurement protocol introduced in Chapter 6. The procedure to measure $P_{0,N}$ is shown in Fig. 7.3. First the fluorescence detection is performed, if it yields dark, the qubit state is projected to $|\downarrow\rangle$ [Fig. 7.3(a)], which removes all the Fock states associated with $|\uparrow\rangle$ due to the imperfections in generating the NOON state. Then an arithmetic subtraction operation and a π -pulse of carrier transition is applied, which serves as the uniform driving of red sideband transition in the X mode. The operation transfers the Fock states with $n_X \geq 1$ from $|\downarrow\rangle$ to $|\uparrow\rangle$ [Fig. 7.3(b)]. If again no fluorescence detected, these phonon states are eliminated [Fig. 7.3(c)]. Similarly for the Y mode, by applying N times of successive arithmetic subtractions and then a detection

stage, we can “roll” all the Fock states with $n_Y < N$ to $|\uparrow\rangle$ and eliminate them if no fluorescence is detected [Fig. 7.3(d)(e)]. These operations also transfer $|\downarrow, 0, N\rangle$ to $|\downarrow, 0, 0\rangle$. Finally one more subtraction operation and the detection stage are applied [Fig. 7.3(f)(g)]. If this time it yields bright, we know that the original state is projected to $|\downarrow, 0, N\rangle$. Altogether, the whole sequence is repeated for 10,000 times and the probability of detecting fluorescence only at the last stage of detection is the population of the $|\downarrow, 0, N\rangle$ state, $P_{0,N}$. In a similar manner, $P_{N,0}$ can be measured.

For the measurement of the parity in “ $X + e^{i\varphi}Y$ ” mode, the excitation of the blue sideband is required, since the parity can be calculated from the phonon distribution, and the distribution can be obtained by fitting the sideband fluorescence signal. Such excitation is realized by exciting the blue sideband transition of both X and Y mode with balanced strength and phase difference φ ,

$$\begin{aligned}
 \hat{H} &= \hat{H}_X + \hat{H}_Y \\
 &= \frac{i\eta_X\Omega_X}{2}(\hat{\sigma}^+\hat{a}_X^\dagger - \hat{\sigma}^-\hat{a}_X) + \frac{i\eta_Y\Omega_Y}{2}(\hat{\sigma}^+\hat{a}_Y^\dagger - \hat{\sigma}^-\hat{a}_Y) \\
 &= \frac{i\Omega_0}{2\sqrt{2}}[\hat{\sigma}^+(\hat{a}_X^\dagger + e^{i\varphi}\hat{a}_Y^\dagger) - \hat{\sigma}^-(\hat{a}_X + e^{-i\varphi}\hat{a}_Y)] \\
 &= \frac{i\Omega_0}{2}(\hat{\sigma}^+\hat{a}_0^\dagger - \hat{\sigma}^-\hat{a}_0), \\
 \Omega_0 &\equiv \sqrt{2}\eta_X\Omega_X = \sqrt{2}\eta_Y\Omega_Y.
 \end{aligned} \tag{7.26}$$

The experiment is performed with a single $^{171}\text{Yb}^+$ ion, with the two radial modes as X and Y mode. The trap frequencies of the two modes are $\omega_X = (2\pi)3.2$ MHz and $\omega_Y = (2\pi)2.6$ MHz. And the Lamb-Dicke parameters are $\eta_X = 0.0538$, $\eta_Y = 0.0597$. The result of the parity oscillation measurement is in Fig. 7.4. The contrast of the parity oscillation is obtained by fitting the oscillation with

$$\langle \Pi(\varphi) \rangle = A \cos k\varphi + B \sin k\varphi + C, \quad C_P = \sqrt{A^2 + B^2}, \tag{7.27}$$

where A , B , C and k are fitting parameters. The result of the fidelity and the quantum Fisher information is shown in Fig. 7.5. The scaling of the quantum Fisher information is clearly below the classical limit and approach the quantum bound.

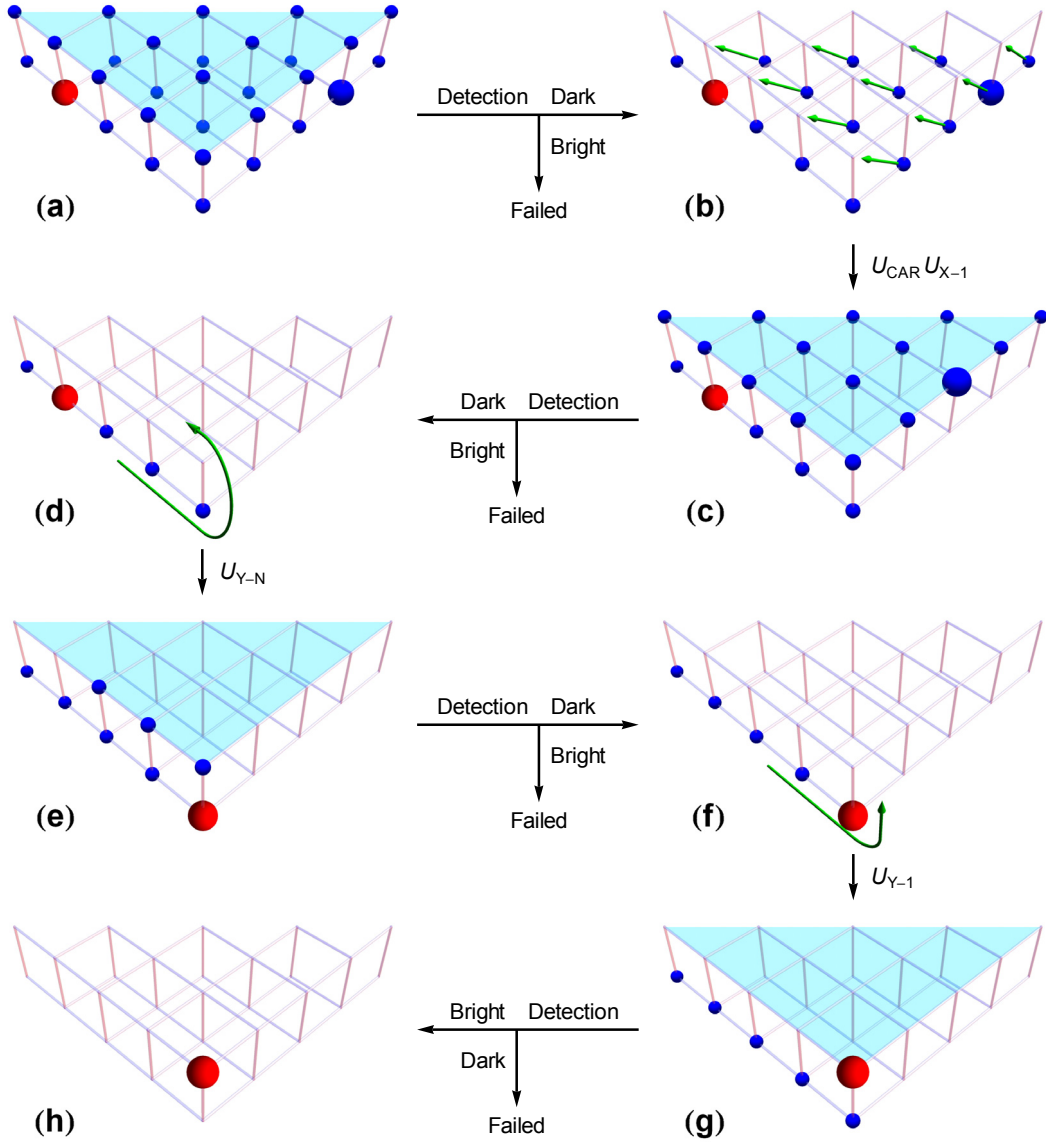


Fig. 7.3 The procedure to measure $P_{0,N}$. The red sphere indicates the target state, $|\downarrow, 0, N\rangle$. U_{CAR} denote a π -pulse of the carrier transition, and U_{X-1} , U_{Y-N} denotes arithmetic subtraction operation(s).

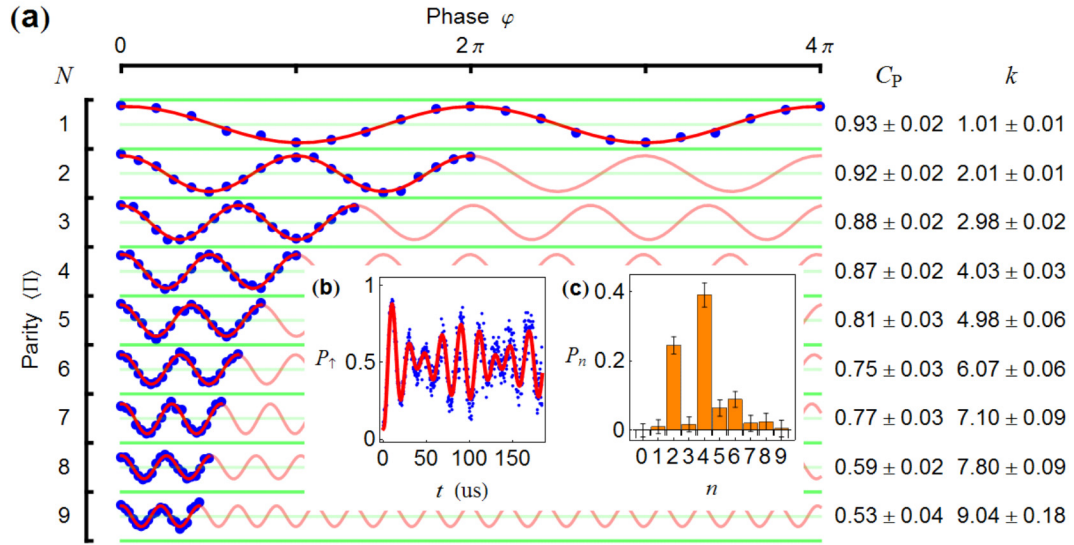


Fig. 7.4 The parity oscillations of the generated NOON states from $N = 1$ to $N = 9$. (a) The blue dots are experimental data, the red lines are fitting curves, and the green lines indicate -1, 0, 1, for each parity oscillation. (b) The blue-sideband fluorescence signal with $\varphi = 0$ for the NOON state of $N = 7$ and its fitting. (c) The corresponding phonon distribution P_n .

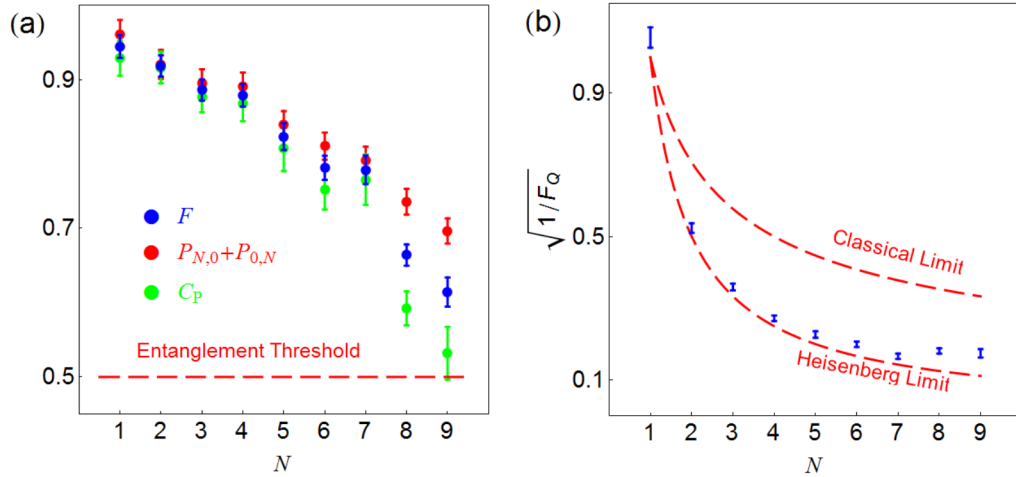


Fig. 7.5 The (a) fidelity and (b) quantum Fisher information of the generated NOON states.

7.5 Optimization and Parameter Calibration

Generating NOON states is a quite demanding experiment, since there are many details that can affect the fidelity of the generated state. The techniques used in experiment to optimize the fidelity and calibrate the parameters are discussed in this section.

For higher N , the generation sequence can take a quite long time. The decoherence and thermalization effect is a problem, so the operations should be as fast as possible. However, if the pulses to drive the phonon sideband transition are too strong, the off-resonant coupling to the carrier and other transitions will reduce the fidelity. So the pulse-shaping technique is implemented to address this conflict. Usually the pulses we use in experiment have a rectangular envelope,

$$E(t) = A \sin[(\omega - \delta)t + \varphi]. \quad (7.28)$$

In this experiment, a sine-shaped envelope is used instead,

$$E(t) = \frac{\pi A}{2} \sin\left[\frac{\pi t}{T}\right] \sin\left[\omega t + \frac{\pi^2 \delta}{8} \left(2\pi t - T \sin\left[\frac{2\pi t}{T}\right]\right) + \varphi\right]. \quad (7.29)$$

The sine-shaped pulse has the advantage that during the application of the pulse, all the off-resonant transitions are adiabatically following the Hamiltonian and remained as its eigenstates. The phase term $\pi^2 \delta (2\pi t - T \sin[2\pi t/T])/8$ is used to compensate the AC-Stark shift from various origins. The parameters of the pulse that require calibration are the amplitude factor A , the resonant frequency ω and the AC-Stark shift compensation factor δ , while the pulse duration T and phase φ is predetermined. The value of A can be determined with rectangular pulses by observing the Rabi oscillation, and the resonant frequency ω can be measured using Ramsey method with rectangular pulses. Then δ , as the last parameter, can be determined by simply sweeping the value of it with the sine-shaped pulses, just the same as measuring the driving frequency with rectangular pulses. According to the numerical simulation, the fidelity reduction of the generated state is 40% without pulse shaping, which is reduced to 4% with pulse shaping for $N = 9$.

Another problem is the phase ϕ of the generated state, the phase φ used in the parity measurement needs to be aligned with ϕ , so that all the parity measurements are consistent with each other. However, the phase ϕ is difficult to determine theoretically, since any small deviations in the resonant frequency of the phonon mode and various AC-

Stark shift can affect this phase, and it also slowly drifts during the course of the data taking. So a scheme to quickly determine and compensate this phase is developed. By exciting the blue sideband transition of the “ $X + e^{i\varphi}Y$ ” mode for a fixed duration with varying φ , the state of the spin has similar behavior as the parity oscillation. In [FIG.(a)] is an example for $N = 5$, the color indicates the population of $|\uparrow\rangle$ with different phase φ and rotation angle $\theta = \Omega_0 t$ of the blue sideband transition. If we take $\theta = 3.55\pi$, for a generated state with phase $\phi = 0$, we should have an oscillation of P_\uparrow as in [FIG.(b)] with no phase shift. So the phase shift of this sine curve can be used to calibrate the phase ϕ of the generated state by changing the phase of the $\pi/2$ -pulse in the generation sequence accordingly. For each N , there is an optimal value of θ such that the contrast of this oscillation is maximal.

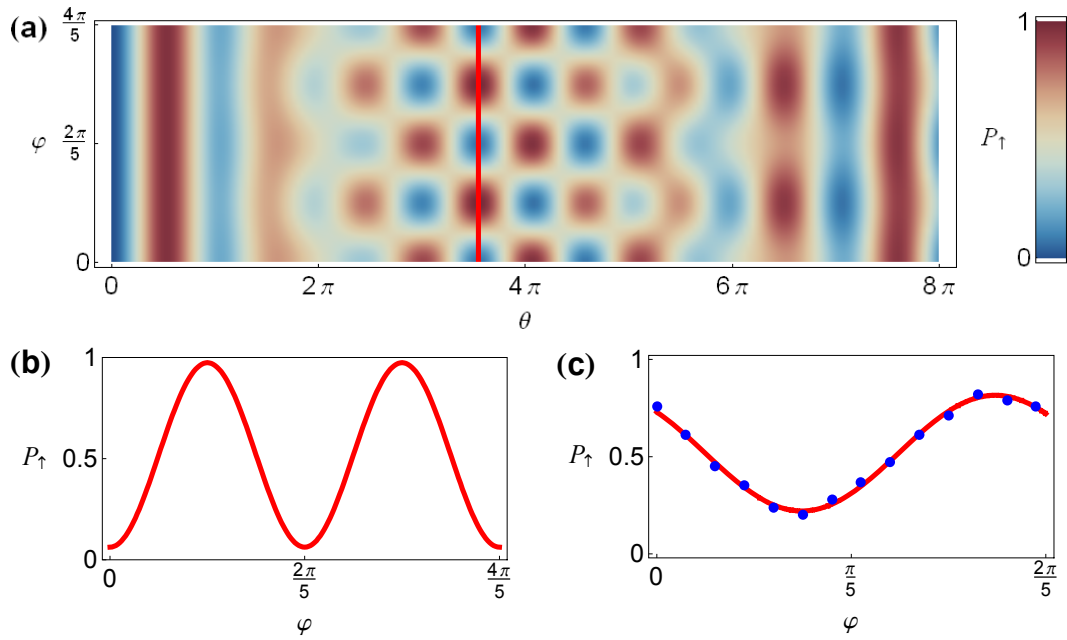


Fig. 7.6 The phase calibration scheme.

(a) the theoretical calculation of the dependency of P_\uparrow on θ and φ . The red line indicates the optimal duration, $\theta = 3.55\pi$, for $N = 5$. (b) Theoretical calculation of P_\uparrow when φ is scanned and θ is set to the optimum. (c) Experimental data of a typical phase scan for $N = 5$, the fitting (red line) indicates that $\phi = 0.15\pi$.

Chapter 8 Entanglement of $^{171}\text{Yb}^+$ Ion and $^{138}\text{Ba}^+$ Ion

8.1 Introduction

Increasing the number of ions in a single trap is one of the ways to scale up the trapped-ion system. Recently most of the multi-ion research is done with multiple ions of same species. However, trapping different species of ions in the same trap can have wider applications and more advantages. It can be used for sympathetic cooling [92], creation of entanglement through dissipation [93], or performing quantum non-demolition measurements [94]. One experiment of our system [31] is to use the $^{171}\text{Yb}^+$ ion to be the qubit while the $^{138}\text{Ba}^+$ ion to sympathetically cool down the $^{171}\text{Yb}^+$ ion for minutes-level operations. For other applications that involves quantum information transfer between the ions, the entanglement operation for different species of ions is essential. Experimental implementations of this kind of multi-species trapped-ion systems have been done with a $^{40}\text{Ca}^+$ ion and a $^{43}\text{Ca}^+$ ion [95], a $^9\text{Be}^+$ ion and a $^{25}\text{Mg}^+$ ion [96], and also quite recently a $^{171}\text{Yb}^+$ ion and $^{138}\text{Ba}^+$ ion [97].

The M-S interaction introduced in Chapter 2 works for different species as well, since only the coupling to the phonon sidebands is required and nothing else related to the nature of the ions. But implementing the M-S interaction with different species is more complicated than with same species and globally addressing laser beams, since the coupling strengths and driving frequencies of both sidebands of both ions require independent calibration, effectively doubling the number of control parameters.

In experiment, the axial breathing mode of the $^{171}\text{Yb}^+$ ion and the $^{138}\text{Ba}^+$ ion is used to mediate the M-S interaction. This mode has several advantages to other modes. First, the coherence time of axial modes is longer than the radial modes because usually the mechanical instability of the helical resonator will introduce fluctuations to the power of the RF field. Second, because the ions move in the different direction in the breathing mode, the background electric field noise is less likely to drive the motion. Hence the heating rate of the breathing mode is much lower than the center of mass mode. Third, the frequency of the breathing mode is higher, so the off-resonant coupling to the carrier transition is lower. And finally, the Lamb-Dicke parameters for both ions are more balanced for the breathing mode than the center of mass mode. According to Fig. 3.1 and

Equ. 2.42, the ratios of the Lamb-Dicke parameters can be calculated,

$$\frac{\eta_{\text{Yb,H}}}{\eta_{\text{Ba,H}}} = 1.09, \quad \frac{\eta_{\text{Yb,L}}}{\eta_{\text{Ba,L}}} = 1.67. \quad (8.1)$$

And the mode with higher frequency, the breathing mode, has more balanced Lamb-Dicke parameters.

The excitation of both sidebands of the $^{171}\text{Yb}^+$ ion and the $^{138}\text{Ba}^+$ ion is realized by controlling the signals driving the AOMs of the Raman beams. For the two 355 nm laser beams and the two 532 nm laser beams, one of each is driven by a DDS that provides a constant single frequency signal as the base frequency. While the control of the parameters of all the quantum operations is done by changing the signals from two AWGs that drive the other two Raman beams. So basically, implementing the M-S interaction is to generate the following waveform with the two AWGs,

$$\begin{aligned} E_Y(t) &= A_{\text{YR}} \sin \omega_{\text{YR}}t + A_{\text{YB}} \sin \omega_{\text{YB}}t, \\ E_B(t) &= A_{\text{BR}} \sin \omega_{\text{BR}}t + A_{\text{BB}} \sin \omega_{\text{BB}}t, \end{aligned} \quad (8.2)$$

with correct values of the parameters A and ω . The subscripts of the terms in Equ. 8.2 indicate the purpose of the terms, with the first letter ‘‘Y’’ denoting the $^{171}\text{Yb}^+$ ion, ‘‘B’’ the $^{138}\text{Ba}^+$ ion, the second letter ‘‘B’’ the blue sideband and ‘‘R’’ the red sideband.

Ideally, the four frequencies can be determined by Ramsey measurements and the four amplitudes by scanning the Rabi oscillations of the sideband transitions. However, the real situation is way trickier. An ideal AOM has linear amplitude response and is independent of the driving frequency, but a real AOM is not. Half the driving signal amplitude for a real AOM is likely to yield a more than half driving strength of the ion, and two different frequency components both with half the amplitude is yet another different thing. As for the four frequency parameters, the cross-talk AC-Stark shift should be taken into account, so the results of Ramsey measurements are not exactly the correct values. Hence the calibration of these parameters requires carefully designed procedures.

8.2 Parameter Calibration

8.2.1 Coarse Calibration

The calibration protocol starts by coarsely measuring the values of the resonant frequencies ω and Rabi frequencies Ω of the carrier, blue sideband and red sideband transitions of both ions. The 12 parameters calibrated in this step are denoted as

$$\begin{aligned} \text{Yb: } & \{\Omega_{\text{YC1}}, \Omega_{\text{YR1}}, \Omega_{\text{YB1}}, \omega_{\text{YC1}}, \omega_{\text{YR1}}, \omega_{\text{YB1}}\}, \\ \text{Ba: } & \{\Omega_{\text{BC1}}, \Omega_{\text{BR1}}, \Omega_{\text{BB1}}, \omega_{\text{BC1}}, \omega_{\text{BR1}}, \omega_{\text{BB1}}\}, \end{aligned} \quad (8.3)$$

with the second letter ‘‘C’’ in the subscripts indicating the carrier transition and the third number ‘‘1’’ indicating the first step. All the calibrations in this step are performed with maximum output amplitude of the AWGs, $A = 1$.

The six resonant frequencies are measured by scanning the frequencies and measure the population of the $|\uparrow\rangle$ state. Then the measured spectrum is fitted with Gaussian functions to determine the frequency of the peak. Note that the resonant frequencies of the sideband transitions measured in this way contain the AC-Stark shift from the coupling to the carrier transition. Then the Rabi frequencies can be determined simply by fitting the Rabi oscillations. Only that the Rabi oscillations of the sideband transitions should be fitted with the thermal state one,

$$P_{\uparrow}(t) = A + \frac{Bs}{2} \sum_i \frac{C^i}{(1+C)^{i+1}} \cos \left[\frac{\mathcal{L}_i^1(\eta^2)}{\sqrt{1+i}} \cdot \frac{\pi t}{D} \right], \quad (8.4)$$

instead of the sine function. In Equ. 8.4, A , B are relaxation parameters, C is the fitting parameters for the average phonon number of the thermal state, $D = 1/(2\Omega)$ is the fitting parameters for the π -time of the transition, s is the polarity of the signal, being 1 for blue sideband signal and -1 for red sideband signal, and η is the Lamb-Dicke parameter of the phonon mode.

8.2.2 Fine Calibration

In this step, the Rabi frequencies and resonant frequencies of the sideband transitions are more precisely calibrated. Because of the nonlinear response of the AOMs, the Rabi frequencies should be calibrated in a way that is as close to the experiment situation as possible. So the Rabi frequencies of the sideband transitions are calibrated again with half the amplitude along with a far detuned frequency component such that the overall power driving the AOMs is same as the experiment situation. Take the blue sideband of the

$^{171}\text{Yb}^+$ ion as an example, the waveform used to calibrate $\Omega_{\text{YB}2}$ is

$$E_Y(t) = \frac{1}{2} \sin \omega_{\text{YB}2} t + \frac{1}{2} \sin \frac{t}{2} (5\omega_{\text{Y}C1} - 3\omega_{\text{YB}1}), \quad (8.5)$$

in which $\omega_{\text{YB}2}$ is the resonant frequency for this situation that should be measured in advance with this waveform and the frequency $(5\omega_{\text{Y}C1} - 3\omega_{\text{YB}1})/2$ is roughly in the middle between the red sideband of the breathing mode and the second order red sideband of the center of mass mode, and is not able to drive any transition.

In the experiment situation, the driving strengths of the blue and red sideband transitions are the same, so the resonant frequencies should be free of AS-Stark shift from the carrier transition. Hence the Ramsey measurement is used to determine these frequencies. The AC-Stark shift introduced by applying the Raman beams for the other ion will be addressed in the next step of calibration. Usually the Ramsey measurement is performed by scanning the duration of the gap between the two $\pi/2$ pulses and observing the Ramsey fringes. But this way is not convenient for automated calibration. Instead, the Ramsey measurement can be performed by scanning the frequency with fixed duration of the gap. The waveform used to calibrate $\omega_{\text{YB}3}$ is

$$E_Y(t) = \begin{cases} \sin \omega_{\text{YB}1} t & 0 \leq t < t_{\text{HP}} \\ 0 & t_{\text{HP}} \leq t < t_{\text{HP}} + g \\ -\sin[\omega_{\text{YB}1}(t - g) + \omega_{\text{YB}3}g] & t_{\text{HP}} + g \leq t \leq 2t_{\text{HP}} + g \end{cases}, \quad (8.6)$$

in which $t_{\text{HP}} = \pi/(2\Omega_{\text{YB}1})$ and g is the duration of the gap. If the scan range of $\omega_{\text{YB}3}$ is $[\omega_c - \pi/g, \omega_c + \pi/g]$, the measured curve is just one cycle of a sine curve with the lowest point indicating the resonant frequency. The parameter g can be tuned to adjust the precision of this measurement. A smaller value of g can be used first to roughly determine the resonant frequency, and then a larger value of g is used to increase the precision of the measurement. It would be helpful if the first scan is centered at the theoretical prediction of the resonant frequency,

$$\omega_c = \omega_{\text{YB}1} + \frac{\Omega_{\text{YB}1}^2}{2(\omega_{\text{YB}1} - \omega_{\text{Y}C1})}. \quad (8.7)$$

Moreover, this measurement is also insensitive to the distribution of the phonons in the sense that all the Fock states are ‘‘brought back’’ by the second pulse if the phase is precisely matched.

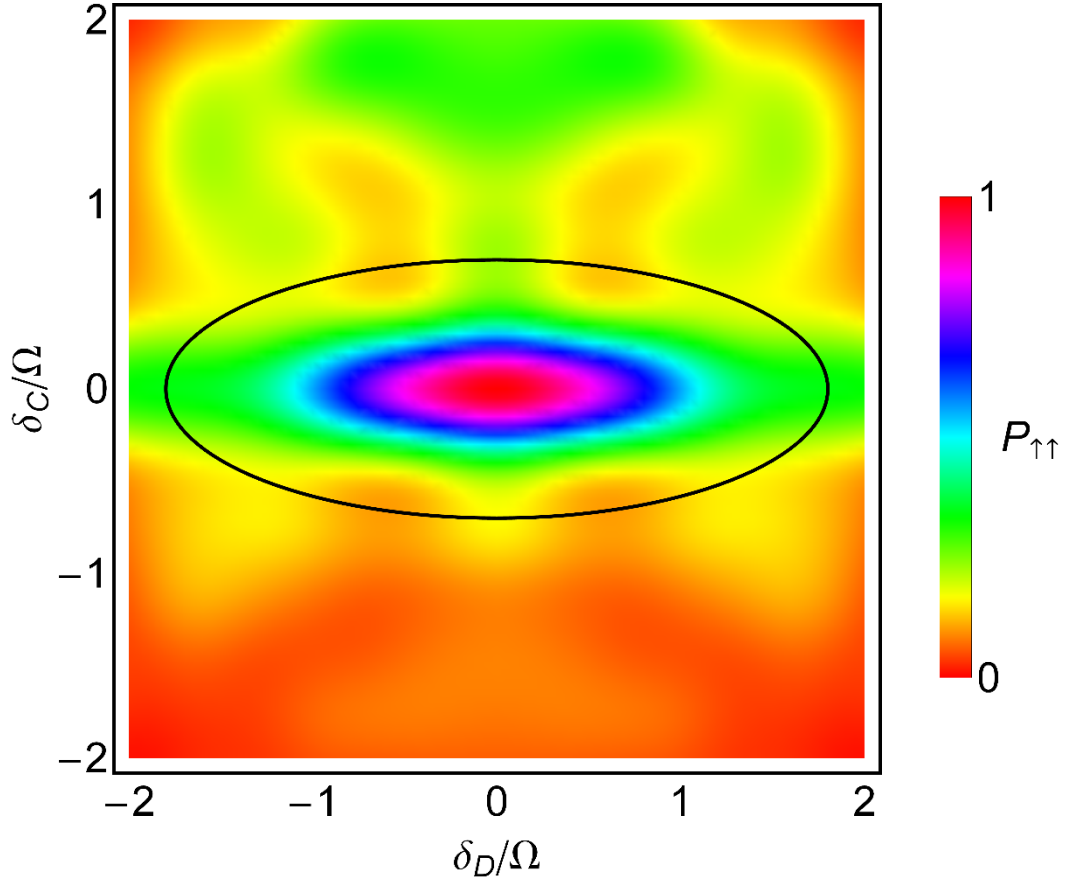


Fig. 8.1 The fidelity diagram of the Mølmer-Sørensen interaction with respect to the detuning of the driving frequencies.

8.2.3 Final Calibration

The Rabi frequencies measured in the last step can be used as the final reference to balance the amplitude of the driving signals,

$$A_{ij} = \frac{\Omega}{2\Omega_{ij2}}, \quad i = \text{Y, B}, \quad j = \text{B, R}, \quad (8.8)$$

$$\Omega = \min(\Omega_{\text{YR}2}, \Omega_{\text{YB}2}, \Omega_{\text{BR}2}, \Omega_{\text{BB}2}).$$

But there is one last problem for the resonant frequencies. When all the four Raman laser beams are applied together, the 355 nm beams may introduce AC-Stark shift to the carrier transition of the $^{138}\text{Ba}^+$ ion, and vice versa for the 532 nm beams and the $^{171}\text{Yb}^+$ ion. A straightforward solution is to apply half a cycle of the M-S interaction and maximize the population of $|\uparrow\uparrow\rangle$ by scanning the common detuning δ of both sidebands for one of the ions each time,

$$\omega_{\text{Y}j} = \omega_{\text{Y}j3} + \delta_{\text{Y}}, \quad \omega_{\text{B}j} = \omega_{\text{B}j3} + \delta_{\text{B}}, \quad j = \text{B, R}. \quad (8.9)$$

However, a better way is to scan the common detuning δ_C and differential detuning δ_D of both ions,

$$\omega_{Yj} = \omega_{Yj3} + \delta_C - \delta_D, \quad \omega_{Bj} = \omega_{Bj3} + \delta_C + \delta_D, \quad j = \text{B, R.} \quad (8.10)$$

This can be justified with numerical simulations. Fig. 8.1 shows the population of $|\uparrow\uparrow\rangle$ with varying δ_C and δ_D . The Ω is as defined in Equ. 8.8. If the initial values of δ_C and δ_D are anywhere within the black ellipse, one scan of each is sufficient to get to the peak. However, if the variables are δ_Y and δ_B , with which the figure is effectively rotated by 45° , it requires successive scans of each parameter to converge to the peak.

8.3 Fidelity of the Mølmer-Sørensen Interaction

When a quarter cycle of the M-S interaction is applied, the entangled state $|\uparrow\uparrow\rangle + |\downarrow\downarrow\rangle$ is generated from $|\downarrow\downarrow\rangle$. The fidelity of the generated state can be evaluated in the same way as introduced in Chapter 7 [78],

$$F = \frac{1}{2}(P_{\uparrow\uparrow} + P_{\downarrow\downarrow} + C_P), \quad (8.11)$$

where C_P is the contrast of the parity oscillation. The parity of the spins is measured after applying a global $\pi/2$ pulse with varying phase φ on both ions and is defined as

$$\Pi(\varphi) = P_{\uparrow\uparrow} + P_{\downarrow\downarrow} - P_{\uparrow\downarrow} - P_{\downarrow\uparrow}. \quad (8.12)$$

A preliminary experiment result is shown in Fig. 8.2 with

$$P_{\uparrow\uparrow} + P_{\downarrow\downarrow} = 0.73 \pm 0.03, \quad C_P = 0.56 \pm 0.05, \quad F = 0.65 \pm 0.06. \quad (8.13)$$

The unfeasible fidelity is mainly due to the fluctuations of the AC-Stark shift of the $^{138}\text{Ba}^+$ ion and the scattering of the Raman laser beams that slowly changes the environment of the trap.

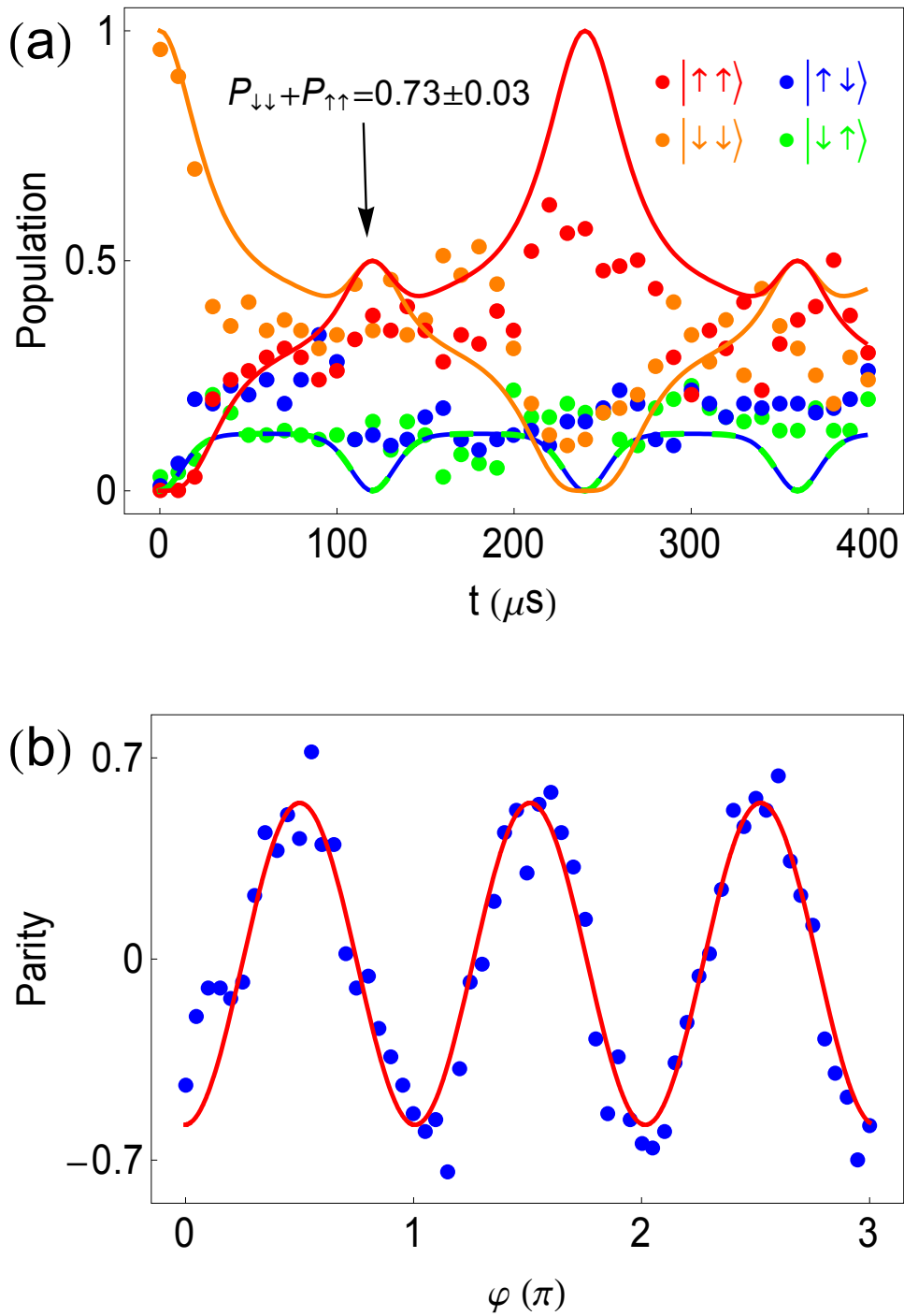


Fig. 8.2 The experiment result of the Mølmer-Sørensen interaction. (a) The time evolution of the system. (b) The parity oscillation.

Chapter 9 Conclusion and Outlook

During my Ph.D. career, my effort on hardware mainly lies in developing the TTL pulse sequencer and establishing the laser system for the $^{138}\text{Ba}^+$ ion. The pulse sequencer is implemented with a pipeline design and is capable of generating TTL pulse sequences with both high timing resolution and long duration. It serves as the central scheduler of the experiment flow. The laser system consists of diode lasers and fiber lasers to cool down the ion, to initialize and detect its quantum state, and pulsed lasers to manipulate both internal and motional quantum states of the ion.

While my study in theory is focused in developing and demonstrating control protocols for phonons. A uniform driving operation of phonons is implemented with rapid adiabatic passage scheme. The ability to perform arithmetic operations on phonon states is demonstrated in experiment. A protocol to deterministically generate phononic NOON states to arbitrary high number of phonons is also developed with composite pulse scheme. This protocol is demonstrated in experiment up to $N = 9$, and the fidelities of the generated states are evaluated. Moreover, the entanglement operation of one $^{171}\text{Yb}^+$ ion and one $^{138}\text{Ba}^+$ ion through Mølmer-Sørensen interaction is demonstrated in experiment.

As for the plan of near future, the upgrade of the pulse sequencer is now under development by my colleagues. Currently the sequencer is only capable of generating the sequence sequentially. But for experiments involving conditional operations, the branching structure is required in the sequences. One way to implement complicated logic structure yet maintaining the high timing resolution is to build the sequencer in new FPGA chips with embedded microprocessors. The FPGA circuit still do the timing, while the microprocessors control the behavior of the sequencer.

The coherence time and the fidelity of the Mølmer-Sørensen interaction still requires improvement. One experiment that can be done immediately when the fidelity is feasible, is the loophole-free verification of quantum contextuality.

References

- [1] R. Landauer, "Information is a Physical Entity," *Physica A*, vol. 263, pp. 63-67, 1999.
- [2] P. W. Shor, "Polynomial-Time Algorithms for Prime Factorization and Discrete Logarithms on a Quantum Computer," *SIAM J.Sci.Statist.Comput.*, vol. 26, pp. 1484-1509, 1997.
- [3] L. K. Grover, "A Fast Quantum Mechanical Algorithm for Database Search," *Proceedings, 28th Annual ACM Symposium on the Theory of Computing*, pp. 212-219, 1996.
- [4] I. Buluta and F. Nori, "Quantum Simulators," *Science*, vol. 326, pp. 108-111, 2009.
- [5] S. Lloyd, "Universal Quantum Simulators," *Science*, vol. 273, pp. 1073-1078, 1996.
- [6] J. L. O'Brien, "Optical Quantum Computing," *Science*, vol. 318, pp. 1567-1570, 2007.
- [7] O. Morsch and M. Oberthaler, "Dynamics of Bose-Einstein Condensates in Optical Lattices," *Rev. Mod. Phys.*, vol. 78, pp. 179-215, 2006.
- [8] Y. Nakamura, Y. A. Pashkin and J. S. Tsai, "Coherent Control of Macroscopic Quantum States in a Single-Cooper-pair Box," *Nature*, vol. 398, pp. 786-788, 1999.
- [9] D. J. Wineland, C. Monroe, W. M. Itano, D. Leibfried, B. E. King and D. M. Meekhof, "Experimental Issues in Coherent Quantum-State Manipulation of Trapped Atomic Ions," *J. Res. Natl. Inst. Stand. Technol.*, vol. 103, pp. 259-328, 1998.
- [10] N. A. Gershenfeld and I. L. Chuang, "Bulk Spin Resonance Quantum Computation," *Science*, vol. 275, pp. 350-356, 1997.
- [11] B. E. Kane, "A Silicon-based Nuclear Spin Quantum Computer," *Nature*, vol. 393, pp. 133-137, 1998.
- [12] C. Shen, Z. Zhang and L. M. Duan, "Scalable Implementation of Boson Sampling with Trapped Ions," *Phys. Rev. Lett.*, vol. 112, p. 050504, 2014.
- [13] J. I. Cirac and P. Zoller, "Quantum Computations with Cold Trapped Ions," *Phys. Rev. Lett.*, vol. 74, pp. 4091-4094, 1995.
- [14] D. L. Moehring, P. Maunz, S. Olmschenk, K. C. Younge, D. N. Matsukevich, L. M. Duan and C. Monroe, "Entanglement of Single-atom Quantum Bits at a Distance," *Nature*, vol. 449, pp. 68-71, 2007.
- [15] D. Leibfried, R. Blatt, C. Monroe and D. Wineland, "Quantum Dynamics of Single Trapped Ions," *Rev. Mod. Phys.*, vol. 75, p. 281, 2003.

-
- [16] D. J. Berkeland, J. D. Miller, J. C. Bergquist, W. M. Itano and D. J. Wineland, "Minimization of Ion Micromotion in a Paul Trap," *Journal of Applied Physics*, vol. 83, pp. 5025-5033, 1998.
- [17] T. R. Carver, "Optical Pumping," *Science*, vol. 141, pp. 599-608, 1963.
- [18] N. Röck, "Quantum Manipulation on the Barium Quadrupolar Transition," Master Thesis, University of Innsbruck, 2011.
- [19] X. Zhang, "Quantum Computation and Simulation with Trapped Ions," PhD. Thesis, Tsinghua University, 2016.
- [20] D. F. V. James, "Quantum Dynamics of Cold Trapped Ions with Application to Quantum Computation," *Appl. Phys. B*, vol. 66, p. 181, 1998.
- [21] R. Lechner, C. Maier, C. Hempel, P. Jurcevic, B. P. Lanyon, T. Monz, M. Brownnutt, R. Blatt and C. F. Roos, "EIT Ground-State Cooling of Long Ion Strings," *Phys. Rev. A*, vol. 93, p. 053401, 2016.
- [22] K. Molmer and A. Sorensen, "Multi-Particle Entanglement of Hot Trapped Ions," *Phys. Rev. Lett.*, vol. 82, pp. 1835-1838, 1999.
- [23] A. Sorensen and K. Molmer, "Quantum Computation with Ions in Thermal Motion," *Phys.Rev.Lett.*, vol. 82, pp. 1971-1974, 1999.
- [24] A. Sorensen and K. Molmer, "Entanglement and Quantum Computation with Ions in Thermal Motion," *Phys. Rev. A*, vol. 62, p. 022311, 2000.
- [25] L. M. Duan, "Scaling Ion Trap Quantum Computation through Fast Quantum Gates," *Phys. Rev. Lett.*, vol. 93, p. 100502, 2004.
- [26] J. J. García-Ripoll, P. Zoller and J. I. Cirac, "Speed Optimized Two-Qubit Gates with Laser Coherent Control Techniques for Ion Trap Quantum Computing," *Phys. Rev. Lett.*, vol. 91, p. 157901, 2003.
- [27] M. Palmero, S. Martínez-Garaot, D. Leibfried, D. J. Wineland and J. G. Muga, "Fast Phase Gates with Trapped Ions," *Phys. Rev. A*, vol. 95, p. 022328, 2017.
- [28] A. M. Steane, G. Imreh, J. P. Home and D. Leibfried, "Pulsed Force Sequences for Fast Phase-Insensitive Quantum Gates in Trapped Ions," *New J. Phys.*, vol. 16, p. 053049, 2014.
- [29] A. Chew, "Doppler-Free Spectroscopy of Iodine at 739nm," Bachelor Thesis, University of Maryland, 2008.
- [30] H. Oberst, "Resonance Fluorescence of Single Barium Ions," Master Thesis, University of Innsbruck, 1999.

- [31] Y. Wang, M. Um, J. H. Zhang, S. M. An, M. Lyu, J. N. Zhang, L. M. Duan, D. Yum and K. Kim, "Single-Qubit Quantum Memory Exceeding Ten-Minute Coherence Time," *Nature Photon.*, vol. 11, pp. 646-650, 2017.
- [32] S. Kling, T. Salger, C. Grossert and M. Weitz, "Atomic Bloch-Zener Oscillations and Stückelberg Interferometry in Optical Lattices," *Phys. Rev. Lett.*, vol. 105, p. 215301, 2010.
- [33] M. Mark, T. Kraemer, P. Waldburger, J. Herbig, C. Chin, H.-C. Nägerl and R. Grimm, "'Stückelberg Interferometry" with Ultracold Molecules," *Phys. Rev. Lett.*, vol. 99, p. 113201, 2007.
- [34] G. Cao, H. O. Li, T. Tu, L. Wang, C. Zhou, M. Xiao, G. C. Guo, H. W. Jiang and G. P. Guo, "Ultrafast Universal Quantum Control of a Quantum-Dot Charge Qubit Using Landau-Zener-Stückelberg Interference," *Nat. Commun.*, vol. 4, p. 1401, 2013.
- [35] J. R. Petta, H. Lu and A. C. Gossard, "A Coherent Beam Splitter for Electronic Spin States," *Science*, vol. 327, p. 669, 2010.
- [36] W. D. Oliver, Y. Yu, J. C. Lee, K. K. Berggren, L. S. Levitov and T. P. Orlando, "Mach-Zehnder Interferometry in a Strongly Driven Superconducting Qubit," *Science*, vol. 310, pp. 1653-1657, 2005.
- [37] P. Huang, J. W. Zhou, F. Fang, X. Kong, X. K. Xu, C. Y. Ju and J. F. Du, "Landau-Zener-Stückelberg Interferometry of a Single Electronic Spin in a Noisy Environment," *Phys. Rev. X*, vol. 1, p. 011003, 2011.
- [38] C. Betthausen, T. Dollinger, H. Saarikoski, V. Kolkovsky, G. Karczewski, T. Wojtowicz, K. Richter and D. Weiss, "Spin-Transistor Action via Tunable Landau-Zener Transitions," *Science*, vol. 337, pp. 324-327, 2012.
- [39] M. J. Biercuk, H. Uys, A. P. VanDevender, N. Shiga, W. M. Itano and J. J. Bollinger, "Optimized Dynamical Decoupling in a Model Quantum Memory," *Nature*, vol. 458, pp. 996-1000, 2009.
- [40] L. M. K. Vandersypen and I. L. Chuang, "NMR Techniques for Quantum Control and Computation," *Rev. Mod. Phys.*, vol. 76, p. 1037, 2005.
- [41] L. M. Duan, J. I. Cirac and P. Zoller, "Geometric Manipulation of Trapped Ions for Quantum Computation," *Science*, vol. 292, pp. 1695-1697, 2001.
- [42] J. A. Jones, V. Vedral, A. Ekert and G. Castagnoli, "Geometric Quantum Computation Using Nuclear Magnetic Resonance," *Nature*, vol. 403, pp. 869-871, 2000.
- [43] G. Falci, R. Fazio, G. M. Palma, J. Siewert and V. Vedral, "Detection of Geometric Phases in Superconducting Nanocircuits," *Nature*, vol. 407, pp. 355-358, 2000.

- [44] P. J. Leek, J. M. Fink, A. Blais, R. Bianchetti, M. Göppl, J. M. Gambetta, D. I. Schuster, L. Frunzio, R. J. Schoelkopf and A. Wallraff, "Observation of Berry's Phase in a Solid-State Qubit," *Science*, vol. 318, pp. 1889-1892, 2007.
- [45] Y. Ota and Y. Kondo, "Composite Pulses in NMR as Nonadiabatic Geometric Quantum Gates," *Phys. Rev. A*, vol. 80, p. 024302, 2009.
- [46] S. Gasparinetti, P. Solinas and J. P. Pekola, "Geometric Landau-Zener Interferometry," *Phys. Rev. Lett.*, vol. 107, p. 207002, 2011.
- [47] Y. Kayanuma, "Stokes Phase and Geometrical Phase in a Driven Two-Level System," *Phys. Rev. A*, vol. 55, p. R2495, 1997.
- [48] A. Zenesini, H. Lignier, G. Tayebirad, J. Radogostowicz, D. Ciampini, R. Mannella, S. Wimberger, O. Morsch and E. Arimondo, "Time-Resolved Measurement of Landau-Zener Tunneling in Periodic Potentials," *Phys. Rev. Lett.*, vol. 103, p. 090403, 2009.
- [49] M. Dakna, J. Clausen, L. Knoll and D. G. Welsch, "Generation of Arbitrary Quantum States of Traveling Fields," *Phys. Rev. A*, vol. 59, pp. 1658-1661, 1999.
- [50] H. Nha and H. J. Carmichael, "Proposed Test of Quantum Nonlocality for Continuous Variables," *Phys. Rev. Lett.*, vol. 93, p. 020401, 2004.
- [51] G. S. Agarwal and K. Tara, "Nonclassical Properties of States Generated by the Excitations on a Coherent State," *Phys. Rev. A*, vol. 43, pp. 492-497, 1991.
- [52] M. S. Kim, H. Jeong, A. Zavatta, V. Parigi and M. Bellini, "Scheme for Proving the Bosonic Commutation Relation Using Single-Photon Interference," *Phys. Rev. Lett.*, vol. 101, p. 260401, 2008.
- [53] R. Kumar, E. Barrios, C. Kupchak and A. I. Lvovsky, "Experimental Characterization of Bosonic Creation and Annihilation Operators," *Phys. Rev. Lett.*, vol. 110, p. 130403, 2013.
- [54] J. S. Neergaard-Nielsen, B. Melholt Nielsen, C. Hettich, K. Mølmer and E. S. Polzik, "Generation of a Superposition of Odd Photon Number States for Quantum Information Networks," *Phys. Rev. Lett.*, vol. 97, p. 083604, 2006.
- [55] A. Ourjoumtsev, R. Tualle-Brouri, J. Laurat and P. Grangier, "Generating Optical Schrodinger Kittens for Quantum Information Processing," *Science*, vol. 312, pp. 83-86, 2006.
- [56] V. Parigi, A. Zavatta, M. S. Kim and M. Bellini, "Probing Quantum Commutation Rules by Addition and Subtraction of Single photons to/from a Light Field," *Science*, vol. 317, pp. 1890-1893, 2007.
- [57] A. Zavatta, V. Parigi, M. S. Kim, H. Jeong and M. Bellini, "Experimental Demonstration of the

- Bosonic Commutation Relation via Superpositions of Quantum Operations on Thermal Light Fields," *Phys. Rev. Lett.*, vol. 103, p. 140406, 2009.
- [58] M. S. Kim, "Recent Developments in Photon-Level Operations on Travelling Light Fields," *J. Phys. B At. Mol. Opt. Phys.*, vol. 41, p. 133001, 2008.
- [59] K. L. Pagnell and D. T. Pegg, "Retrodictive Quantum Optical State Engineering," *J. Mod. Opt.*, vol. 51, p. 1613, 2004.
- [60] D. K. L. Oi, V. Potocek and J. Jeffers, "Nondemolition Measurement of the Vacuum State or its Complement," *Phys. Rev. Lett.*, vol. 110, p. 210504, 2013.
- [61] L. C. G. Góvia, E. J. Pritchett and F. K. Wilhelm, "Generating Nonclassical States from Classical Radiation by Subtraction Measurements," *New J. Phys.*, vol. 16, p. 045011, 2014.
- [62] H. J. Kim, S. Y. Lee, S. W. Ji and H. Nha, "Quantum Linear Amplifier Enhanced by Photon Subtraction and Addition," *Phys. Rev. A*, vol. 85, p. 013839, 2012.
- [63] S. Schneider, D. F. V. James and G. J. Milburn, "Method of Quantum Computation with 'Hot' Trapped Ions," 1998. [Online]. Available: <http://arxiv.org/abs/quant-ph/9808012>.
- [64] L. Susskind and J. Glogower, "Quantum Mechanical Phase and Time Operator," *Physics*, vol. 1, pp. 49-61, 1964.
- [65] J. Rehaek, Z. Hradil and M. Jezek, "Iterative Algorithm for Reconstruction of Entangled States," *Phys. Rev. A*, vol. 63, p. 040303(R), 2001.
- [66] L. Pezzé and A. Smerzi, "Entanglement, Nonlinear Dynamics, and the Heisenberg Limit," *Phys. Rev. Lett.*, vol. 102, p. 100401, 2009.
- [67] V. Giovannetti, S. Lloyd and L. Maccone, "Advances in Quantum Metrology," *Nature Photon.*, vol. 5, pp. 222-229, 2011.
- [68] G.-Q. Liu, Y.-R. Zhang, Y.-C. Chang, J.-D. Yue, H. Fan and X.-Y. Pan, "Demonstration of Entanglement-enhanced Phase Estimation in Solid," *Nature Commun.*, vol. 6, p. 6726, 2015.
- [69] B. C. Sanders, "Quantum Dynamics of the Nonlinear Rotator and the Effects of Continual Spin Measurement," *Phys. Rev. A*, vol. 40, pp. 2417-2427, 1989.
- [70] P. Kok, H. Lee and J. P. Dowling, "Creation of Large-photon-number Path Entanglement Conditioned on Photodetection," *Phys. Rev. A*, vol. 65, p. 052104, 2002.
- [71] M. W. Mitchell, J. S. Lundeen and A. M. Steinberg, "Super-resolving Phase Measurements with a Multiphoton Entangled State," *Nature*, vol. 429, pp. 161-164, 2004.
- [72] P. Walther, J.-W. Pan, M. Aspelmeyer, R. Ursin, S. Gasparoni and A. Zeilinger, "De Broglie

- Wavelength of a Non-local Four-photon State," *Nature*, vol. 429, pp. 158-161, 2004.
- [73] T. Nagata, R. Okamoto, J. L. O'Brien, K. Sasaki and S. Takeuchi, "Beating the Standard Quantum Limit with Four-Entangled Photons," *Science*, vol. 316, pp. 726-729, 2007.
- [74] I. Afek, O. Ambar and Y. Silberberg, "High-NOON States by Mixing Quantum and Classical Light," *Science*, vol. 328, pp. 879-881, 2010.
- [75] X.-L. Wang, L.-K. Chen, W. Li, H.-L. Huang, C. Liu, C. Chen, Y.-H. Luo, Z.-E. Su, D. Wu, Z.-D. Li, H. Lu, Y. Hu, X. Jiang, C.-Z. Peng, L. Li, N.-L. Liu, Y.-A. Chen, C.-Y. Lu and J.-W. Pan, "Experimental Ten-photon Entanglement," *Phys. Rev. Lett.*, vol. 117, p. 210502, 2016.
- [76] Y.-F. Huang, B.-H. Liu, L. Peng, Y.-H. Li, L. Li, C.-F. Li and G.-C. Guo, "Experimental Generation of an Eight-photon Greenberger–Horne–Zeilinger State," *Nature Commun.*, vol. 2, p. 546, 2011.
- [77] X.-C. Yao, T.-X. Wang, P. Xu, H. Lu, G.-S. Pan, X.-H. Bao, C.-Z. Peng, C.-Y. Lu, Y.-A. Chen and J.-W. Pan, "Observation of Eight-photon Entanglement," *Nature Photon.*, vol. 6, p. 225–228, 2012.
- [78] C. A. Sackett, D. Kielpinski, B. E. King, C. Langer, V. Meyer, C. J. Myatt, M. Rowe, Q. A. Turchette, W. M. Itano, D. J. Wineland and C. Monroe, "Experimental Entanglement of Four Particles," *Nature*, vol. 404, pp. 256-259, 2000.
- [79] D. Leibfried, E. Knill, S. Seidelin, J. Britton, R. B. Blakestad, J. Chiaverini, D. B. Hume, W. M. Itano, J. D. Jost, C. Langer, R. Ozeri, R. Reichle and D. J. Wineland, "Creation of a Six-atom 'Schrödinger Cat' State," *Nature*, vol. 438, pp. 639-642, 2005.
- [80] T. Monz, P. Schindler, J. T. Barreiro, M. Chwalla, D. Nigg, W. A. Coish, M. Harlander, W. Hansel, M. Hennrich and R. Blatt, "14-Qubit Entanglement: Creation and Coherence," *Phys. Rev. Lett.*, vol. 106, p. 130506, 2011.
- [81] J. A. Jones, S. D. Karlen, J. Fitzsimons, A. Ardavan, S. C. Benjamin, G. A. D. Briggs and J. J. L. Morton, "Magnetic Field Sensing Beyond the Standard Quantum Limit Using 10-spin NOON States," *Science*, vol. 324, pp. 1166-1168, 2009.
- [82] Y.-A. Chen, X.-H. Bao, Z.-S. Yuan, S. Chen, B. Zhao and J.-W. Pan, "Heralded Generation of an Atomic NOON State," *Phys. Rev. Lett.*, vol. 104, p. 043601, 2010.
- [83] H. Wang, M. Mariantoni, R. C. Bialczak, M. Lenander, E. Lucero, M. Neeley, A. D. O'Connell, D. Sank, M. Weides, J. Wenner, T. Yamamoto, Y. Yin, J. Zhao, J. M. Martinis and A. N. Cleland, "Deterministic Entanglement of Photons in Two Superconducting Microwave Resonators," *Phys. Rev. Lett.*, vol. 106, p. 060401, 2011.

- [84] D. Porras and J. I. Cirac, "Bose-Einstein Condensation and Strong-correlation Behavior of Phonons in Ion Traps," *Phys. Rev. Lett.*, vol. 93, p. 263602, 2004.
- [85] K. Toyoda, Y. Matsuno, A. Noguchi, S. Haze and S. Urabe, "Experimental Realization of a Quantum Phase Transition of Polaritonic Excitations," *Phys. Rev. Lett.*, vol. 111, p. 160501, 2013.
- [86] L. Ortiz-Gutiérrez, B. Gabrielly, L. F. Muñoz, K. T. Pereira, J. G. Filgueiras and A. S. Villar, "Continuous Variables Quantum Computation over the Vibrational Modes of a Single Trapped Ion," 2016. [Online]. Available: <https://arxiv.org/abs/1603.00065>.
- [87] K. Toyoda, R. Hiji, A. Noguchi and S. Urabe, "Hong-Ou-Mandel Interference of Two Phonons in Trapped Ions," *Nature*, vol. 527, pp. 74-77, 2015.
- [88] J. M. Raimond, M. Brune and S. Haroche, "Manipulating Quantum Entanglement with Atoms and Photons in a Cavity," *Rev. Mod. Phys.*, vol. 73, pp. 565-582, 2001.
- [89] F. Schmidt-Kaler, H. Haffner, M. Riebe, S. Gulde, G. P. T. Lancaster, T. Deuschle, C. Becher, C. F. Roos, J. Eschner and R. Blatt, "Realization of the Cirac-Zoller Controlled-NOT Quantum Gate," *Nature*, vol. 422, pp. 408-411, 2003.
- [90] J. J. Cooper and J. A. Dunningham, "Towards Improved Interferometric Sensitivities in the Presence of Loss," *New J. Phys.*, vol. 13, p. 115003, 2011.
- [91] S. L. Braunstein and C. M. Caves, "Statistical Distance and the Geometry of Quantum States," *Phys. Rev. Lett.*, vol. 72, pp. 3439-3443, 1994.
- [92] M. D. Barrett, B. DeMarco, T. Schaetz, V. Meyer, D. Leibfried, J. Britton, J. Chiaverini, W. M. Itano, B. Jelenkovic, J. D. Jost, C. Langer, T. Rosenband and D. J. Wineland, "Sympathetic Cooling of $^9\text{Be}^+$ and $^{24}\text{Mg}^+$ for Quantum Logic," *Phys. Rev. A*, vol. 68, p. 042302, 2003.
- [93] Y. Lin, J. P. Gaebler, F. Reiter, T. R. Tan, R. Bowler, A. S. Sorensen, D. Leibfried and D. J. Wineland, "Dissipative Production of a Maximally Entangled Steady State of Two Quantum Bits," *Nature*, vol. 504, pp. 415-418, 2013.
- [94] D. B. Hume, T. Rosenband and D. J. Wineland, "High-Fidelity Adaptive Qubit Detection through Repetitive Quantum Nondemolition Measurements," *Phys. Rev. Lett.*, vol. 99, p. 120502, 2007.
- [95] C. J. Ballance, V. M. Schäfer, J. P. Home, D. J. Szwer, S. C. Webster, D. T. C. Allcock, N. M. Linke, T. P. Harty, D. P. L. Aude Craik, D. N. Stacey, A. M. Steane and D. M. Lucas, "Hybrid Quantum Logic and a Test of Bell's Inequality Using Two Different Atomic Isotopes," *Nature*, vol. 528, pp. 384-386, 2015.

Reference

- [96] T. R. Tan, J. P. Gaebler, Y. Lin, Y. Wan, R. Bowler, D. Leibfried and D. J. Wineland, "Multi-Element Logic Gates for Trapped-Ion Qubits," *Nature*, vol. 528, pp. 380-383, 2015.
- [97] I. V. Inlek, C. Crocker, M. Lichtman, K. Sosnova and C. Monroe, "Multi-Species Trapped Ion Node for Quantum Networking," *Phys. Rev. Lett.*, vol. 118, p. 250502, 2017.

Acknowledgement

I would like to thank my supervisor, Prof. Kihwan Kim, for insightful guidance during the years, both on academic research and personal life. He is always willing to help whenever I feel lost. His modest altitude, his diligence and his enthusiasm deeply influences me. In the early years, his expertise and hand to hand teaching helps a lot to save me from tedious trials and errors. I am grateful that it is him that leads me into this realm of experimental physics where I find my interests.

I also appreciate the time with all our group members. We make an amazing team, whether inside or outside the lab. Working with active and brilliant guys is always my favorite. After years of cooperation, we are quite a tight group. I know I can count on them.

Moreover, I would like to thank Prof. Luming Duan, Prof. Hyunchul Nha and Prof. Myungshik Kim for their theory collaborations.

Finally, I want to express my gratitude to my wife, Lu Dandan. We have been through a lot. She is encouraging and supportive while I pursue my research career. I am grateful that I find her as my companion for life.

声 明

本人郑重声明：所呈交的学位论文，是本人在导师指导下，独立进行研究工作所取得的成果。尽我所知，除文中已经注明引用的内容外，本学位论文的研究成果不包含任何他人享有著作权的内容。对本论文所涉及的研究工作做出贡献的其他个人和集体，均已在文中以明确方式标明。

签 名： _____ 日 期： _____

Appendix A Verilog Code of the Pulse Sequencer

A.1 Top Module

```
module PulseSequencer(clk, rxd, ptrg, out, led1, led2);
```

```
parameter TW = 40;
```

```
parameter OW = 32-1;
```

```
parameter RW = 24;
```

```
input  clk;
```

```
input  rxd;
```

```
input  ptrg;
```

```
output [OW : 0] out;
```

```
output led1;
```

```
output led2;
```

```
wire led1 = ~hold;
```

```
wire c0 = clk;
```

```
wire [RW-1 : 0] rep;
```

```
wire [TW+OW : 0] seq;
```

```
wire ftrg;
```

```
wire hedrcv;
```

```
wire seqrcv;
```

```
wire endrcv;
```

```
PS_InputDispatcher #(TW, OW, RW, 10) INPD(c0, rxd, rep, seq, ftrg, hedrcv, seqrcv,  
endrcv);
```

```
wire hold;
```

```

wire init;
PS_Controller #(RW) CTRL(c0, hedrcv, endrcv, rep, sfin, ptrg, ftrg, hold, init, led2);

wire [TW : 0] str;
wire [TW : 0] cry;
wire [OW : 0] lvl;
wire sfin;
reg rst = 0;
always @ (posedge c0) rst <= hedrcv;
PS_FIFO_Assembly #(TW, OW) FIFO(c0, seq, tick, seqrcv, rst, str, cry, lvl, sfin);

wire tick;
Core_Ticker_RP #(TW, 1'b0) TIMER(c0, 1'b1, {str[TW] | init, str[TW-1:0]}, cry, hold,
tick);

reg [OW : 0] out = 0;
always @ (posedge c0) if (tick) out <= lvl & {(OW+1){~init}};

endmodule

```

A.2 Input Dispatcher

```

module PS_InputDispatcher(clk, rxd, rep, seq, ftrg, hedrcv, seqrcv, endrcv);

parameter TW = 40;
parameter OW = 32-1;
parameter RW = 24;
parameter Byt = 10;

parameter Len = Byt*8-1;

input  clk;
input  rxd;

```

```
output [RW-1 : 0] rep;
output [TW+OW : 0] seq;
output frg;
output hedrcv;
output seqrcv;
output endrcv;

wire [Len : 0] str;
wire tmp;
RS232_StringRecv #(Byt, 50, 1) SRCV(clk, rxd, str, tmp);

reg [RW-1 : 0] rep = 0;
always @ (posedge clk) if (t[2]) rep <= str[RW-1:0];

reg frg = 0;
always @ (posedge clk) if (t[2]) frg <= str[Len-3];

reg [TW+OW : 0] seq = 0;
always @ (posedge clk) if (t[1]) seq <= str[TW+OW:0];

reg [2 : 0] t = 0;
reg hedrcv = 0;
reg seqrcv = 0;
reg endrcv = 0;
always @ (posedge clk)
begin
    t <= str[Len:Len-2] & {3{tmp}};
    {hedrcv, seqrcv, endrcv} <= t;
end

endmodule

module RS232_ByteRecv(clk, in, byt, rcv, brk);
```

```
parameter Baud = 17;
parameter StopBit = 1;

parameter BaudCnt = Baud - 1;

input  clk;
input  in;
output [7 : 0] byt;
output recv;
output brk;

reg idle = 1;
always @ (posedge clk) idle <= (idle & in) | recv;

wire tick;
Core_Ticker #(BaudCnt) BAUD(clk, 1'b1, idle, tick);

wire brk;
Core_Ticker #(BaudCnt<<20) RBRK(clk, idle, recv, brk);

wire smp;
Core_Ticker #((BaudCnt>>1)+2) SAMP(clk, in, tick, smp);

reg cbt = 0;
always @ (posedge clk) cbt <= (smp | cbt) & ~tick;

reg [7+StopBit : 0] tmp = 0;
wire [7 : 0] byt = tmp[7:0];
always @ (posedge clk) if (tick) tmp <= {cbt, tmp[7+StopBit:1]};

reg [8+StopBit : 0] cnt = 2;
always @ (posedge clk) if (tick) cnt <= {cnt, cnt[8+StopBit]};
```

```
reg recv = 0;
always @ (posedge clk) recv <= tick & cnt[0];

endmodule

module RS232_StringRecv(clk, in, str, recv);

parameter Len = 1;
parameter BaudCnt = 159;
parameter StopBit = 1;

input  clk;
input  in;
output [Len*8-1 : 0] str;
output recv;

wire [7 : 0] byt;
wire tick;
wire brk;
RS232_ByteRecv #(BaudCnt, StopBit) BRCV(clk, in, byt, tick, brk);

reg [Len*8-1 : 0] str = 0;
always @ (posedge clk) if (tick) str <= {str, byt};

reg [Len-1 : 0] cnt = 2;
always @ (posedge clk) if (brk) cnt <= 2; else if (tick) cnt <= {cnt, cnt[Len-1]};

reg recv = 0;
always @ (posedge clk) recv <= tick & cnt[0];

endmodule
```


A.3 Controller

```
module PS_Controller(clk, hedrcv, endrcv, rep, sfin, ptrg, ftrg, hold, init, led);
```

```
parameter RW = 24;
```

```
input  clk;
input  hedrcv;
input  endrcv;
input  [RW-1 : 0] rep;
input  sfin;
input  ptrg;
input  ftrg;
output hold;
output init;
output led;
```

```
wire led = etrg;
```

```
reg [12 : 0] dly = 0;
reg init = 0;
always @ (posedge clk) dly <= {dly, endrcv};
always @ (posedge clk) if (endrcv) init <= 1; else if (dly[12]) init <= 0;
```

```
reg t1 = 0;
reg t2 = 0;
reg trg = 0;
always @ (posedge clk) t1 <= ptrg;
always @ (posedge clk) t2 <= t1;
always @ (posedge clk) trg <= (t1 & ~t2) | ftrg;
```

```
reg etrg = 0;
always @ (posedge clk) if (dly[12]) etrg <= 1; else if (sfin & rcnt[RW] | hedrcv) etrg <=
```

```
0;

reg hold = 1;
always @ (posedge clk) if (sfin | hedrcv | dly[12]) hold <= 1; else if (dly[0] | trg & etrg)
hold <= 0;

reg [RW : 0] rcnt = {(RW+1){1'b1}};
always @ (posedge clk) if (dly[0]) rcnt <= {1'b0, rep} - 1; else if (sfin) rcnt <= rcnt - 1;

endmodule
```

A.4 FIFO Array

```
module PS_FIFO_Assembly(clk, din, reqr, reqw, rst, str, cry, lvl, sfin);
```

```
parameter TW = 40;
parameter OW = 32-1;
```

```
input   clk;
input   [TW+OW : 0] din;
input   reqr;
input   reqw;
input   rst;
output  [TW : 0] str;
output  [TW : 0] cry;
output  [OW : 0] lvl;
output  sfin;
```

```
reg [4 : 0] rpnt = 1 /* -pragma maxfan = 24 */;
reg [4 : 0] wpnt = 1;
always @ (posedge clk or posedged rst) if (rst) rpnt <= 1; else if (reqr) rpnt <= {rpnt[3:0],
rpnt[4]};
always @ (posedge clk or posedged rst) if (rst) wpnt <= 1; else if (reqw) wpnt <=
```

```

{wpnt[3:0], wpnt[4]};

wire [TW : 0] tr0 = {(TW+1){rpnt[0]}};
wire [TW : 0] tr1 = {(TW+1){rpnt[1]}};
wire [TW : 0] tr2 = {(TW+1){rpnt[2]}};
wire [TW : 0] tr3 = {(TW+1){rpnt[3]}};
wire [TW : 0] tr4 = {(TW+1){rpnt[4]}};
reg [TW : 0] t11 = 0;   reg [TW : 0] t21 = 0;   reg [TW : 0] t31 = 0;
reg [TW : 0] t12 = 0;   reg [TW : 0] t22 = 0;   reg [TW : 0] t32 = 0;
reg [OW : 0] t13 = 0;   reg [OW : 0] t23 = 0;   reg [OW : 0] t33 = 0;
reg [TW : 0] str = 0;
reg [TW : 0] cry = 0;
reg [OW : 0] lvl = 0;
always @(posedge clk) if (reqr)
begin
    t11 <= (st0 & tr0) | (st1 & tr1);   t21 <= st2 & tr2;   t31 <= (st3 & tr3) | (st4 & tr4);
    t12 <= (cr0 & tr0) | (cr1 & tr1);   t22 <= cr2 & tr2;   t32 <= (cr3 & tr3) | (cr4 & tr4);
    t13 <= (lv0 & tr0) | (lv1 & tr1);   t23 <= lv2 & tr2;   t33 <= (lv3 & tr3) | (lv4 & tr4);
    str <= t11 | t21 | t31;
    cry <= t12 | t22 | t32;
    lvl <= t13 | t23 | t33;
end

wire [TW : 0] st0;
wire [TW : 0] cr0;
wire [OW : 0] lv0;
PS_FIFO #(TW, OW) QUE0(clk, din, reqr & rpnt[0], reqw & wpnt[0], rst, st0, cr0, lv0);

wire [TW : 0] st1;
wire [TW : 0] cr1;
wire [OW : 0] lv1;
PS_FIFO #(TW, OW) QUE1(clk, din, reqr & rpnt[1], reqw & wpnt[1], rst, st1, cr1, lv1);

```

```
wire [TW : 0] st2;
wire [TW : 0] cr2;
wire [OW : 0] lv2;
PS_FIFO #(TW, OW) QUE2(clk, din, reqr & rpnt[2], reqw & wpnt[2], rst, st2, cr2, lv2);
```

```
wire [TW : 0] st3;
wire [TW : 0] cr3;
wire [OW : 0] lv3;
PS_FIFO #(TW, OW) QUE3(clk, din, reqr & rpnt[3], reqw & wpnt[3], rst, st3, cr3, lv3);
```

```
wire [TW : 0] st4;
wire [TW : 0] cr4;
wire [OW : 0] lv4;
PS_FIFO #(TW, OW) QUE4(clk, din, reqr & rpnt[4], reqw & wpnt[4], rst, st4, cr4, lv4,
sfn);
```

```
endmodule
```

```
module PS_FIFO(clk, din, reqr, reqw, rst, str, cry, lvl, sfn);
```

```
`include "Functions.v"
```

```
parameter TW = 40;
```

```
parameter OW = 32-1;
```

```
parameter [TW-1 : 0] Zero = Ticker_Conv_Start(0, TW);
```

```
input  clk;
```

```
input  [TW+OW : 0] din;
```

```
input  reqr;
```

```
input  reqw;
```

```
input  rst;
```

```
output [TW : 0] str;
```

```

output [TW : 0] cry;
output [OW : 0] lvl;
output sfin;

reg dreq = 0;
always @ (posedge clk) dreq <= reqr;

reg tr = 0;
reg rclk = 0;
always @ (posedge clk) begin tr <= dreq; rclk <= dreq | tr; end
reg tw = 0;
reg wclk = 0;
always @ (posedge clk) begin tw <= reqw; wclk <= reqw | tw; end

reg [10 : 0] h = 0;
reg [10 : 0] t = 0;
reg [10 : 0] f = 0;
always @ (posedge rclk or posedge rst) if (rst) h <= 0; else if (h == f) h <= 0; else h <= h
+ 1;
always @ (posedge wclk or posedge rst) if (rst) t <= 0; else t <= t + 1;
always @ (posedge wclk) f <= t;

reg [TW+OW : 0] ram [0 : 1535];
always @ (posedge wclk) ram[t] <= din;

reg [TW+OW : 0] tmp = 0;
always @ (posedge rclk) tmp <= ram[h];

wire [OW : 0] tlw = tmp[OW:0];
wire [TW : 0] tst = {(tmp[TW+OW:1+OW] == Zero), tmp[TW+OW:1+OW]};
wire [TW : 0] tcr;
TIC_Converter #(TW) CONV(tst[TW-1:0], tcr);

```

```
reg [OW : 0] lvl = 0;
reg [TW : 0] str = 0;
reg [TW : 0] cry = 0;
always @ (posedge clk) if (dreq)
begin
    lvl <= tlvl;
    str <= tst;
    cry <= tcr;
end

reg [1 : 0] d = 0;
reg sfin = 0;
always @ (posedge clk)
begin
    d <= {d, (h == 2)};
    sfin <= d[0] & ~d[1];
end

endmodule

module TIC_Converter(str, cry);

parameter CntWid = 1;

parameter MaxWid = 48;

input  [CntWid-1 : 0] str;
output [CntWid : 0] cry;

wire [MaxWid-1 : 0] s = str;
wire [CntWid : 0] cry = c[CntWid : 0];

reg [MaxWid : 0] c = 0;
```

```
always
begin
  c[00] <= 1'b1;
  c[01] <= (s[00:0] == 00);  c[02] <= (s[01:0] == 01);
  c[03] <= (s[02:0] == 00);  c[04] <= (s[03:0] == 03);
  c[05] <= (s[04:0] == 02);  c[06] <= (s[05:0] == 01);
  c[07] <= (s[06:0] == 04);  c[08] <= (s[07:0] == 07);
  c[09] <= (s[08:0] == 06);  c[10] <= (s[09:0] == 05);
  c[11] <= (s[10:0] == 00);  c[12] <= (s[11:0] == 11);
  c[13] <= (s[12:0] == 10);  c[14] <= (s[13:0] == 09);
  c[15] <= (s[14:0] == 12);  c[16] <= (s[15:0] == 15);
  c[17] <= (s[16:0] == 14);  c[18] <= (s[17:0] == 13);
  c[19] <= (s[18:0] == 08);  c[20] <= (s[19:0] == 03);
  c[21] <= (s[20:0] == 18);  c[22] <= (s[21:0] == 17);
  c[23] <= (s[22:0] == 20);  c[24] <= (s[23:0] == 23);
  c[25] <= (s[24:0] == 22);  c[26] <= (s[25:0] == 21);
  c[27] <= (s[26:0] == 16);  c[28] <= (s[27:0] == 27);
  c[29] <= (s[28:0] == 26);  c[30] <= (s[29:0] == 25);
  c[31] <= (s[30:0] == 28);  c[32] <= (s[31:0] == 31);
  c[33] <= (s[32:0] == 30);  c[34] <= (s[33:0] == 29);
  c[35] <= (s[34:0] == 24);  c[36] <= (s[35:0] == 19);
  c[37] <= (s[36:0] == 02);  c[38] <= (s[37:0] == 33);
  c[39] <= (s[38:0] == 36);  c[40] <= (s[39:0] == 39);
  c[41] <= (s[40:0] == 38);  c[42] <= (s[41:0] == 37);
  c[43] <= (s[42:0] == 32);  c[44] <= (s[43:0] == 43);
  c[45] <= (s[44:0] == 42);  c[46] <= (s[45:0] == 41);
  c[47] <= (s[46:0] == 44);  c[48] <= (s[47:0] == 47);
end

endmodule
```

A.5 Timer

```
module Core_Ticker_RP(clk, trg, str, cry, set, tic);
```

```
parameter CntWid = 32;
```

```
parameter PwrTic = 1'b1;
```

```
input  clk;
```

```
input  trg;
```

```
input  [CntWid : 0] str;
```

```
input  [CntWid : 0] cry;
```

```
input  set;
```

```
output tic;
```

```
reg tic = PwrTic;
```

```
reg [CntWid-1 : 0] c0 = 0;
```

```
reg [CntWid : 0] c1 = 0;
```

```
always @ (posedge clk)
```

```
if (tic | set)
```

```
begin
```

```
    {tic, c0} <= str;
```

```
    c1 <= cry;
```

```
end
```

```
else if (trg)
```

```
begin
```

```
    {tic, c0} <= {tic, c0} ^ c1;
```

```
    c1 <= {c0 & c1[CntWid-1 : 0], 1'b1};
```

```
end
```

```
endmodule
```


A.6 Common Modules and Functions

```
module Core_Ticker(clk, trg, set, tic);
```

```
  `include "Functions.v"
```

```
  parameter Interval = 1;
```

```
  parameter CntWid = GetSize(Interval);
```

```
  parameter [CntWid : 0] Start = Ticker_Conv_Start(Interval, CntWid);
```

```
  parameter [CntWid : 0] Carry = Ticker_Conv_Carry(Interval, CntWid);
```

```
  input  clk;
```

```
  input  trg;
```

```
  input  set;
```

```
  output tic;
```

```
  reg tic = Start[CntWid] /* -pragma maxfan = 11 */;
```

```
  reg [CntWid-1 : 0] c0 = Start[CntWid-1:0];
```

```
  reg [CntWid : 0] c1 = Carry;
```

```
  always @ (posedge clk)
```

```
  if (tic | set)
```

```
  begin
```

```
    {tic, c0} <= Start;
```

```
    c1 <= Carry;
```

```
  end
```

```
  else if (trg)
```

```
  begin
```

```
    {tic, c0} <= {tic, c0} ^ c1;
```

```
    c1 <= {c0 & c1[CntWid-1 : 0], 1'b1};
```

```
  end
```

```
endmodule
```

```
function integer GetSize;
```

```
input [63 : 0] Num;
```

```
integer S;
```

```
begin
```

```
    S = 0;
```

```
    while (Num > 0)
```

```
    begin
```

```
        S = S + 1;
```

```
        Num = Num >> 1;
```

```
    end
```

```
    if (S == 0) GetSize = 64; else GetSize = S;
```

```
end
```

```
endfunction
```

```
function [63 : 0] Ticker_Conv_Start;
```

```
input [63 : 0] Num;
```

```
input integer Wid;
```

```
integer i;
```

```
reg [63 : 0] t0;
```

```
reg [63 : 0] t1;
```

```
begin
```

```
    t0 = 0;
```

```
    t1 = 0;
```

```
    Num = (1 << Wid) + Wid - Num;
```

```
    for (i = 0; i <= Wid; i = i + 1)
```

```
begin
    t0[i] = Num[i];
    t1[i] = (t0 < i) | (t0 >= (1 << i) + i);
end
Ticker_Conv_Start = t1;
end
```

```
endfunction
```

```
function [63 : 0] Ticker_Conv_Carry;
```

```
input [63 : 0] Num;
input integer Wid;
```

```
integer i;
reg [63 : 0] t0;
reg [63 : 0] t1;
begin
    t0 = 0;
    t1 = 0;
    Num = (1 << Wid) + Wid - Num;
    for (i = 0; i < Wid; i = i + 1)
        begin
            t0[i] = Num[i];
            t1[i+1] = (t0 == i);
        end
    t1[0] = 1'b1;
    Ticker_Conv_Carry = t1;
end
```

```
endfunction
```

个人简历、在学期间发表的学术论文与研究成果

个人简历

1990年3月29日生于福建省福州市。

2008年9月考入北京大学物理学院物理专业，2012年7月本科毕业并获得理学学士学位。

2012年9月免试进入清华大学交叉信息研究院攻读理学博士学位至今。

发表的学术论文

- [1] M. Um, **J. H. Zhang** (co-first author), D. S. Lv, Y. Lu, S. M. An, J. N. Zhang, H. Nha, M. S. Kim and K. Kim, "Phonon Arithmetic in a Trapped Ion System", *Nature Commun.*, vol. 7, p. 11410, 2016.
- [2] **J. H. Zhang** and K. Kim, "Realization of Geometric Landau-Zener-Stückelberg Interferometry", *Phys. Rev. A*, vol. 89, p. 013608, 2014.
- [3] Y. Wang, M. Um, **J. H. Zhang**, S. M. An, M. Lyu, J. N. Zhang, L. M. Duan, D. Yum and K. Kim, "Single-Qubit Quantum Memory Exceeding Ten-Minute Coherence Time," *Nature Photon.*, vol. 11, pp. 646-650, 2017.
- [4] X. Zhang, Y. C. Shen, **J. H. Zhang**, J. Casanova, L. Lamata, E. Solano, M. H. Yung, J. N. Zhang and K. Kim, "Time Reversal and Charge Conjugation in an Embedding Quantum Simulator", *Nature Commun.*, vol. 6, p. 8917, 2015.
- [5] J. Park, **J. H. Zhang**, J. Lee, S. W. Ji, M. Um, D. S. Lv, K. Kim and H. Nha, "Testing Nonclassicality and Non-Gaussianity in Phase Space", *Phys. Rev. Lett.*, vol. 114, p. 190402, 2015.
- [6] X. Zhang, M. Um, **J. H. Zhang**, S. M. An, Y. Wang, D. L. Deng, C. Shen, L. M. Duan and K. Kim, "State-independent Experimental Test of Quantum Contextuality with a Single Trapped Ion", *Phys. Rev. Lett.*, vol. 110, p. 070401, 2013.